ABSTRACT

Title of Dissertation: A COMPUTATIONAL STUDY OF THE FORCE GENERATION MECHANISMS IN FLAPPING-WING HOVERING FLIGHT

Brandon L. Bush, Doctor of Philosophy, 2013

Dissertation Directed by: Dr. James D. Baeder
Department of Aerospace Engineering

An incompressible Navier-Stokes computational fluid dynamics (CFD) solver is developed for simulating flapping wings at Reynolds numbers (Re) of approximately 10^2 – 10^3 in which the governing equations are solved in an immersed boundary framework on fixed Cartesian meshes. The dissertation work is divided into two portions: (1) Implementation of the immersed boundary method for incompressible low-*Re* flowfields. The applicability and robustness of various solution schemes are studied, with specific applicability to low Re biological flows (staggered variable formulations versus collocated implementations, upwind schemes as applied to incompressible flows, ray-tracing and geometric optimization of immersed boundary determination, Large Eddy Simulation (LES) model implementations). (2) The extension and application of the flow solver (IBINS) to model flapping-wing kinematics, and the analysis of the influence of kinematics and flow parameters on the force production for idealized flapping strokes. A representative *Drosophila* wing is simulated undergoing an idealized periodic flapping

stroke. A detailed characterization of the vortical structures that develop in the near and far wake, along with their correlation with the force and power time histories, is given for simulations of various stroke kinematics at $Re = 147$ and $Re = 1400$.

A COMPUTATIONAL STUDY OF THE FORCE GENERATION MECHANISMS IN FLAPPING-WING HOVERING FLIGHT

by

Brandon L. Bush

Dissertation submitted to the Faculty of the Graduate School of the
University of Maryland at College Park in partial fulfillment
of the requirements for the degree of
Doctor of Philosophy
2013

Advisory Committee:

Dr. James D. Baeder, Chairman/Advisor
Dr. J. Gordon Leishman
Dr. Inderjit Chopra
Dr. J. Sean Humbert
Dr. Anya Jones
Dr. Ramani Duraiswami, Dean's Representative

Dedicated to my mother,

Barbara,

and my late father,

Ralph.

ACKNOWLEDGEMENTS

If it takes a village to raise a child, then it takes a small well-funded metropolis to get them their doctorate. I cannot thank enough the countless people who helped me finish this research. My Advisor, Dr. Baeder, was the most patient and flexible Ph.D. advisor a student could hope for. The faculty and staff of the UMD Aerospace Engineering Department, the College of Engineering and Computer Science and the UMD Graduate School during my time here all helped immensely as well. But I think that my journey, as it seems to be with many doctoral students, was more a struggle of personal will and perseverance than academics, and those people who helped most with those challenges were my friends and family. Students of the Alfred Gessow Rotorcraft Center, foremost, but many other graduate students, former graduate students, faculty and family were constant mentors. I am deeply thankful for everyone who called, wrote, e-mailed, texted, whispered, yelled, and even pestered me with words of encouragement. I do not know that I could have finished this without you all.

TABLE OF CONTENTS

LIST OF FIGURES

NOMENCLATURE

Roman Symbols

A	Spatial coefficient matrix
B_{ijk}	"Bottom" coefficient in spatial discretization equations
c	Wing chord, m
$\bar{c}$	Mean chord, S/R
$\bar{c}_w$	Velocity-weighted mean chord, $3\int_0^1 \hat{r}^2 c(\hat{r}) d\hat{r}$
$c_1, c_2, b_1, b_2, \ldots$	Interpolation equation constants
D	Drag, N
E_{ijk}	"East" coefficient in spatial discretization equations
f	Flapping frequency, s^{-1}
i,j,k	Indices in the x, y, z directions, respectively
i,j	Indicial notation indices
K	Local permeability in continuous forcing IB equations
k	Reduced frequency, $0.5\omega\bar{c}\bar{V}_{tip}{}^{-1}$
L	Lift, N
M	Mach number
N_{ijk}	"North" coefficient in spatial discretization equations
n	Discrete time interval index

$\hat{n}$	Normal vector
P	Pressure, N m^{-2}
Q	Q-criterion: second invariant of the velocity gradient tensor
R	Wing radius, m
R_c	Wing root offset, m
Re	Reynolds Number, $\bar{c}\bar{V}_{tip}/\nu$
r	Radial distance along wingspan, m
$\hat{r}$	Non-dimensional radial coordinate, r/R
S	Surface area
S_w	Velocity-weighted surface area
$\bar{S}_{ij}$	Filtered strain rate tensor
S_{ijk}	"South" coefficient in spatial discretization equations
T	Stroke period, s
T_{ijk}	"Top" coefficient in spatial discretization equations
t	Time, s
t_c	Characteristic time, s
u	Velocity component in the x-direction
u_1, u_2, u_{tip}	Scalar quantity at an immersed boundary locations
u_i	$i = 1,2,3$ component of the velocity vector
u_i^*	$i = 1,2,3$ component of the predicted velocity field
u',u''	Intermediate velocity fields in Runge-Kutta schemes
$\bar{u}$	Spatially filtered velocity field for filtered Navier-Stokes
$\langle\bar{u}\rangle$	Spatially filtered velocity field at grid and test scales

V	Velocity, m s^{-1}
v	velocity component in the y-direction
W_{ijk}	"West" coefficient in spatial discretization equations
w	velocity component in the z-direction
x, y, z	Cartesian coordinate directions

Greek Symbols

α	Geometric pitch angle
β	Ratio of divided differences
Δt	Discrete time step size
Δx, Δy, Δz	Discrete spatial step sizes in x, y, and z directions
δ	Dirac delta function
Φ	Total stroke angle for flapping cases, rad
ϕ	Pseudo-pressure
φ	Limiter function
μ	Dynamic viscosity, N s m^{-2}
ν	Kinematic viscosity, m^2 s^{-1}
ν_T	Turbulent eddy viscosity, m^2 s^{-1}
Ω	Angular rotational velocity about the flapping axis, s^{-1}
ω_r, ω_p	Rotational velocity for flapping and pitching, respectively, s^{-1}
τ	Non-dimensionsal stroke time, t/T

τ_{ij}	Subgrid scale stress tensor
T	Flapping stroke period, s

Abbreviations

AB2	2nd order Adams-Bashforth
CFD	Computational Fluid Dynamics
CFL	Courant-Friedrichs-Lewy number $u\Delta t/\Delta x$
CN	Crank-Nicolson
DNS	Direct Numerical Simulation
GTOW	Gross Takeoff Weight
IB	Immersed Boundary
IBINS	Immersed Boundary Incompressible Navier-Stokes Solver
LES	Large Eddy Simulation
LEV	Leading Edge Vortex
MAV	Micro-Air Vehicle
MPI	Message Passing Interface
RK3	3rd order Runge-Kutta
SGS	Subgrid Scale
TEV	Trailing Edge Vortex

Chapter 1 –

Introduction

Large-scale, human-sized flapping-wing ornithopters (flapping vehicles modeled after bird flight) have a long history in aviation research and development; perhaps longer than the fixed and rotating-wing vehicles that have become the staples of manned flight. However, while some successful full-scale flapping vehicles have been designed, flapping wing research has lagged behind its counterparts. This is primarily because when designing a flight vehicle to carry a large payload, or achieve a long endurance, or fly a great distance – all practical design requirements that fixed and rotary winged aircraft can excel at – flapping wings have traditionally been far less efficient. Yet nature provides a variety of examples of highly "efficient" flapping wing platforms.

In recent years, as modern security, surveillance, search & rescue, and warfare activities begin to frequently require remote operation in confined, urban or otherwise obstacle-rich environments, an increasing number of applications for small, highly maneuverable, hover-capable air platforms has arisen. The ability of the natural flappers to meet these demands, combined with the miniaturization of mechanical and electrical components and advances in light-weight materials to help meet the mechanical demands of constructing these "Micro-Air Vehicles" (MAVs), has thrust smaller scale flapping-wing research forward on its path towards maturity.

1.1 Flapping-Wing Micro-Air Vehicles

The US Defense Advanced Research Projects Agency (DARPA) initially defined a standard for MAVs including the requirements that the flight vehicle have no dimension larger than 15cm, an endurance of about an hour, and a GTOW of less than 100 grams. DARPA has since defined a second, lighter class of vehicles called "Nano-Air Vehicles" (NAV) which should have no dimension greater than 15cm and a GTOW of less than 20 grams.

1.1.1 Representative Current MAVs

These DARPA sizing criteria have proven challenging to meet, because, as will be discussed, the physical understanding of aerodynamic mechanisms, mathematical models, design tools, and assumptions that have been developed for full-scale flight vehicles do not efficiently translate to these smaller scales. Nevertheless, a number of vehicles have been successfully developed with the DARPA sizing criteria in mind, and many of these have been flapping-wing designs. Figure 1.1 shows a few representative examples of these. Flapping-wing MAVs are generally separated into two categories. "Avian flappers" or ornithopters, such as the Lilienthal ornithopter studied at the University of Maryland [1] and the novel clap-and-fling biplane from the Naval Postgraduate School (Figure 1.1a) have a flapping stroke similar to a bird's in which the wing-stroke is perpendicular to the direction of travel and the change in angle of incidence is relatively small. "Insect flappers", such as the AeroVironment Hummingbird (Figure 1.1) have a stroke that is not necessarily perpendicular to the travel direction, during which the wings undergo large changes in pitch angle. Examples include

Michelson's "Entomopter" [2], a term which the literature has begun to use as the generic term for any flapping MAV using an insect-like kinematic stroke. As in nature, the larger flapping MAVs tend to be of the avian flapping design (although the Delfly Mirco, at 10 cm, is a notably small avian flapper), while smaller scale flappers tend to use the insect-flapping stroke. Because the lift for an Entomopter is generated primarily by the kinematics of the wing, and does not require a relative wind to stay aloft as the typical avian flapper would, insect flapping is of particular interest for MAV development where indoor operation or hover capability is a key requirement.

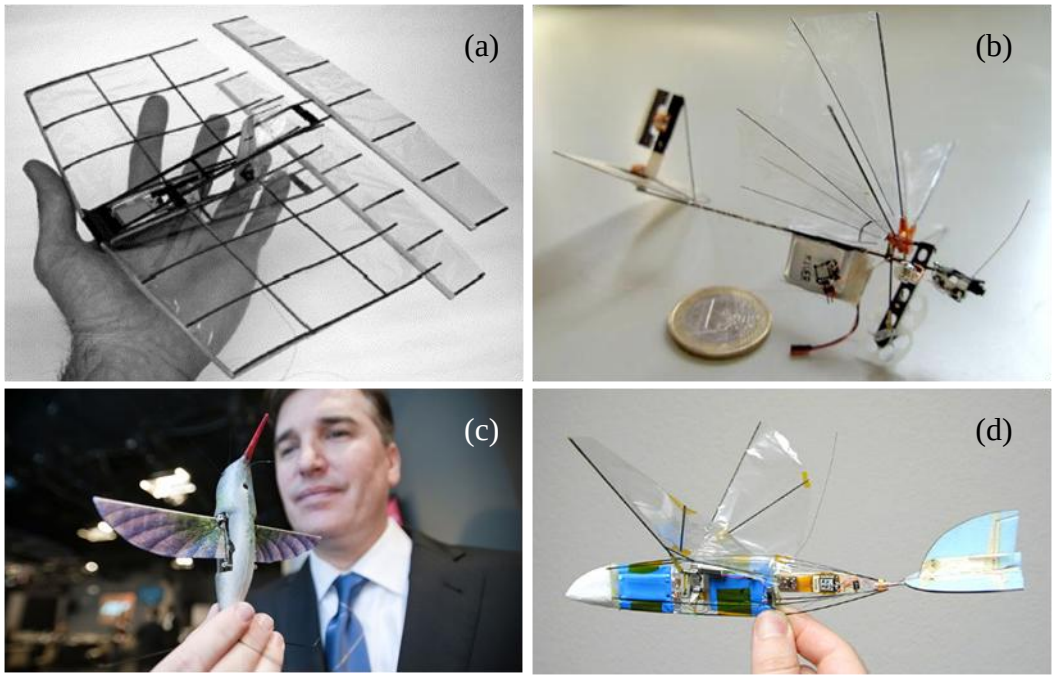

Figure 1.1: Examples of current flapping wing MAVs (a) Naval Postgraduate school flapper, (b) Delfly Micro, (c) AeroVironment's Hummingbird, (d) Microbat.

Even with the successful implementation of these and other flapping wing MAVs, rotating-wing MAVs still represent the bulk of the vehicles being developed at this scale.

A sample of representative types of rotating-wing designs is shown in Figure 1.2. A primary reason for this is the maturity of the full-scale rotorcraft technology, compared with that of large-scale flappers. A variety of examples exist, from coaxial configurations like the University of Maryland's MICOR, shrouded rotors such as the TiShrov, quad-rotors (Pereira et al. [3]), and non-traditional rotary concepts such as the Cyclocopter [4].

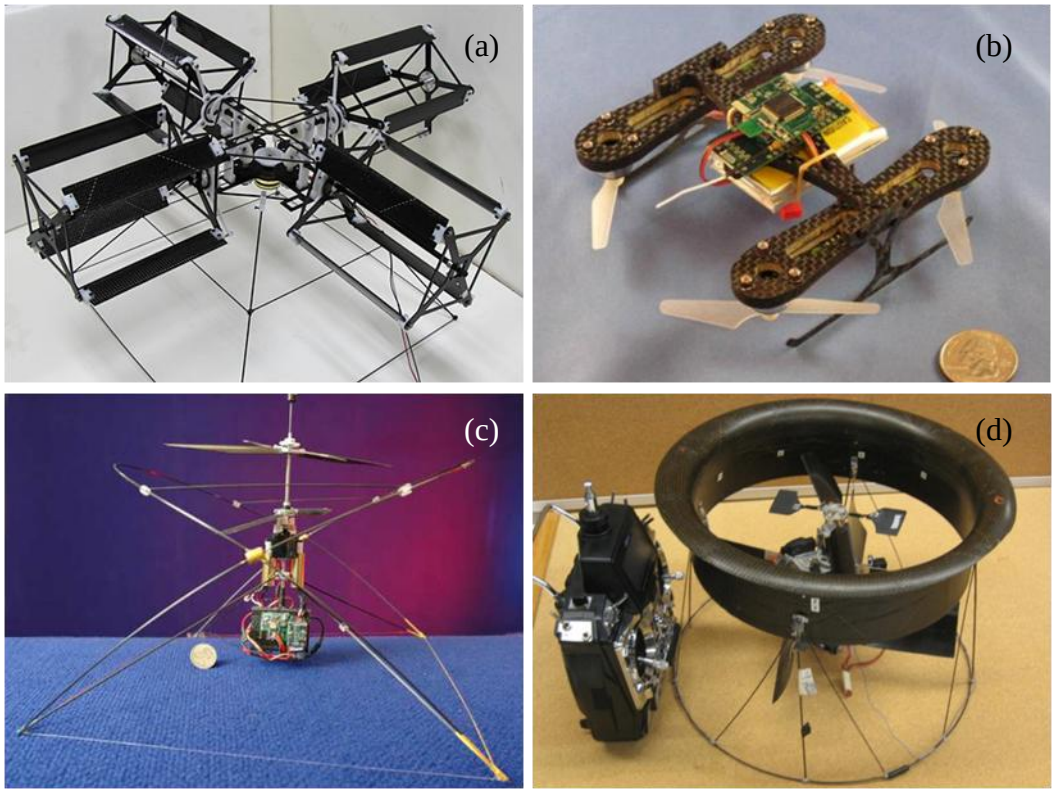

Figure 1.2: Examples of rotating-wing MAVs (a) UMD Cyclocopter, (b) Stanford's Mesicopter, (c) UMD MICOR (d) UMD TiShrov

These, and the myriad of similar commercial and research vehicles, have clearly demonstrated the viability of the rotary concept at the MAV scale, and have shown that the difficulties in generating and extending physical understanding about their efficient operation at lower Reynolds numbers (Re) than their full-scale counterparts can be overcome. Many of these rotary-wing MAV operate at Reynolds numbers on the order of

$O(10^4 - 10^5)$, however, as the design scales continue to get smaller, it is not clear whether the rotary wing understanding and models generated for $Re\ O(10^4 - 10^5)$, can be made to efficiently scale to $Re\ O(10^3)$ and below [5]. It is in this limit of low Re that flapping wings may offer not only higher efficiency than rotating designs, but better maneuverability and control. Of the trend in micro and nano-air vehicle design, Petricca et. al [6] in their review article comment: "Considering the short-term future (1–3 years from mid-2010), rotary-wing NAV will be the most important commercial type, since it has the best performing technology at present…However, in the future, flapping-wing solutions are viable and will improve maneuverability and efficiency relative to rotary NAVs."

Therefore, there is still a great need to build our understanding of extremely low Reynolds number flight aerodynamics (as well as dynamics and control) if we are to eventually build vehicles as efficient and maneuverable as the fliers seen in nature. However, the characterization of the aerodynamic environment of low Reynolds number flapping wings (this work will consider the range $Re \leq O(10^3)$ as "low Re") is complicated by a number of factors.

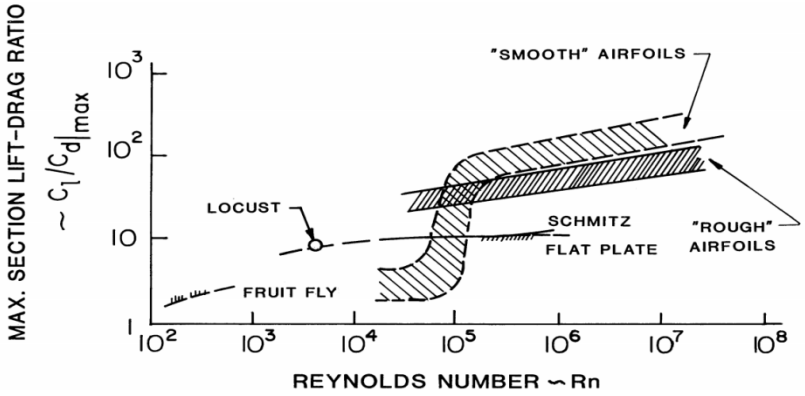

Figure 1.3: Sectional maximum L/D versus Reynolds number. Taken from [7]

1.1.2 Problems Facing Flapping-Wing Analysis

The most significant factor can be thought of as the Low Reynolds number itself. A low Re implies that the influence of the working fluid's viscous forces are *not* insignificant in comparison to the fluid's inertial forces. Physically, this results in larger boundary layers, larger vortices formed in the flowfield, larger laminar separation bubbles, and increased shear drag (profile losses). Each of these presents challenges to the practical construction of efficient low Re flight vehicles, and practical mathematical modeling of the aerodynamics. The increase in shear drag is particularly challenging, since the maximum sectional lift-to-drag ratio has been shown to drop rapidly with Reynolds number (Figure 1.3). Lower L/D equates to lower efficiency in terms of endurance and power consumption, thus maximizing this ratio becomes a critical design goal, and a great deal of research has gone into finding more optimum airfoil shapes than those traditionally used for high Reynolds number applications. It has been found that thin wings or flat plates, such as those studied by Mueller [7], perform better than the cambered or thick airfoils at moderate Reynolds numbers, and for low Reynolds numbers, thin but complex shapes have been shown to excel (e.g. [8]).

The wings of flapping insects and those used in flapping MAVs can have aspect ratios as low as 1 [9]. The tip vortices (which tend to be larger and more diffuse at lower Re) therefore affect a larger portion of the span than is typically seen at higher Re or for larger aspect ratio lifting surfaces, such as those found on rotating-wing MAVs. The induced flow created by these vortices varies in time and can have significant impacts on the lift and drag generated, even on simply translating wings [10].

Mathematically, the reduced Reynolds number increases the significance of the 2nd order viscous terms in the governing partial differential equations (PDEs). Therefore, a number of the simplifications that lead to practical solutions or approximations of the Navier-Stokes equations are either difficult to justify or formally invalid. These simplifications include computational methods such as the vortex panel method, solutions of the inviscid Euler equations, thin airfoil theory, and the thin boundary layer approximation. One benefit from a modeling perspective is that low Re flows can in many cases be considered laminar; which means that turbulent effects, which can be difficult to quantify and simulate, need not be included in certain analyses.

Another significant problem associated with flapping-wing flight analysis is the increased unsteadiness inherent in both the kinematics and the aerodynamic field. Dragonflies flap at a frequency of 40 – 50 Hz. Smaller insects, such as the Chalcid wasp, flap at frequencies of 400 Hz [11] with wing flips at the end of each half-stroke. These high flapping frequencies not only produce highly unsteady vorticity fields, but they also produce large unsteady inertial forces [12] causing deformation of the often thin membranes of insect and flapping MAV wings. This time dependency requires more complex unsteady experimental techniques (for example [13]), and more computationally expensive simulation methodologies to properly resolve. Furthermore, particularly in insect as opposed to avian flapping kinematics, the vorticity that was generated and shed into the wake during the first half of one stroke is reencountered during the second half of the stroke. Therefore, the upstream conditions that the wing sees along its stroke path are unsteady as well. Quasisteady analysis of the aerodynamics would then seem to be an inadequate methodology to predict the unsteady forces. However, when combined with

unsteady modifications to the baseline quasisteady models, quasisteady aerodynamics has found an important place as part of many modeling techniques (e,g, [9], [14]).

1.1.3 Force Production Studies on Insect Wings

Because of the complexities associated with low Reynolds number flapping wing analysis and the fascinating potential applications of an efficient mechanical implementation, these flapping conditions have received a considerable amount of attention in the literature. This includes a variety of experimental work on biological flappers ([15] – [16]), and mechanical flapping devices with specific applicability to MAV design ([5], [17], [13]). However, the following section will give a brief overview of primarily the analytical and numerical studies related to flapping-wing force production.

1.1.3.1 Analysis

Weis-Fogh [18] performed pioneering research on the force production in a variety of flapping-wing birds and insects using high speed video to dissect wing motions. His research led to two important conclusions. First, he considered the contribution of unsteady effects to the force production to be minimal, i.e. the force production could be explained almost exclusively by quasisteady analysis. Secondly, was the idea that the contact and peeling away of insect wings at the stroke endpoints, termed the "clap-and-fling", was a primary contributor to lift production. Furthermore, this clap-and-fling mechanism is an inviscid phenomenon [19], meaning viscosity was not the critical mechanism that allowed flapping insects to achieve the effectively larger lift production than steady analysis would have allowed for [20]. Lighthill [19] went on to create an

inviscid model based on this mechanism, concluding that forces should peak near stroke reversal. These predicted force peaks were experimentally observed by Spedding and Maxworthy [21] and Bennett [22]. However the Lighthill model is only applicable where a clap-and-fling exists, and not all flapping insects have strokes that include this kinematic feature. Sane [23] suggested that the clap-and-fling may not occur as a necessity in insect flight, but as a consequence of the animal simply attempting to maximize its stroke amplitude, which would maximize lift even without a clap and fling.

Ellington ([9], [11]), in his 1984 seminal series of works on the aerodynamics of hovering insect flight, concluded that the Weis-Fogh mechanism and quasisteady aerodynamics were insufficient to broadly explain the experimentally observed force time histories of many insect species. Expanding on his earlier work using a momentum theory analysis [24], Ellington proposed an expanded quasisteady vortex theory that included a blade-element analysis for the prediction of the time histories of the unsteady forces. The addition of circulatory effects (the Kramer effect) to the quasisteady analysis formed the basis for a number of subsequent models ([25] – [27]).

Dickinson, Lehmann and Sane's 1999 seminal work [14] expanded further on Ellington's modified quasisteady analysis using a dynamically scaled mechanical flapping wing pair, "Robofly". The experiments, intended to simulate a simplified *Drosophila* (fruitfly) flapping stroke, provided a broad enough parameter space to be able to identify three general mechanisms which are now widely used as a basis when discussing force production of flapping hovering wings. *Delayed stall* refers to a tendency of the leading edge vortex to remain fixed above the wing during translation, where it would otherwise be expected to peel off and cause a lift stall. *Rotational*

circulation (also noted by Ellington [9]) refers to forces generated by the wing's rapid rotation about the pitch axis at stroke reversal. Finally, *wake capture* refers to the forces generated as the wing re-encounters its shed wake from the previous half-stroke.

1.1.3.2 Computational Fluid Dynamics (CFD)

Computational studies offer a way to survey the 2D or 3D time-accurate velocity field of a flapping wing with a spatial and a temporal resolution far superior to current experimental techniques. However, because of the difficulties with mathematically solving the unsteady governing equations at low Re, only in the last 10 – 15 years have computational power and numerical methods been sufficient to efficiently model the full 3D governing equations. 2D simulations and inviscid approximations to the Navier-Stokes equations have still played an important role in building understanding and modeling experimental results. Tuncer and Platzer [8] simulated a high Re flapping airfoil ($Re = O(10^6)$) and concluded that the amplitude of the effectively inviscid forces generated at the high Reynolds number becomes significantly smaller as viscous forces become more significant (as discussed earlier). Smith et al. [28] used a 3D panel method to study the experimental flapping of a Hawkmoth. Similarly, a number of studies ([29], [30]), used vortex panel methods to study the inviscid lift generation mechanisms (e.g. the Wagner effect) on a pitching airfoil. These include a series of works conducted at the Naval Post-Graduate School specifically geared towards (e.g. Jones and Platzer [31]) developing flapping MAVs.

Liu and Kawachi [32] published the first 3D Navier-Stokes simulation of insect flapping in 1998. Their simulation modeled the vortex structure over a scaled mechanical flapping Hawkmoth [33] and showed good qualitative agreement with smoke flow

visualization. The Robofly mechanical flapping apparatus has provided a wealth of data to base 3D CFD studies around. Notable examples include studies by Sun and Tang [34] and Ramamurti and Sandberg [35]. In spite of geometric differences from the experiment, both studies found good agreement between the computed forces and published experimental data for Robofly conditions approximating *Drosophila* in hovering flight at $Re \approx 10^2$. The Ramamurti and Sandberg study employed a body fitted finite element solution to the incompressible governing equations, and the Sun and Tang study cast the Navier-Stokes equations in an inertial frame, also using a body-fitted approach.

While many CFD studies in the late 1990s and early 2000s employed body-fitted approaches, a new class of non-body-fitted methodologies have been gaining popularity for complex low Re flow analysis: the Immersed Boundary (IB) techniques. Since its formal introduction in 1972 by Peskin [36], the immersed boundary technique's promise has been explored in a variety of research areas. As will be discussed in subsequent sections, IB techniques can be efficient methodologies for low Reynolds number flows. Correspondingly, extremely low Reynolds number biological problems such as heart valve operation and arterial blood flow studies [37] have benefited from immersed boundary representations of complex and deformable body tissue shapes. In the engineering arena, detailed representations of internal combustion engine piston operation [38], flow over vehicle chassis [39], and mechanical heart valves [37] have been examined that demonstrate the potential capabilities of this still developing class of techniques. The flow simulation group lead by Mittal has published a number of studies of fish/underwater vehicle hydrodynamics [40] and human swimming [41] using this methodology. Flapping-wing flight has been studied by Vanella et al. [42], Dong et al.

[43], and Emblemsvag and Candler [44]. The next chapter will discuss the reasons that this methodology is gaining popularity in recent years, and will detail its history, implementation, and relevance to the present work.

1.2 Immersed Boundary Methods

Traditional non-immersed-boundary approaches discretize the flow domain using body-fitted structured or unstructured meshes that conform to the surface and allow precise positioning of computational nodes. In this way, physical boundaries coincide with computational boundaries allowing surface boundary conditions to be specified and extracted in a relatively straightforward manner. Combined with mesh deformation algorithms and overset methodologies, body-fitted formulations have been successfully applied to a wide spectrum of problems requiring complex bodies, deformable surfaces and unsteady motion. However, factors such as the requirement of casting the governing equations in general curvilinear coordinates, relatively large storage requirements for the mesh and the solution, mesh-to-mesh interpolation requirements in overset methodologies, and re-computation of deforming meshes can make these body-fitted mesh methods computationally expensive.

Immersed boundary (IB) techniques are any of a number of methods that spatially modify the governing flow equations in an effort to represent the influence of a body *immersed* in the flowfield. With IB methods, because the equations themselves are modified based on the shape of the immersed surface, meshes in general need not conform to the body. This carries with it a number of benefits, including the ability to forego the use of complex curvilinear meshes in favor of simple Cartesian meshes, even

for the simulation of flow over complex geometries. Although specialized applications have applied immersed boundary techniques to curvilinear meshes [45], a vast majority of implementations choose Cartesian meshes (or other orthogonal mesh types e.g. spherical or cylindrical) because of their comparative ease of generation, low storage requirements, accuracy of interpolations performed on them, and the highly efficient solution algorithms that are either optimal for or exclusive to Cartesian grid arrangements (e.g. multigrid acceleration techniques or cyclic reduction for uniform meshes). Another notable benefit is the ability to model moving or deforming bodies with a single fixed mesh. The promise of the immersed boundary technique is then the ability to model complex, deformable or moving surfaces while maintaining the advantages of simple orthogonal meshes.

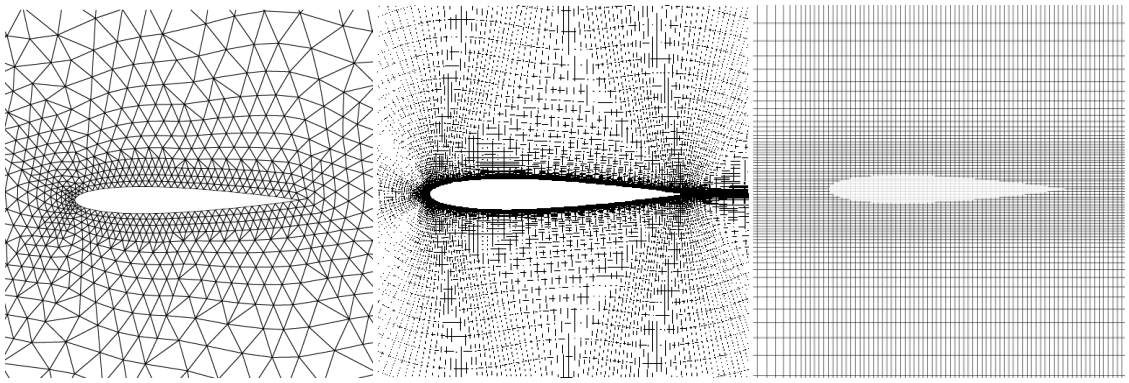

Figure 1.4: Representative meshes for NACA 0012 airfoil. l*eft:* unstructured body-fitted [45], *middle:* structured curvilinear body-fitted, *right*: Cartesian immersed boundary.

Cartesian meshes however are not optimal for all problems. For the NACA 0012 airfoil mesh in Figure 1.4 for example, it may be difficult to maintain an adequate resolution of the boundary layer for higher Reynolds number flows without significantly increasing the number of grid points. Mittal and Iaccarino [46] show that the ratio of grid size for Cartesian versus body-fitted formulations scales with $Re^{1.0}$ for 2D simulations

and $Re^{1.5}$ for 3D simulations. Furthermore, many of the additional grid points will fall either on the interior of the body or far from regions of interest where the solution is irrelevant but still must be computed. In this respect, at higher Reynolds numbers, the ability to precisely position points at the physical boundary gives body-fitted structured or unstructured meshes a significant advantage over Cartesian meshes of similar resolution. An improvement for Cartesian meshes may be to use multiple non-conformal meshes in a block or overset structure, possibly incorporating body-fitted meshes as well. However, little work is found in the literature (e.g. [47]) partially because of the computational overheads associated with intermesh communication and interpolation procedures. Similarly, Cartesian adaptive mesh refinement techniques that have the promise to blend the advantages of Cartesian meshes and body fitted techniques have seen slow progress (e.g. Durbin and Iaccarino [48]). Regardless, for many applications of low to moderate Re, the aforementioned benefits of a single Cartesian mesh in the immersed boundary framework overcome these deficiencies to make this technique a potentially attractive option.

1.2.1 Survey of Immersed Boundary Methods

With any immersed boundary technique, the ability to represent arbitrary surfaces on simple Cartesian meshes comes from a modification of the governing Navier-Stokes equations to include a forcing term, $\vec{f}$, which represents the influence of the immersed body on the surrounding fluid. Applied to the standard incompressible momentum equation:

$$\frac{\partial \vec{u}}{\partial t} = -\vec{u} \cdot \nabla \vec{u} - \nabla P + \nu \nabla^2 \vec{u} + \vec{f} \tag{1.1}$$

In a broad sense, all immersed boundary techniques can be grouped into two categories based on the method of defining $\vec{f}$, *continuous* and *direct* forcing.

1.2.1.1 Continuous Forcing

In *continuous forcing* methods, the forcing function is given as a continuous function of space and time, and may be defined at all computational nodes. In the earliest examples of immersed boundary techniques, Peskin [36] simulated the 2D fluid/structural interaction of blood flow in the heart valve system. The elastic character of the tissue walls was approximated using springs and Hooke's relation, which also allowed a direct calculation of the forcing terms necessary to impose the surface boundary conditions. A similar methodology was used by Peskin and McQueen [37] in the extension to 3D heart flow with muscular constriction. While this technique may work well for situations where surface forces are determined by Hooke's law or some similar relation, the general case (which includes stationary boundaries) requires some explicit expression for the forcing term. Goldstein et al. [49] developed a feedback relationship for quantities at the immersed surface of the form:

$$\vec{f} = \alpha \int_0^t \left[\vec{u}(t') - \vec{V}(t')\right] dt' + \beta\left[\vec{u}(t) - \vec{V}(t)\right] \tag{1.2}$$

Where $\vec{u}(t)$ is the computed surface velocity, $\vec{V}(t)$ is the known physical surface velocity and α and β are constants that determine the elastic response of the body. The expression can be thought of as a classical damped oscillator that responds to the difference between the computed velocity and the desired velocity at a given node [50]. Then, given any desired surface velocity $\vec{V}(t)$, this expression provides a method of analytically specifying the corresponding forcing function required to enforce that

velocity. Equation (1.2) has been used with some success by Saiki and Biringen [51]. The primary drawback to this method lies with the problem-dependant frequency response and damping parameters, α and β. In addition to the numerical experimentation required to minimize stability restrictions, stationary bodies require limiting values of these parameters (typically large values) which leads to a stiff numerical system. Depending on the temporal discretization of the feedback function and the specific problem under consideration, Fadlun and colleagues [50] were able to obtain a stable solution at CFL values between $O(10^{-3} - 10^{-1})$; values that are impractically small for flows that are highly unsteady or have a higher Reynolds number. Angot and colleagues [52] present a variation on the feedback idea called the *permeability* or *penalty* method, which may be obtained by setting $\alpha = 0$ and $\beta = \mu/K$. Iaccarino and Verizicco [53] show that the forcing function may then be written as:

$$\vec{f} = \frac{\nu\left(\vec{u}(t) - \vec{V}(t)\right)}{\gamma K} \tag{1.3}$$

Where γ is a reference constant based on a length scale and a reference permeability, and K is the local permeability. Within solid boundaries $K \to 0$, which results in large values of the forcing function and greater influence of the body on the flow. In the freestream, the forcing function vanishes to zero as $K \to \infty$. Again, these limiting values of K present numerical stability problems when an impermeable, stationary surface is simulated. Additionally, a smooth transition of K between the fluid and solid must be made which results in a blurring of the solid boundary. In fact, since the surface does not generally coincide with computational nodes, the simulated boundary is not sharply defined for any of the continuous forcing methods. Peskin [36] used a linear spreading of

the forcing at the boundary that extended over four computational nodes. Goldstein et al., using Equation (1.2) coupled with a spectral method, required the forcing to be spread over three to four nodes to prevent spurious oscillations. Partly in response to this, Saiki and Biringen added in a central fourth-order finite difference dissipation term to eliminate the flow oscillations allowed by the baseline spectral method. Nevertheless, their study still employed a linear blurring of the forcing function similar to that used by Peskin.

In the literature, continuous forcing methods have been shown to work well with moving boundaries where elastic deformation provides some information about the value of the forcing term. Also, the simulation of low Reynolds numbers flows approaching Stokes flow (e.g. some biological flows) allows a method of alleviating problems associated with blurred boundaries. With a relatively small number of total computational nodes in these low Reynolds number cases, the blurring is mitigated by providing finer discretization near surfaces resulting in a more exact boundary representation and a tolerable increase in computational expense. Nevertheless, it can be generally concluded that solid or rigidly deforming surfaces prove troublesome for continuous forcing approaches due to the stability restraints encountered for limiting cases of the forcing functions.

1.2.1.2 Direct Forcing

Direct forcing can be understood as a direct imposition of the solution of the discretized Navier-Stokes equations for the unknown forcing terms. At time-step *n+1*, we require that the velocity field at the surface satisfy $\vec{u}^{n+1} = \vec{V}^{n+1}$. Substituting this into Equation (1.4) and solving for the forcing:

$$\vec{f}^{n+1} = \frac{\vec{V}^{n+1} - \vec{u}^{n}}{dt} - [-\vec{u} \cdot \nabla\vec{u} - \nabla P + \nu\nabla^2\vec{u}] \tag{1.4}$$

Substituting this back into Equation (1.1) we see that the governing equations at the surface reduce to $\vec{u} = \vec{V}$. Direct forcing applies this constraint at nodes that lie on the surface and applies the Navier-Stokes equations with $\vec{f} = 0$ at all points in the flow. This apparently simple method has gained much popularity in part because it addresses the problems of ad-hoc user-defined parameters and the stability issues of continuous forcing methods. Nevertheless, as in continuous forcing, the surface generally does not coincide with computational nodes. Imposition of the condition $\vec{u} = \vec{V}$ is then carried out by an interpolation which can be made as formally accurate as the spatial discretization. Therefore, the boundaries can be enforced "exactly" within the accuracy of the scheme and thus the surfaces can be sharply defined as opposed to the diffuse boundaries encountered in continuous forcing methods.

The choice of interpolation scheme differentiates the various direct forcing methods. If no interpolation is used then the desired boundary condition is simply applied to the nearest computational node. On arbitrary bodies, this *stair-step* method produces artificial edges and a blurring of the surface (especially for staggered variable arrangements) that can potentially result in large errors near the surface, even with fine discretization. *Cut-cell* approaches remove the stair-step approximation by using a finite-volume methodology to take into account the intersected area of each cell and the boundary. In 2D, the cut area of cells in general forms a quadrilateral, around which mass and momentum conservation can be applied to yield interface velocities and pressure. While this is the only method considered that directly enforces the conservation laws, the arbitrary shape of cut cells can produce many special cases that require individual

treatment. Additionally, thin slices of cells or cells with a small volume can cause numerical stability issues and can have an adverse impact on the conservation properties of the scheme (Yang [54]). Mittal and Iaccarino [46] also noted that the extension of this methodology to 3D is a nontrivial task because of the complex polyhedral cells that arise from the surface intersected areas. Still, in 2D this cut-cell methodology has been used by Mittal et al. [55] and Quirk [56] with good results. A third interpolation scheme enforces the velocity at the surface by reconstructing the flow field at computational nodes surrounding the surface, based on the known surface velocity. This reconstruction can be of arbitrary accuracy and various interpolation stencils have been proposed for a variety of problems. Verzicco et al. [38] and Fadlun et al. [50] used a 1D linear interpolation to simulate vortex ring formation from a 2D piston/cylinder configuration. With the smoothly varying geometry of the cylinder wall, this simple interpolation proved adequate to obtain good comparison with experiment. However, for more complex bodies, higher Reynolds numbers, or situations where adequate resolution of the boundary layer may not be possible, a number of researchers have adopted higher order interpolations. Mittal et al. [55], Balaras [57], and Iaccarino and Verzicco [53] used multidimensional linear interpolation schemes to study vortex formation by Olympic swimmers, large-eddy simulation (LES) of wavy channel flow at $Re = 6{,}760$ and the airflow over a sports car, respectively.

1.3 Motivation

While there has been much research and development work towards understanding the aerodynamics that govern the force production of low Reynolds number flapping

wing flight, a detailed understanding of specifically how the flowfield affects force production mechanisms has still proven elusive, especially in the context of specific applicability to the design of biologically-inspired flapping Micro-Air Vehicles. Understanding the details of these flowfield effects can lead to improvements in efficiency in the form of lift-to-drag or lift-to-power. Therefore instead of primarily considering the stroke-averaged or quasisteady contributions to aerodynamic forces, the present work seeks to present a detailed analysis of the time-dependent forces of insect-like hovering flapping flight.

Computationally, an immersed boundary scheme presents a potentially robust framework within which to study these flapping wings. However, the relative dearth of validated immersed boundary codebases available, requires that a tailored immersed boundary solver be developed for the proposed applications. It is therefore the goal of this work to develop a baseline immersed boundary solver for the incompressible Navier-Stokes equations, capable of studying vortex dynamics at Reynolds numbers on the order of $Re = O(10^2 - 10^3)$. The rigid-body prescribed kinematics to be simulated for this work seek to provide results of broad appeal to flapping-wing aerodynamic understanding, with clearly defined parameters and in a fashion repeatable experimentally as well as computationally.

1.4 Scope and Organization of Thesis

This work is divided into two sections: The development of the Immersed Boundary Incompressible Navier-Stokes Solver (IBINS), and the application of the solver to a flapping-wing in hover.

Chapter 2 discusses the incompressible governing equations and their numerical discretization in time and space within the IBINS solver. In order to create a robust solver, IBINS offers multiple user-selectable spatial and temporal discretization schemes, and the details of their implementation as relevant to the flapping-wing proposed applications are shown. Next, the modification of the governing equations to account for the addition of a sub-grid scale turbulence model for LES computations is shown. Finally, verification and validation of the code is performed using two canonical problems to demonstrate asymptotic accuracy and spatial resolution capability.

Chapter 3 builds on the baseline solver by modifying the boundary conditions to include immersed boundaries. The boundary surface's data format and its immersion into computational space are discussed with specific regard to efficiency and accuracy. Construction of the modified spatial discretization matrix is then shown, along with the method used to extract forces from the flowfield. Finally, the immersed boundaries are combined with the baseline equations, and the solver, IBINS, is validated using simple 3D flows as baseline cases.

Chapter 4 begins the second section by focusing on the application of IBINS to a model *Drosophila* (fruit fly) wing rotation at a constant angular velocity across a range of pitch angles and for two Reynolds numbers $Re = 120$ and $Re = 1400$. After the validity of the incompressible assumption is established, the computed lift and drag are compared with experiment from the literature, and good agreement is found. It should be noted that this serves as a validation case for the flow solver. Flow structures at the wing and in the near wake are detailed. Finally power is calculated and discussed in terms of the lift-to-

power ratio. Chapter 4 serves as a baseline quasisteady case for the unsteady results of Chapter 5.

Chapter 5 discusses the application of IBINS to an idealized unsteady flapping stroke for *Drosophila* at $Re = 147$. Specific attention is given to comparing the unsteady results with the applicable quasisteady cases from Chapter 4. Over a full flapping stroke, a detailed description and visualization of the near-wake flow topology and kinematic events are given relating to the force and surface pressures observed. The force predictions are then compared against experiment, and similarities and potential causes for discrepancies are discussed. The far wake inflow distributions are visualized, again with respect to their impact on the computed lift and drag time histories. Finally for the baseline flapping case, power is computed and related to efficiency and force production.

The second portion of Chapter 5 takes the baseline flapping kinematics and modifies them by separately changing the mid-stroke pitch angle, and increasing the Reynolds number by one order of magnitude. Comparisons are made with the baseline flapping results, and with the quasisteady results. Specific attention is given to the similarities and differences in the modified kinematics from the analogous quasisteady cases from Chapter 4.

The final chapter summarizes the important conclusions and contributions of the development of IBINS and the applications of it to flapping wings in hover detailed in this work.

Chapter 2 –

Baseline Navier-Stokes Solver

As stated in the introductory chapter, one of the primary advantages of the immersed boundary technique is that practical implementation involves starting with a baseline flow solver and modifying the boundary condition routines to include the immersed boundaries. In this way, the baseline solver and its verification and implementation are essentially decoupled from the immersed boundaries, and one can use any number of well established solvers or numerical methods with the IB method. This chapter describes the implementation of the incompressible baseline solver and its verification.

For this work, the choice of baseline solver type and numerical methodologies is based on the desire to maintain simplicity, accuracy and expandability. Finite differences are used for spatial discretization since the aforementioned direct immersed boundary forcing that is applied in the next chapter is most readily applied in this form. In terms of temporal discretization, the pressure correction-type schemes (SIMPLE, PISO, etc.) have been popular choices for steady or quasisteady problems where time accuracy is not required. When time accuracy is desired with these schemes, dual time-stepping procedures may be employed, however this is computationally expensive and thus undesirable for complex unsteady processes. The pseudo-compressibility method, while allowing many of the high accuracy schemes developed for the compressible NS equations to be used for incompressible problems, also requires dual time-stepping to maintain time accuracy. The fractional step method decouples the solution of the mass

and momentum equations, and in doing so allows time-accurate solutions without sub-iterations, and thus a potentially reduced computational expense. While there are some drawbacks to the method, such as the need to solve an expensive Poisson relation, the time accuracy and flexibility to handle explicit or implicit schemes equally as well makes the fractional-step method the method of choice for the proposed applications. Furthermore, because time-accuracy is a primary requirement and turbulence production is handled using either a DNS or LES approach, it is sufficient to use only explicit schemes or semi-implicit schemes which treat the viscous terms implicitly only to remove viscous stability restrictions – potentially problematic with viscous dominated flows – thus no fully implicit schemes are considered.

Although the incompressible NS equations do not allow shocks to develop, under certain circumstances we can still expect solution gradients that are strong enough to cause oscillations and stability problems when using second order or higher differencing schemes. Experience from insect flapping simulations carried out in this work found that these oscillations begin to adversely affect stability near $Re \approx 1000$. Of course, the highly viscous nature of the low Re flows proposed for this solver introduces a level of physical dissipation that can help to control these oscillations. However, depending on the specific numerical implementation (e.g. collocated versus staggered variables, upwind versus central), these oscillations can still be problematic. The primary spatial discretization is handled using a staggered variable second order centered energy conserving approach; however Section 2.2 will briefly cover all of the spatial discretization schemes that have been implemented in the baseline solver in an attempt to minimize oscillations, maintain accuracy, and generally make the solver more robust.

Finally, the solution to the Poisson equation that arises in the fractional-step approach becomes the performance bottleneck. 60% or more of the wall-time taken for a single time step may be attributed to this portion of the solution. Therefore, a great deal of work has gone into developing and optimizing the Poisson solver to minimize the expense while keeping storage requirements reasonable (Section 2.3).

2.1 Time Integration

The governing incompressible Navier-Stokes equations for a constant viscosity, ν are as follows:

$$\frac{\partial u_i}{\partial t} = -\frac{\partial (u_i u_j)}{\partial x_j} - \frac{\partial P}{\partial x_i} + \frac{\partial}{\partial x_j}\left(\nu \frac{\partial u_i}{\partial x_j}\right) \tag{2.1}$$

$$\nabla \cdot u_i = 0 \tag{2.2}$$

where i,j = 1,2,3 and x_1, x_2, x_3 are coordinate directions. These are integrated in time by a semi-implicit fractional step method similar to that proposed by Kim and Moin [58]. The molecular viscosity, ν, may be taken out of the derivative sign for a spatially constant viscosity (the majority of cases in this work). Convection terms in the momentum equation are treated explicitly by either the second-order Adams-Bashforth scheme (AB2), or a low-storage 3rd order Runge-Kutta scheme (RK3). To remove the viscous stability limit, viscous terms are treated implicitly using the second-order Crank-Nicolson scheme (CN). For LES cases and cases where the viscous stability limit is not in danger of being violated, the equations are solved in a fully explicit manner with all terms either AB2 or RK3. The fractional step integration procedure begins by calculating a predicted velocity field, u_i*, which is evaluated without consideration of the pressure gradient term.

For the semi-implicit AB2-CN scheme, this discretization in time results in the following form of the momentum equations:

$$\Delta u_i - \nu \frac{1}{2}\Delta t \frac{\partial^2}{\partial x_j \partial x_j}\left(\Delta u_i\right) = \frac{3}{2}\Delta t \frac{\partial\left(u_i u_j\right)}{\partial x_j}\bigg|^{n} - \frac{1}{2}\Delta t \frac{\partial\left(u_i u_j\right)}{\partial x_j}\bigg|^{n-1} + \nu\Delta t \frac{\partial^2\left(u_i\right)}{\partial x_j \partial x_j}\bigg|^{n} \qquad (2.3)$$

where, $$\Delta u_i = u_i^* - u_i^n$$

For the semi-implicit RK3 formulation, this discretization results in the following form of the momentum equations:

$$\Delta u'_i - \nu \frac{1}{2}\Delta t \frac{\partial^2}{\partial x_j \partial x_j}\left(\Delta u'_i\right) = \frac{8}{15}\Delta t \frac{\partial\left(u_i u_j\right)}{\partial x_j}\bigg|^{n} + \nu\Delta t \frac{\partial^2\left(u_i\right)}{\partial x_j \partial x_j}\bigg|^{n}$$

$$\Delta u''_i - \nu \frac{1}{2}\Delta t \frac{\partial^2}{\partial x_j \partial x_j}\left(\Delta u''_i\right) = \frac{5}{12}\Delta t \frac{\partial\left(u_i u_j\right)}{\partial x_j}\bigg|^{n'} - \frac{17}{60}\Delta t \frac{\partial\left(u_i u_j\right)}{\partial x_j}\bigg|^{n} + \nu\Delta t \frac{\partial^2\left(u_i\right)}{\partial x_j \partial x_j}\bigg|^{n}$$

$$\Delta u_i - \nu \frac{1}{2}\Delta t \frac{\partial^2}{\partial x_j \partial x_j}\left(\Delta u_i\right) = \frac{3}{4}\Delta t \frac{\partial\left(u_i u_j\right)}{\partial x_j}\bigg|^{n''} - \frac{5}{12}\Delta t \frac{\partial\left(u_i u_j\right)}{\partial x_j}\bigg|^{n'} + \nu\Delta t \frac{\partial^2\left(u_i\right)}{\partial x_j \partial x_j}\bigg|^{n'} \qquad (2.4)$$

where, $$\left\{\begin{array}{l} \Delta u'_i = u_i^{n'} - u_i^n \\ \Delta u''_i = u_i^{n''} - u_i^{n'} \\ \Delta u_i = u_i^* - u_i^{n''} \end{array}\right\}$$

Superscripts refer to discrete time levels, *n* is the current time step, and predicted field values are indicated by stars. Solving either Equation (2.3) or Equations (2.4), as discussed below, gives the non-divergence-free predicted velocity field, u_i^*, at some intermediate time step between *n* and *n+1*. In order to enforce the divergence-free condition at *n+1*, as required by Equation (2.2), a pressure-like variable ϕ is introduced that obeys the following relation:

$$\frac{u_i^{n+1} - u_i^*}{dt} = -\frac{\partial \phi}{\partial x_i} \tag{2.5}$$

Note that if ϕ in Equation (2.5) is replaced by the actual pressure, *P*, then this relation is simply a rearrangement of the momentum equations in terms of the predicted velocity fields and the pressure gradient. It should be stressed however that ϕ is only a numerical quantity created to enforce continuity and does not fully correspond to any physical property of the flow [59]. Nevertheless, as has become convention in the literature, this work may often refer to ϕ as "pressure" instead of using a term such as "pseudo-pressure" as strict adherence to terminology would require. Taking the divergence of this velocity correction equation, Equation (2.5), we obtain:

$$\nabla \cdot u_i^{n+1} - \nabla \cdot u_i^* = -dt \frac{\partial^2 \phi}{\partial x_i \partial x_i} \tag{2.6}$$

The first term on the left-hand side is zero as a result of the desired divergence-free condition at *n+1*. The remaining terms constitute a Poisson equation for the field variable ϕ:

$$\frac{\partial^2 \phi}{\partial x_i \partial x_i} = \frac{1}{dt} \nabla \cdot u_i^* \tag{2.7}$$

The solution of the Poisson Equation (2.7) gives a scalar field ϕ that is finally used to determine the true velocity field at *n+1* by substitution into Equation (2.5).

2.2 Spatial Discretization

Spatial discretization on the Cartesian mesh is handled by a staggered variable finite-difference approach where scalar values are stored at a different physical location than the velocity variables (Figure 2.1). Although the standard staggered variable arrangement

requires more storage and computational time than a comparable collocated variable arrangement, it is energy conservative and tightly couples the pressure and velocity fields to prevent odd-even oscillations. Initial versions of the baseline code used the collocated variable arrangement, however for the highly unsteady flapping cases considered here, pressure-velocity decoupling and the associated oscillations resulted in high levels of inaccuracy and in many cases instability. It should be noted that attempts to mitigate these issues with artificial dissipation and specialized interpolation procedures (Rhie and Chow [60]), or multi-dimensional discretization [61] to couple the pressure and velocity fields, resulted in execution times similar to the staggered approach but without the accuracy or mathematical rigor of the staggered approach. All results presented in this work use the staggered variable versions of the code.

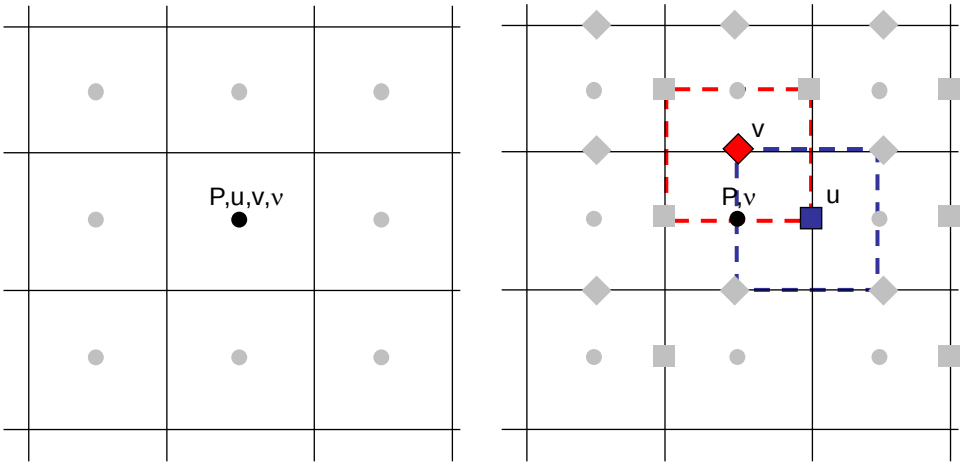

Figure 2.1: Collocated (left) versus staggered (right) variable arrangements.

2.2.1 Viscous Terms

Viscous and pressure derivatives in Equations (2.3), (2.4) and (2.7) are handled using second-order central derivatives of the form:

$$\frac{\partial^2 F}{\partial x^2} = \frac{2}{x_{i+1} - x_{i-1}} \left(\frac{F_{i+1} - F_i}{x_{i+1} - x_i} - \frac{F_i - F_{i-1}}{x_i - x_{i-1}} \right) \tag{2.8}$$

In order to facilitate the solution of Equations (2.3), (2.4) and (2.7) as described in the following section, this discretization scheme can be written in terms of coefficients of the solution variables. If we let *i*,*j*,*k* indicate computational nodes in the *x*, *y*, and *z* directions, then for the momentum equations:

$$\begin{aligned} LHS_{ijk} = {} & B_{ijk}\Delta\vec{u}_{i,j,k-1} + S_{ijk}\Delta\vec{u}_{i,j-1,k} + W_{ijk}\Delta\vec{u}_{i-1,j,k} + C_{ijk}\Delta\vec{u}_{i,j,k} + \\ & E_{ijk}\Delta\vec{u}_{i+1,j,k} + N_{ijk}\Delta\vec{u}_{i,j+1,k} + T_{ijk}\Delta\vec{u}_{i,j,k+1} \end{aligned} \tag{2.9}$$

where LHS_{ijk} is the left-hand side of Equation (2.3) or (2.4). The seven diagonals of the coefficient matrix are then:

$$B_{ijk} = -\frac{\nu \Delta t}{\left(z_{i,j,k+1} - z_{i,j,k-1}\right) \cdot \left(z_{i,j,k} - z_{i,j,k-1}\right)}$$

$$S_{ijk} = -\frac{\nu \Delta t}{\left(y_{i,j+1,k} - y_{i,j-1,k}\right) \cdot \left(y_{i,j,k} - y_{i,j-1,k}\right)}$$

$$W_{ijk} = -\frac{\nu \Delta t}{\left(x_{i+1,j,k} - x_{i-1,j,k}\right) \cdot \left(x_{i,j,k} - x_{i-1,j,k}\right)}$$

$$E_{ijk} = -\frac{\nu \Delta t}{\left(x_{i+1,j,k} - x_{i-1,j,k}\right) \cdot \left(x_{i+1,j,k} - x_{i,j,k}\right)}$$

$$N_{ijk} = -\frac{\nu \Delta t}{\left(y_{i,j+1,k} - y_{i,j-1,k}\right) \cdot \left(y_{i,j+1,k} - y_{i,j,k}\right)}$$

$$T_{ijk} = -\frac{\nu \Delta t}{\left(z_{i,j,k+1} - z_{i,j,k-1}\right) \cdot \left(z_{i,j,k+1} - z_{i,j,k}\right)}$$

$$C_{ijk} = 1 - \left(B_{ijk} + S_{ijk} + W_{ijk} + E_{ijk} + N_{ijk} + T_{ijk}\right)$$

A similar expression may be obtained for the pressure Equation (2.7) following the discretization in Equation (2.8):

$$LHS_{ijk} = B_{ijk}\phi_{i,j,k-1} + S_{ijk}\phi_{i,j-1,k} + W_{ijk}\phi_{i-1,j,k} + C_{ijk}\phi_{i,j,k} + E_{ijk}\phi_{i+1,j,k} + N_{ijk}\phi_{i,j+1,k} + T_{ijk}\phi_{i,j,k+1} \tag{2.10}$$

where LHS_{ijk} is the left-hand side of Equation (2.7). The seven diagonals of the pressure equation coefficient matrix are:

$$B_{ijk} = -\frac{2}{\left(z_{i,j,k+1} - z_{i,j,k-1}\right)\cdot\left(z_{i,j,k} - z_{i,j,k-1}\right)}$$

$$S_{ijk} = -\frac{2}{\left(y_{i,j+1,k} - y_{i,j-1,k}\right)\cdot\left(y_{i,j,k} - y_{i,j-1,k}\right)}$$

$$W_{ijk} = -\frac{2}{\left(x_{i+1,j,k} - x_{i-1,j,k}\right)\cdot\left(x_{i,j,k} - x_{i-1,j,k}\right)}$$

$$E_{ijk} = -\frac{2}{\left(x_{i+1,j,k} - x_{i-1,j,k}\right)\cdot\left(x_{i+1,j,k} - x_{i,j,k}\right)}$$

$$N_{ijk} = -\frac{2}{\left(y_{i,j+1,k} - y_{i,j-1,k}\right)\cdot\left(y_{i,j+1,k} - y_{i,j,k}\right)}$$

$$T_{ijk} = -\frac{2}{\left(z_{i,j,k+1} - z_{i,j,k-1}\right)\cdot\left(z_{i,j,k+1} - z_{i,j,k}\right)}$$

$$C_{ijk} = -\left(B_{ijk} + S_{ijk} + W_{ijk} + E_{ijk} + N_{ijk} + T_{ijk}\right)$$

2.2.2 Convective Terms

Convective terms are solved in conservative form and are discretized according to:

$$\frac{\partial F}{\partial x} = \frac{F_{i+1/2} - F_{i-1/2}}{x_{i+1/2} - x_{i-1/2}} \tag{2.11}$$

Velocity values at the midpoints are interpolated using one of three schemes. The simplest case used for a majority of the simulations is the central scheme where midpoint values are taken as the average of the surrounding nodes: $F_{i+1/2} = 0.5(F_i + F_{i+1})$. This works well for cases without strong spatial gradients, or when sufficient physical

viscosity is present to dampen numerical oscillations (e.g. in extremely low Re cases). For higher Re cases or when strong gradients are expected, a second-order limited upwind scheme is used. The form for the convective terms at the 1/2 locations is:

$$F_{i+1/2} = \tilde{F}^{low}_{i+1/2} - \varphi(\beta)\left[\tilde{F}^{low}_{i+1/2} - \tilde{F}^{high}_{i+1/2}\right] \tag{2.12}$$

Where $\tilde{(\,)}_{i+\frac{1}{2}}$ represent approximations at the i+1/2 locations, *low* and *high* refer to low and high order versions of these approximations, β is the ratio of divided differences at the i^{th} node $\beta = (F_i - F_{i-1})/(F_{i+1} - F_i)$, and $\varphi(\beta)$ is the limiter function. φ varies between 0 and 1 such that when $\varphi = 0$ in Equation (2.12) the low order approximation is used, and when $\varphi = 1$ the high order approximation is used. We arrive at a second order limited upwinding scheme by choosing the following approximations at the 1/2 locations:

$$\tilde{F}^{low}_{i+1/2} = F_i \tag{2.13}$$

$$\tilde{F}^{high}_{i+1/2} = \frac{1}{2}(F_i + F_{i+1}) \tag{2.14}$$

For a positive convective velocity, Equation (2.13) is the first order upwind approximation and Equation (2.14) is a second order approximation. Substituting these approximations into Equation (2.12), we have a second order limited upwind approximation:

$$F_{i+1/2} = F_i + \frac{1}{2}\varphi(\beta)(F_{i+1} - F_i) \tag{2.15}$$

Note that the term $(F_{i+1} - F_i)$ is the second order approximation to the slope at i+1/2. It is therefore a straightforward extension to write that for negative convective velocities the analogous second order upwind approximation is:

$$F_{i+1/2} = F_{i+1} - \frac{1}{2}\varphi(\beta)(F_{i+2} - F_{i+1}) \tag{2.16}$$

Of the limiting schemes tested with the baseline code, Van Leer's monotanized central flux limiter and Roe's "Superbee" limiter (see [62] for detailed descriptions) were able to stably convect a Kelvin-Helmholtz vortex with the least oscillations and therefore were implemented in the present versions of the code:

Van Leer:
$$\phi(\beta) = \max\left[0, \min\left(2\beta, \frac{1}{2}(1+\beta), 2\right)\right] \tag{2.17}$$

Superbee:
$$\phi(\beta) = \max[0, \min(2\beta, 1), \min(\beta, 2)] \tag{2.18}$$

For higher accuracy and potentially less numerical dissipation, the QUICK scheme implemented with variable coefficients for non-uniform meshes is also used in some simulations. QUICK is a formally third-order accurate interpolation procedure that uses a parabolic fit to three upwind nodes to approximate interface values. Referring to Figure 2.2, the coefficients of the interpolating polynomial $I(x)$ are given by the solution to the 3×3 system:

$$\begin{bmatrix} x_i^2 & x_i & 1 \\ x_{i+1}^2 & x_{i+1} & 1 \\ x_{i+2}^2 & x_{i+2} & 1 \end{bmatrix} \cdot \begin{Bmatrix} c_1 \\ c_2 \\ c_3 \end{Bmatrix} = \begin{Bmatrix} u_i \\ u_{i+1} \\ u_{i+2} \end{Bmatrix} \tag{2.19}$$

Solving for the coefficients and evaluating $I(x)$ at $x = x_{i+1/2}$ we arrive at the x-direction interpolation for a cell velocity oriented from right-to-left:

$$u_{i+1/2} \approx \frac{1}{4}\frac{2\Delta x_2^2 + \Delta x_1 \Delta x_2}{\Delta x_2(\Delta x_2 + \Delta x_1)} u_i + \frac{1}{4}\frac{(\Delta x_2 + \Delta x_1)(2\Delta x_2 + \Delta x_1)}{\Delta x_2(\Delta x_2 + \Delta x_1)} u_{i+1} - \frac{1}{4}\frac{\Delta x_1^2}{\Delta x_2(\Delta x_2 + \Delta x_1)} u_{i+2} \tag{2.20}$$

where $\Delta x_1 = x_{i+1} - x_i$ and $\Delta x_2 = x_{i+2} - x_{i-1}$. Similar expressions may be derived for other coordinate directions and cell velocity orientations.

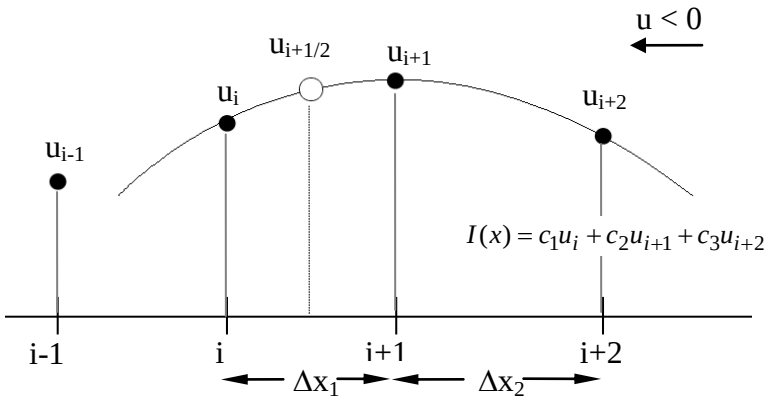

Figure 2.2: Evaluation of midpoint values using upwind QUICK scheme.

Despite its formal accuracy, the QUICK scheme typically converges in a second-order manner and differences in the solution between QUICK and second-order central convective discretization are typically small [63]. However, QUICK interpolations can help damp gradient-induced oscillations. As an example, in Figure 2.3 we see a velocity profile taken across the center of a developing Kelvin-Helmholtz vortex forming in a free shear layer. Although the location of the peak velocity is captured by the central scheme, the oscillations in the solution are non-physical and may eventually grow without bounds. The second-order upwind scheme coupled with a Van Leer limiter, Equation (2.17), is non-oscillatory but highly dissipative. The upwind QUICK scheme in this case is able to capture the peak velocities while also preventing oscillations.

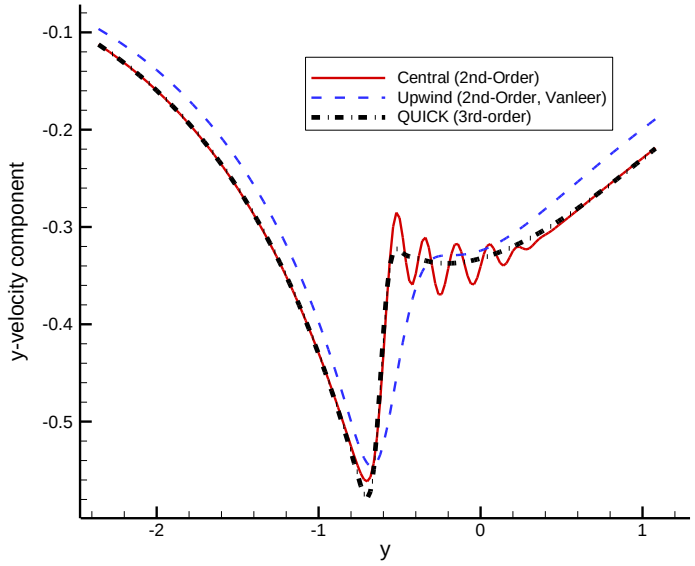

Figure 2.3: Velocity profiles through center of developing Kelvin-Helmholtz vortex. Comparison of convective discretization schemes.

2.3 Poisson and Momentum Equation Solution

Typically, the solution of the Poisson equation for ϕ is the most computationally expensive portion of the fractional step algorithm. In 2D, Equation (2.7) is solved using the incomplete LU decomposition of Stone [64], termed the Strongly Implicit Procedure (SIP). The extension of SIP to 3D developed by Zedan and Schneider [65] is used to solve the 3D Poisson equation. Although the popularity of SIP as applied to the solution of the pressure equation has waned in light of efficient multigrid and conjugate-gradient procedures, it offers reasonably uniform and rapid convergence for a wide variety of boundary conditions, and most importantly, is readily implemented in a parallel multi-block solver, unlike multigrid approaches. SIP requires that the Poisson equation be represented by second-order central finite differences and that the solution is elliptic in

nature (i.e. relatively smooth). The discrete Poisson equation for $\vec{\phi}$ may then be written as

$$[A]\cdot\vec{\phi}=\vec{b} \tag{2.21}$$

where $\vec{b}$ is the right-hand-side of Equation (2.7) and [*A*] is a 7-diagonal banded matrix in 3D given by the equation's coefficients. The standard LU decomposition would exactly split [*A*] into the product of a *dense* lower and *dense* upper triangular matrix. It is well known that $O(N^3)$ operations are required to construct the triangular matrices by Gaussian elimination and $O(N^2)$ operations are required each time the system is solved. This cost is greatly reduced if [*A*] is *approximately* decomposed into the product of *banded* lower and upper triangular matrices, M_l and M_u.

$$[M_u M_l]\cdot\vec{\phi}=\vec{b} \tag{2.22}$$

In the Zedan and Schneider 3D SIP scheme, the product of the approximations M_u and M_l is a 19-diagonal banded $N\times N$ matrix as opposed to a 7-diagonal matrix for the exact decomposition. Stone's 2D SIP decomposition results in a 7-diagonal banded matrix as opposed to a 5-diagonal matrix for the exact computation. The SIP procedure is a specification of the elements of M_u and M_l with an additional parameter used to modify the assumption of an elliptic solution and affect the convergence rate. For the results presented in this work, the parameter is fixed between 0.89 – 0.92. The Zedan and Schneider scheme is modified slightly in the present implementation to account for non-uniform meshes.

Because the approximately decomposed matrices M_u and M_l are triangular and banded, inverting them to obtain the pseudo-pressure field is a trivial matter of forward and then backward substitution. Provided that the number of iterations is small, a factor

determined by the smoothness of the final solution, the efficiency of this iterative scheme is often quite good compared with SOR or ADI schemes. The values of the diagonals of M_u and M_l in terms of the coefficients in Equation (2.7) and further details of the method may be found in Ferziger and Perić [63].

As a result of the implicit Crank-Nicolson scheme, the computation of the predicted velocity field from Equations (2.3), (2.4) and (2.7) requires a matrix inversion for each coordinate direction. Although these equations are hyperbolic in nature, they still may be expressed as in Equation (2.21) and thus SIP is still used to perform the required inversion. In this case, $\vec{\phi}$ is replaced by each velocity component and the vector $\vec{b}$ is the right-hand side of Equation (2.9). The strongly diagonally dominant discretization matrices allow convergence to be reached in 4 – 5 iterations, whereas the solution to the Poisson equation may require 20 or more iterations for a 3 order-of-magnitude reduction in the residual. Typically, the problems examined in this work require approximately 50 Poisson iterations to converge 5 orders of magnitude.

2.4 Boundary Conditions (for non-IB boundaries)

Unless otherwise noted, Neumann, Dirchlet and periodic boundary conditions are implemented using standard first-order approximations. In the external flow problems, velocities at the inflow are set to the free stream values and their time derivatives are set to zero:

$$\begin{aligned} u_{\text{inflow}} &= u_{\text{inf}} \\ \Delta u_{\text{inflow}} &= 0 \end{aligned} \tag{2.23}$$

The pressure variable is set to a zero gradient normal to all computational boundaries.

$$\left.\frac{\partial P}{\partial n}\right|_{boundary} = 0 \tag{2.24}$$

As an exception, in external problems the outflow velocities and pressure are predicted using the one-dimensional linear advection equation normal to the boundary:

$$\frac{\partial \gamma}{\partial t} = -C\frac{\partial \gamma}{\partial n} \tag{2.25}$$

Although this hyperbolic equation is not strictly applicable for viscous elliptic problems, this relation provides a reasonable estimate of flowfield behavior provided that the advection velocity *C* is chosen appropriately. Using a second-order DuFort-Frankel discretization of the above equation, Orlanski [66] derived an expression for *C* that has become popular enough that the use of any choice of advection speed and discretization is often referred to as an *Orlanski* boundary condition. Alternate forms of *C* and the spatial/temporal discretization may however be required for stable solutions in various problems. The present code applies first-order forward differencing in time, second-order backwards differencing in space and the local velocity normal to the boundary at the first interior node as the advection velocity. For a uniform mesh the result is:

$$\frac{(\gamma_b^{n+1} + \gamma_b^n)}{\Delta t} = -(u \cdot \hat{n})_{b-1}\frac{\frac{3}{2}\gamma_b^n - 2\gamma_{b-1}^n + \frac{1}{2}\gamma_{b-2}^n}{\Delta s} \tag{2.26}$$

where γ is a flow property, *b* is the boundary index, and Δs is the uniform mesh spacing normal to the boundary. γ at the boundary at the new time step *n+1* can then be explicitly calculated from Equation (2.26).

2.5 Turbulent SubGrid-Scale (SGS) Modeling

For most of the low Reynolds number problems that the code developed in this work is designed to simulate, $Re < 1000$, the flow may either be considered to be laminar, or the smallest length scales of turbulence, η (the Komolgorov scale), are large enough that they can be directly computed without incurring a significant computational cost in terms of storage or time. However, as we increase Re, the mesh count required to adequately resolve the Komolgorov scale grows proportionate to $Re^{9/4}$ and the number of time steps required grows as $Re^{3/4}$. As an example, the meshes used to compute the $Re = O(10^2)$ unsteady problems in the first part of Chapter 5 required $N \approx 30 \times 10^6$ nodes to resolve the flow and required 20000 time steps to reach a periodic solution. An order of magnitude increase in Reynolds number would require $10^{2.25}N \cong 5 \times 10^9$ nodes, and $10^{0.75}(20000) \cong 1 \times 10^5$ time steps for a converged solution.

In order to avoid these large computational expenses for the present simulations, the preceding Navier Stokes solution can be extended to become a Large Eddy Simulation (LES) solver. Here, the effect of the smallest scales of turbulence are modeled explicitly based on the assumption that the smallest energy carrying turbulent eddies behave in a statistically determinant fashion that is decoupled from the large scale turbulence. The LES technique chosen for this work is a simple Dynamic Smagorinsky SubGrid Scale (SGS) model.

In order to apply the model, the spatially filtered form of Equation (2) may be expressed:

$$\frac{\partial \overline{u}_\iota}{\partial t} = -\frac{\partial(\overline{u}_\iota \overline{u}_j)}{\partial x_j} - \frac{\partial \bar{P}}{\partial x_i} + \frac{\partial}{\partial x_j}\left(\nu \frac{\partial \bar{u}_i}{\partial x_j}\right) - \frac{\partial \tau_{ij}}{\partial x_j} \tag{2.27}$$

Where the overbar denotes a spatially filtered variable, and τ_{ij} is the subgrid scale stress tensor:

$$\partial\tau_{ij} - \frac{1}{3}\tau_{kk}\delta_{ij} = -2\nu_T\bar{S}_{ij} = -2\nu_T\left[\frac{1}{2}\left(\frac{\partial\overline{u_i}}{\partial x_j} + \frac{\partial\overline{u_j}}{\partial x_i}\right)\right] \tag{2.28}$$

where ν_T is the turbulent eddy viscosity. Substituting Equation (2.28) into (2.27) we arrive at:

$$\begin{aligned}\frac{\partial\overline{u_\iota}}{\partial t} &= -\frac{\partial(\overline{u_\iota}\overline{u_J})}{\partial x_j} - \frac{\partial\left(\bar{P} + \frac{1}{3}\tau_{kk}\right)}{\partial x_i} + \frac{\partial}{\partial x_j}\left(\nu\frac{\partial\bar{u}_i}{\partial x_j}\right) - \frac{\partial\tau_{ij}}{\partial x_j} \\ &= -\frac{\partial(\overline{u_\iota}\overline{u_J})}{\partial x_j} - \frac{\partial(\bar{P}_{total})}{\partial x_i} + \frac{\partial}{\partial x_j}\left(\nu\frac{\partial\bar{u}_i}{\partial x_j}\right) + \frac{\partial}{\partial x_j}\left(\nu_T\frac{\partial\bar{u}_i}{\partial x_j}\right) \\ &\quad + \frac{\partial}{\partial x_j}\left(\nu_T\frac{\partial\bar{u}_j}{\partial x_i}\right)\end{aligned}$$

$$\frac{\partial\overline{u_\iota}}{\partial t} = -\frac{\partial(\overline{u_\iota}\overline{u_J})}{\partial x_j} - \frac{\partial(\bar{P}_{total})}{\partial x_i} + \frac{\partial}{\partial x_j}\left(\nu_{total}\frac{\partial\bar{u}_i}{\partial x_j}\right) + \frac{\partial}{\partial x_j}\left(\nu_T\frac{\partial\bar{u}_j}{\partial x_i}\right) \tag{2.29}$$

where $\bar{P}_{total} = \bar{P} + \frac{1}{3}\tau_{kk}$, which is a scalar term that can be solved for in the same manner as was $\bar{P}$, and $\nu_{total} = \nu + \nu_T$ behaves similarly to ν in the unfiltered governing equation. The turbulent eddy viscosity can be computed in a number of ways, but for the Dynamic Smagorinsky Model (DSM) a second more coarse filtering of the governing equations is performed, called the *test filter*, of width h_t. The original filter is referred to as the *grid filter*, and has a filter length h. Then the DSM value for ν_T is:

$$\nu_T = C(\vec{x})\Delta^2|\bar{S}_{ij}| \tag{2.30}$$

Where the Smagorinsky parameter C is chosen based on a scale similarity assumption and $\Delta = \sqrt[3]{\Delta x\Delta y\Delta z}$ for each grid cell. A detailed derivation of a simple model for $C(\vec{x})$ is given in Bernard and Wallace [67], the final result of which is given here:

$$C(\vec{x}) = \frac{1}{2}\mathcal{L}_{ij}M_{ij}/M_{ij}^2 \tag{2.31}$$

where $$M_{ij} = h^2\langle|\bar{S}_{ij}|\bar{S}_{ij}\rangle - h_t^2|\bar{S}_{ij}|\langle\bar{S}_{ij}\rangle$$

and $$\mathcal{L}_{ij} = \langle\overline{u}_i\overline{u}_j\rangle - \langle\overline{u}_i\rangle\langle\overline{u}_j\rangle$$

Angled brackets indicate test filtered quantities. In order to ensure numerical stability, ν_{total} is forced to always remain positive by artificially increasing the value of $C(\vec{x})$ where it is found to be negative. This procedure is reported to work well when the flow is only weakly turbulent, and thus not prone to large areas where C may be negative [68].

It should be noted that only the results of Section 5.3 use the above LES formulation. All other simulations in this work solve Equation (2) directly.

2.6 Solver Parallelization

The solver is parallelized by block decomposition of the global Cartesian mesh. Given the number of desired divisions of the global mesh in the x, y and z directions, the code attempts to split the domain such that the number of nodes in each block is nearly uniform. This load balancing minimizes the time that processors have to wait to continue if their next computations are dependent on another processor which has a larger number of nodes and thus take longer. It should be notes that for the immersed boundary computations, this simple node count load balancing does not necessarily minimize wait time, since the number of immersed boundary nodes in each block can have a significant impact on the number of computations that need to be performed per block. Nevertheless, since splitting can be performed in any of the 3 coordinate directions, one should attempt to choose a direction that minimizes the number of nodes along a boundary. For example,

a 10×10×100 mesh should be split in the z direction (100 nodes at an interface plane), not along x or y planes (1000 nodes at an interface plane).

Communication between blocks is handled explicitly using a 2 row overlap region. This overlap is large enough to accommodate the computational stencils described previously without requiring reduced order across boundaries. Information is passed across blocks after each after each time step, after each iteration of the pressure Poisson iterative solver, and for semi-implicit formulations after each iteration of the calculation of the velocity prediction equation. This information includes all scalars (P, ν), velocity, and immersed boundary parameters.

Machine level inter-processor communication is implemented using the MPI standard, and MPICH2 libraries.

2.7 Verification and Validation

In the final portion of this chapter, the baseline solver described above is verified by computing the solution to simple canonical problems. The accuracy of the viscous terms is verified by comparison with an exact solution for decay of a stationary vortex lattice. The convective terms are validated by computing a 2D flow in a square cavity. Finally, the LES implementation is validated by computing the decay spectrum of an isotropic turbulence field.

2.7.1 Taylor-Green Vortex Lattice

The Taylor-Green vortices are a divergence-free infinite array of quasi-2D counter-rotating vortices whose strength decays exponentially according to the following exact solution for the velocity and pressure fields (for $Re = 1.0$):

$$u_x(t) = -e^{-2t}\cos(x)\sin(y)$$

$$u_y(t) = e^{-2t}\cos(y)\sin(x) \tag{2.32}$$

$$P(t) = -\frac{1}{4}e^{-4t}[\cos(2x) + \cos(2y)]$$

The vortices are stationary, meaning that convective terms should sum to zero in this model problem, thus the results primarily verify the accuracy of the viscous and pressure terms. The square 2D computational domain is 2π in length and is uniformly discretized into $N \times N$ nodes. Periodicity is enforced using the boundary condition specification of a row of ghost-cells outside of the domain in each direction. The exact solution to Equations (2.32) at $t = 0$ is given as an initial condition and the flow is allowed to evolve until $t = 5.0$ at a fixed time step of $\Delta t = 0.005$. The velocity residual is reduced by 10 orders of magnitude while the number of SIP iterations for pressure is fixed at 25. This results in a pressure residual drop of at least 3 orders of magnitude (for this model problem). Note that although this problem is 2D, the solution is obviously valid in any coordinate plane (not just the X-Y plane). Therefore, as was done but not shown here, one can readily verify the 3D solver with this 2D problem.

As seen in Figure 2.4, the computed velocity and pressure magnitude decay are in excellent agreement with the analytical solutions at all simulated times. The L2-norm of the velocity magnitude error (Figure 2.5a) and pressure magnitude error (Figure 2.5b) are plotted at $t = 2.5$. The velocity error decay confirms that the spatial accuracy of the velocity discretization scheme is approximately second-order accurate. The L2-norm of the pressure error similarly shows an asymptotically second-order accurate reduction with mesh refinement.

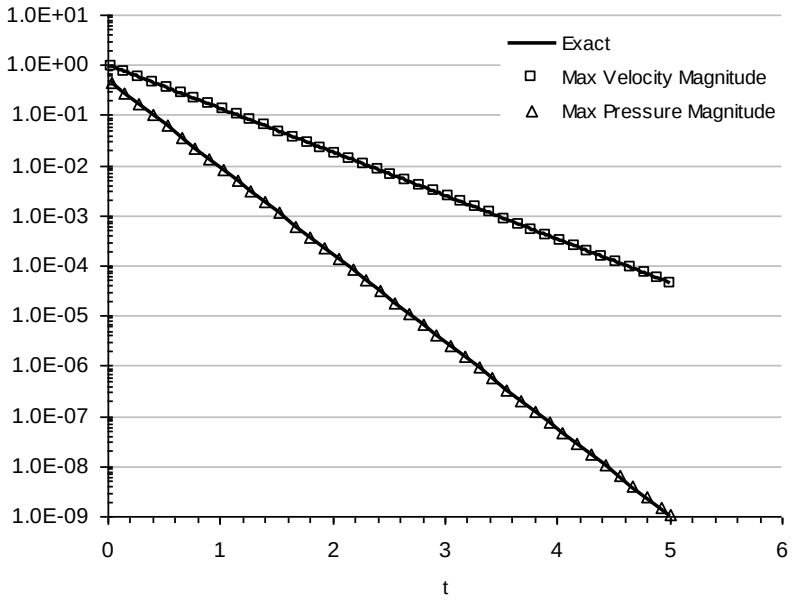

Figure 2.4: Computed and exact maximum velocity and pressure magnitude decay for Taylor-Green vortices.

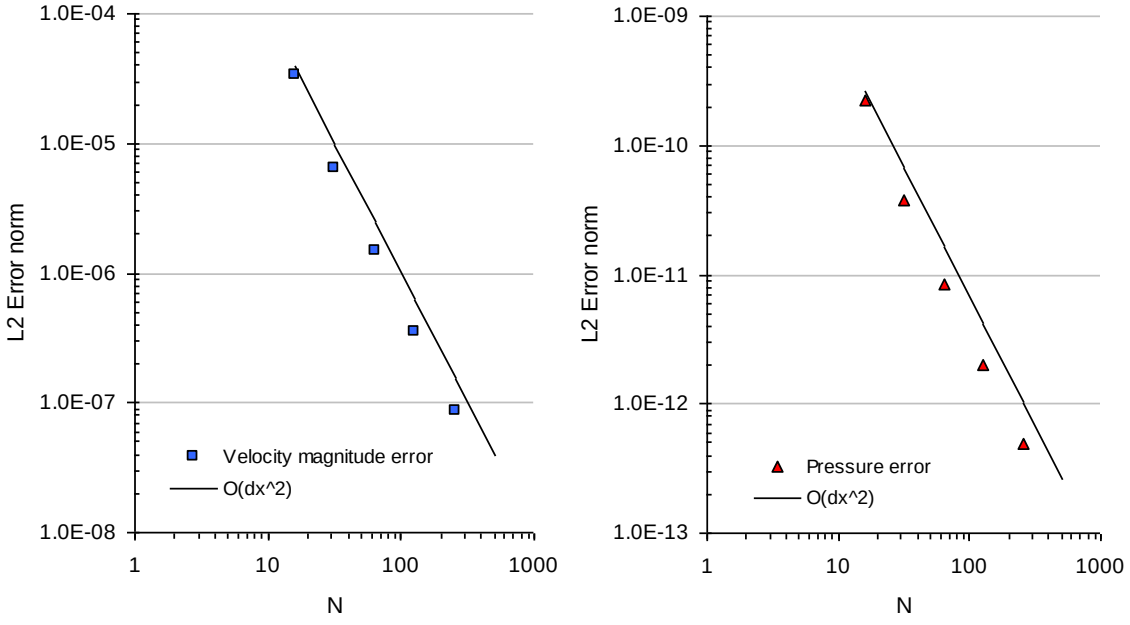

(a) (b)

Figure 2.5: Reduction in L2 error norm with grid refinement demonstrating second-order spatial accuracy for (a) velocity (b) pressure.

2.7.2 Lid-Driven Square Cavity

Convective terms are verified by simulating the steady vortex formation in a square lid-driven cavity at Re = 100, 1000 and 3200, based on cavity dimension and lid velocity. For the Reynolds numbers tested, this flow is characterized by a steady primary vortex and up to three secondary vortices that develop in the cavity corners (Figure 2.6). Although experimental results for this configuration are difficult to obtain, numerous high resolution computational studies are available for this standard test problem (e.g. [69], [70]). Dirchlet velocity boundary conditions and a zero ϕ gradient are enforced on all boundaries (Figure 2.6). In this case, in order to minimize numerical diffusion of the secondary vortices near the walls, the ϕ gradient is enforced using a second-order one-sided difference approximation. The field is initialized with a circular vortex centered at the geometric center of the cavity, after which the flow is allowed to evolve with CFL = 0.25 until the separation and attachment points of the secondary vortices along the walls remain fixed. This is noted to occur by a nondimensional time of t = 15 for Re = 100 – 1000, and t = 20 for Re = 3200.

Erturk et al. [69] report that a uniform mesh of 129×129 for their second-order streamfunction-vorticity solver was sufficient to obtain a mesh resolved steady solution for Re = 1000 – 5000. Similar results are found with the present algorithm, as demonstrated by the velocity profiles taken at the geometric center of the cavity which are compared to the computations of Ghia et al. [70]. In general, for the 129×129 mesh, the agreement is excellent at all simulated Reynolds numbers (Figure 2.7). At Re = 3200, the 129×129 mesh results appear to more closely follow the Ghia et al. data than the finer 257×257 mesh. This, however, is most likely because the comparison data were obtained

on a 129×129 mesh (with a scheme of similar accuracy) thus the finer mesh used in the present study probably gives a more accurate representation of the grid-converged solution. Although not presented in full here, the size and locations of the separation and attachment points associated with the secondary vortices for all Reynolds numbers tested are in good agreement with both Erturk et al. and Ghia et al. predictions. As a sample, these results for *Re* = 1000 are presented in Figure 2.8 where the two secondary vortices have been magnified for comparison.

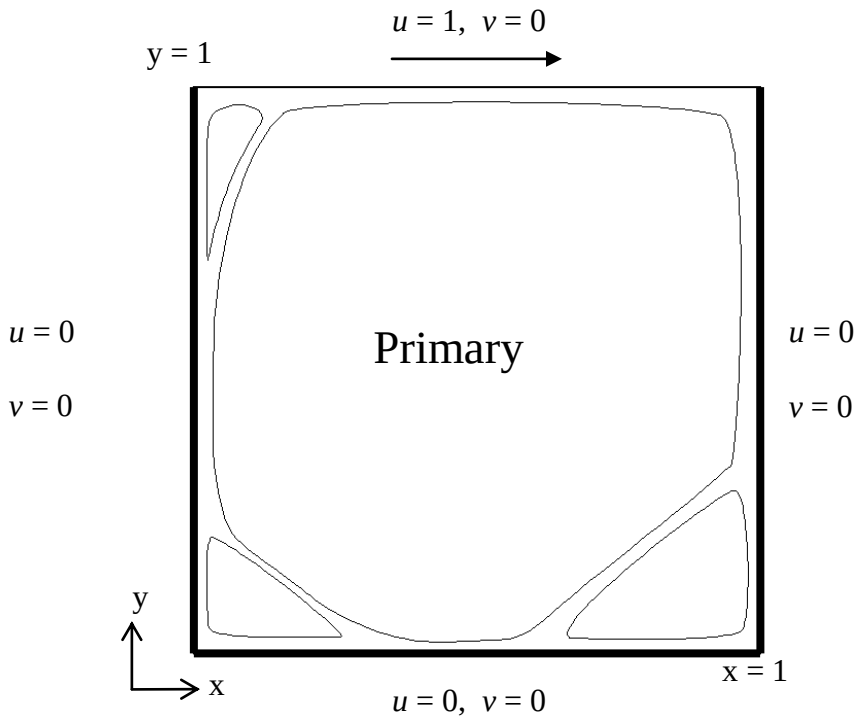

Figure 2.6: Lid-driven cavity problem schematic.

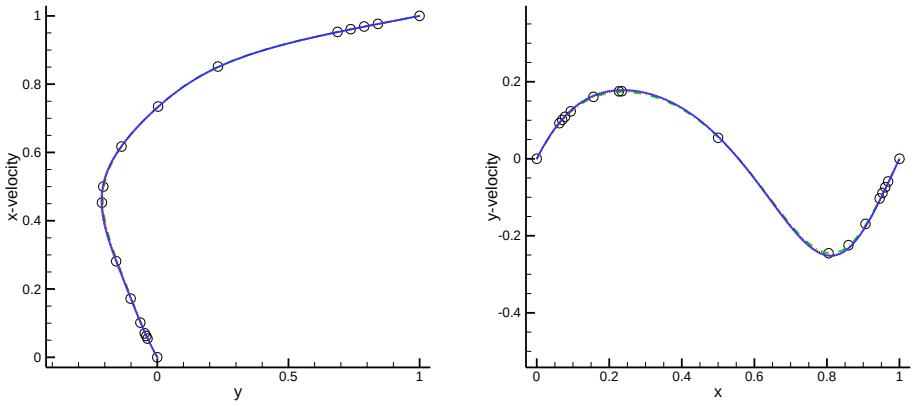

(a) Re = 100

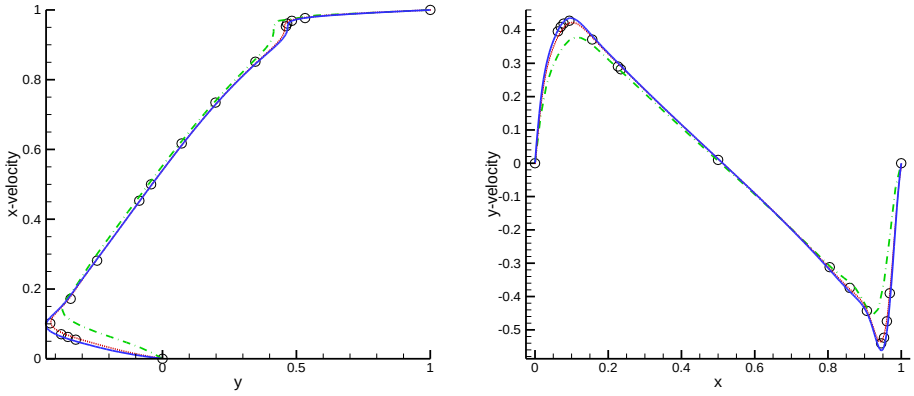

(b) Re = 1000

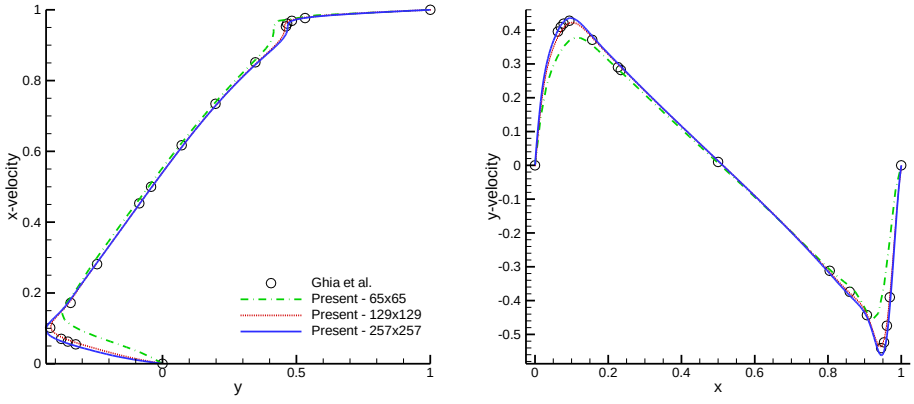

(c) Re = 3200

Figure 2.7: Computed velocity profiles at geometric center of cavity for 65×65, 129×129 and 257×257 mesh resolutions. Comparisons with computations of Ghia et al. [70].

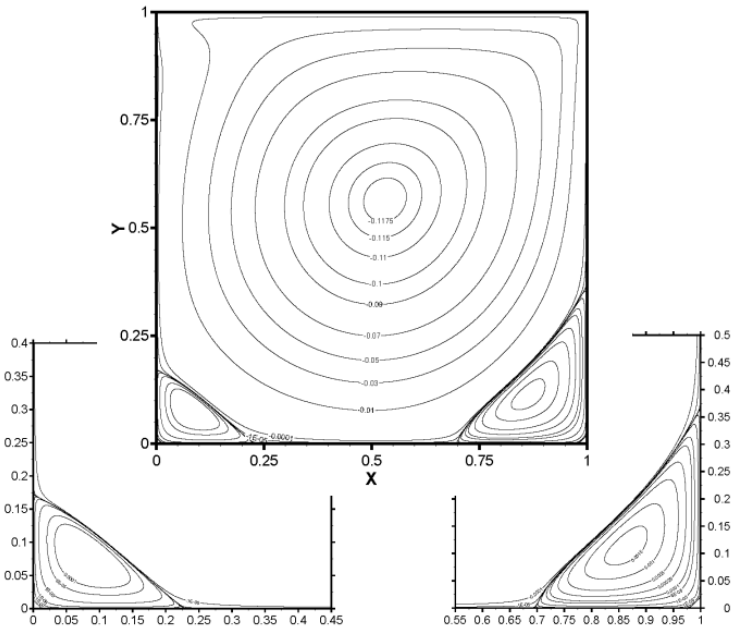

(a)

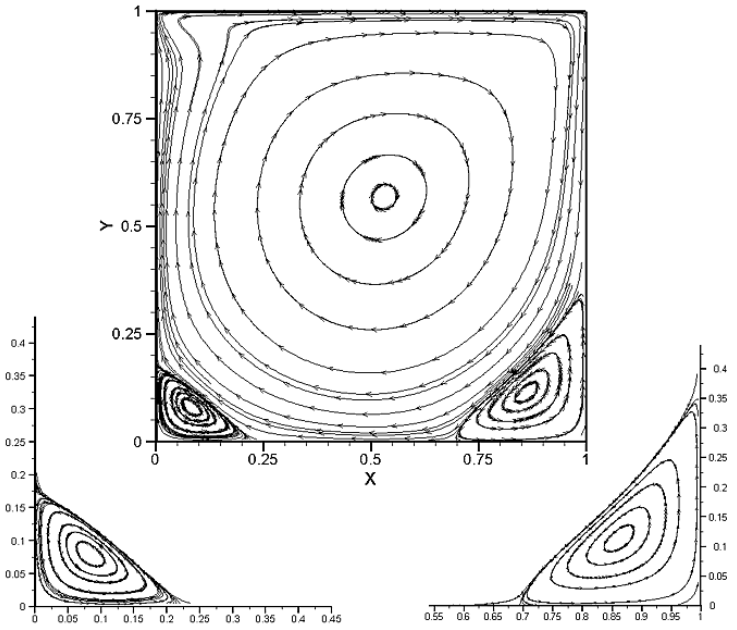

(b)

Figure 2.8: Streamlines for cavity flow at Re = 1000 from (a) Erturk et al. [69] (b) present results. Secondary vortices are magnified for comparison

2.7.3 Isotropic Turbulence

To validate the Dynamic Smagorinsky LES model implementation, an initial periodic field of isotropic turbulence is generated, and the rate of energy decay is computed and compared against high resolution spectral results in the literature.

In order to observe realistic energy decay in the turbulent field, it is ideally necessary to specify all of its single point statistics such as K and ϵ, as well the autocorrelations and infinitely many higher order moments at the initial time [67]. As this is not possible, the present validation study adopts the method employed by Rogallo [71] and Mansour and Wray [72] which specifies random velocities having a prescribed initial energy spectrum of the form (in wave space):

$$E(\kappa) = \frac{q^2}{2A}\frac{1}{\kappa_p^{\sigma+1}}\,\kappa^{\sigma}\exp\left[-\frac{\sigma}{2}\left(\frac{\kappa}{\kappa_p}\right)^2\right] \tag{2.33}$$

Where κ is the wave number, $q^2 = 3$, $\sigma = 6$, $A = (5/432)\sqrt{(3\pi)}$ and $k_p = 10$. While not statistically realistic, this permits the clustering of energy around a desired wave number (k_p) such that after some simulation time, a statistically valid isotropic turbulent condition should arise. The Taylor microscale, λ, characterizes the size of eddies in transition between the inertial subrange and the dissipation range. Based on the turbulent kinetic energy E and the dissipation ε we can define $R_\lambda = \sqrt{20E^2/3\nu\varepsilon}$ as the Reynolds number based on λ. This Reynolds number should monotonically decrease with simulation time. As shown in Figure 2.9, for $\nu = 0.001$, this occurs sear a non-dimensional time of $t = 4.5$. The validation simulations are run to $t = 10.0$, which is well within the monotonic decrease regime, and therefore represent valid turbulent conditions.

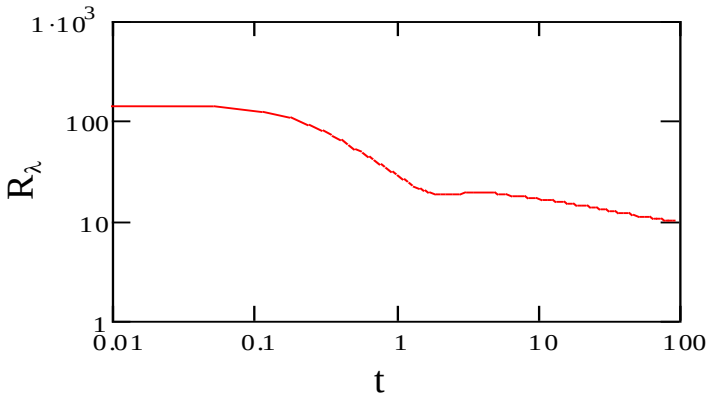

Figure 2.9: Turbulent Reynolds number decay in isotropic turbulence field for $\nu = 0.001$.

Using these initial conditions, the simulation is performed using the baseline non-LES solver in a cube of length 2π using a uniform mesh with $N = 128^3$ points in each direction. In Figure 2.10 the 1D energy spectrum, turbulent dissipation rate, and turbulent kinetic energy of the present solver, IBINS, are compared against the spectral results of Rogallo [71]. The energy spectrum results are in good agreement even in the higher wave numbers, and the magnitudes and decay rates of both kinetic energy and dissipation also compare well. These DNS results indicates that for these conditions, the 128^3 mesh is sufficient to resolve the Taylor microscale without any explicit turbulence modeling. However, as stated in section 2.5, as the Reynolds number increases, a finer mesh is required to adequately capture the turbulent energy scales in the flowfield.

Another way to view the problem is for a fixed Reynolds number, the mesh cannot become coarser than a certain value and still adequately resolve the turbulent scales. In Figure 2.11a, the above simulation is repeated on a coarser mesh $N = 64^3$. The baseline solver shows excess energy buildup in the higher wave numbers. The energy cascade from larger to smaller scales is not being properly predicted because the smallest scales

are not being resolved. However, when the dynamic Smagorinsky model is enabled, the energy again is in good agreement with literature. Similarly, in Figure 2.11b, the mesh is coarsened again to $N = 32^3$. The baseline solver shows a large buildup of turbulent energy, and very little dissipation with increases in wave number. In a simulation, this type of energy buildup not only leads to inaccurate results, but potential instabilities as well. With the dynamic Smagorinsky model enabled in the present solver, Figure 2.11b shows that the energy cascade is in much better agreement with the high order spectral DNS results, even on this coarse mesh.

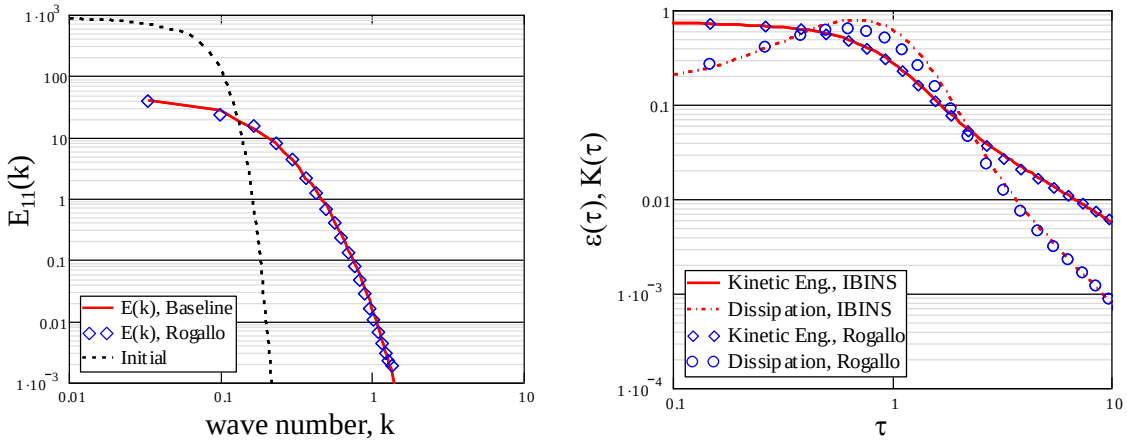

Figure 2.10: 1D Energy Spectrum (left), turbulent kinetic energy K (right) and turbulent dissipation rate, ε (right) compared with Rogallo [71] at $t = 10$, $\nu = 0.001$. Uniform mesh size $N = 128^3$.

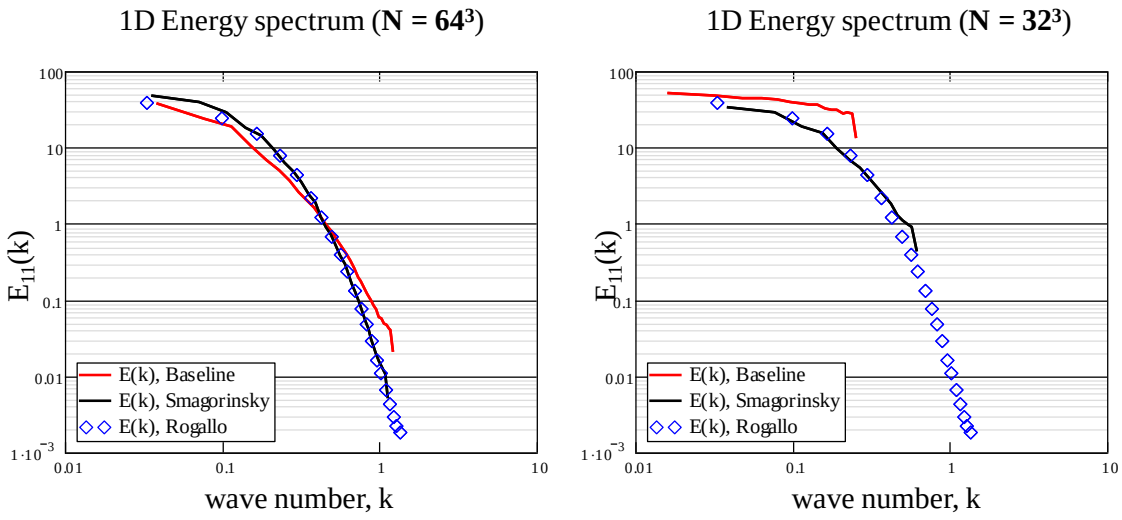

(a) (b)

Figure 2.11: 1D energy spectrum for baseline solver and solver with the dynamic Smagorinsky model enabled, compared against the Rogallo results for (a) $N = 64^3$ and (b) $N = 32^3$.

2.8 Summary

This chapter described the implementation of the baseline Navier-Stokes solver. In choosing the numerical schemes, care was taken to optimize for relevance to incompressible, low Reynolds number, unsteady aerodynamic applications. Time integration is performed using a second order fractional step method. Spatial discretization uses either a 2nd order central scheme or, for cases with sharp gradients that may affect solution stability and accuracy, 2nd or 3rd order upwinded convective schemes with viscous terms always handled with 2nd order central discretizations. The Poisson solution is carried out using an efficient approximate LU decomposition method. For cases where turbulent scales require more spatial or temporal resolution than can

practically be handled by the baseline DNS solver, a simple dynamic Smagorinsky method is added. The entire baseline code is block parallelized using MPICH2 libraries.

Finally, the baseline code is verified using the exact solution to a 2D vortex field, and validated with the solution to the canonical lid-driven cavity problem. The dynamic Smagorinsky model is validated by demonstrating that the proper energy cascade is recovered on meshes too coarse to recover the energy spectrum without modeling the sub-grid-scale eddies.

Chapter 3 –

Immersed Boundary Methodology

The proposed applications of the code developed in this work primarily focus on external flow at low Reynolds numbers ($Re \leq O(10^3)$) with unsteady free stream and surface boundary conditions. Additionally, although not currently implemented, the surfaces may be required to deform as a result of inertial or aerodynamic forces. As recent work has demonstrated (Mittal et al. [55], Balaras [57], Iaccarino and Verzicco [53]), a flexible immersed boundary approach that meets these requirements is a direct forcing scheme with the boundary properties imposed using a surface reconstruction method. For unsteady conditions, continuous forcing schemes, as discussed in Chapter 1, may exhibit stability restrictions that would require a prohibitively small CFL number. Large scale flow physics may be captured reasonably well by either continuous or direct forcing, however the sharp interface allowed by direct forcing methods also may allow a better description of small scale near-body phenomena. Direct forcing schemes can more readily handle moving surfaces than continuous forcing schemes handle stationary surfaces. For the proposed application to flapping-wing flight, where sharply defined moving boundaries form the bulk of the applications, the choice of a direct forcing method is therefore clear. In the context of direct forcing schemes, Fadlun et al. [50] provide a comparison of results obtained from simple cases of the stair-step, cut-cell and reconstruction interpolation schemes. Although only 1D linear interpolations are used for their 2D test cases, they find that only the field reconstruction method properly maintains

the asymptotic accuracy of the discretization scheme at the surface. This conclusion, while not rigorous, provides additional incentive to move towards implementing a direct forcing reconstruction scheme.

A primary advantage of the direct forcing schemes is that in practice, the governing equations are not modified at all; the enforcement of $u = V$ (required velocity at the boundary equals velocity at the boundary surface) comes in only as a boundary condition. Then, since no additional time dependant terms are added to the momentum equations, deformable or moving surfaces are more readily handled. An upshot of this is that direct forcing methods are relatively easy to integrate into any given baseline solver. A majority of the integration into existing codes comes in modifications to boundary condition subroutines, leaving the core code intact.

Finally, since the present code is extended to include an eddy viscosity turbulence model, as in certain RANS or the SGS LES method from the previous chapter, direct forcing coupled with a reconstruction method provides the infrastructure necessary to treat the near-body turbulence quantities such as eddy viscosity (e.g. [53], [57]). Majumdar et al. [73] noted that for application to RANS or LES, modifications to the turbulence model for continuous forcing would be cumbersome, and using direct forcing with a cut-cell method would require a less efficient unstructured solver.

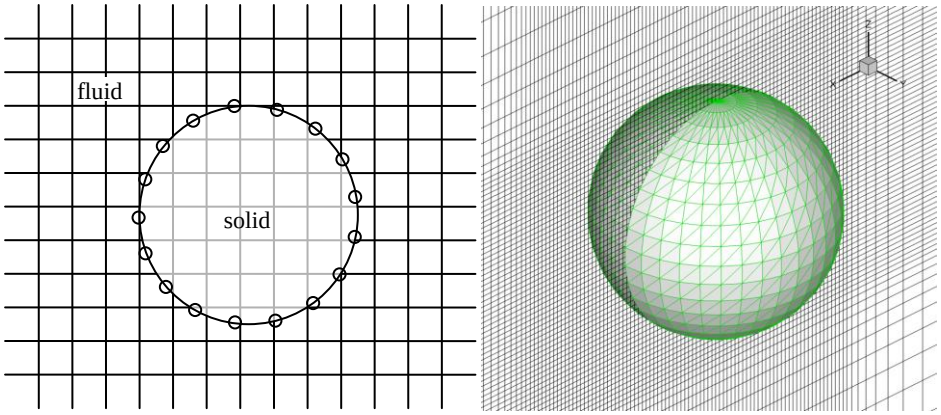

Figure 3.1: Surface representation using (left) marker points in 2D and (right) STL surface tessellation in 3D.

3.1 Boundary Identification

Because the mesh does not exactly follow the shape and orientation of the body's surface, as in body-fitted methods, immersed boundary methods require a separate data structure to track the surface. In 2D, it is a simple task to define a set of "marker points" (Figure 3.1) that are attached to the body to serve as the surface representation. For smooth surfaces, Balaras [57] connected these markers using a quadratic interpolation polynomial (similar to the QUICK scheme described in Chapter 2) which allows a straightforward approximation of midpoint locations and normal vectors. For geometries with sharp corners, such as boxes or airfoils, the present author has found good results using a simple linear connection of the markers.

The extension to 3D boundary representation is not as straightforward, since surface interpolations, rather than 1D polynomial interpolations, are required. A primary concern in 3D is choosing a representation by which a unique normal can be defined at each computational node. The data structure chosen by Iaccarino and Verzicco [53] and

adopted in this work for 2D and 3D representation is the Stereo-Lithography (STL) geometry format (Figure 3.1). With STL geometries, the 3D closed surface is tessellated into triangles without regard to connectivity. Standardized for use with rapid prototyping machines and available in many commercial CAD packages as an export option, the STL file format in its full specification stores the coordinates of the triangle nodes as well as the outward facing normal for each face. Its lack of connectivity information, which differentiates it from other formats commonly associated with finite-element meshes, keeps file sizes small and makes file manipulation more straightforward. Therefore the format provides a low-storage, highly portable and information-rich data structure for use with immersed boundary techniques.

A drawback to STL representation is that CAD STL generation packages typically make no attempt to control the skew and aspect ratio of surface triangles, resulting in highly skewed, high aspect ratio triangles that would be a poor quality surface mesh. Thus, an unmodified STL geometry is often not suitable for interpolating surface forces onto for analysis, and can lead to problems when attempting to identify immersed boundary nodes. To address this in the present code, the STL triangles are preprocessed by further subdividing them using a node-fixed centroid location method that reduces the aspect ratio of the most skewed cells.

With the geometry immersed in the Cartesian mesh, the fundamental connection between mesh and geometry comes by specifying which mesh nodes are positioned inside of the surface. Again, in 2D there are a number of methods of efficiently accomplishing this (e.g. O'Rourke [74]). However in 3D, identifying interior points can be computationally expensive and prone to error. One method that has found widespread

use in computer graphics applications is *ray-tracing*. For each computational node, a ray is extended in an arbitrary direction and the number of surface intersections are counted (Figure 3.2). For a single body, if the number of intersections is odd, the point is determined to be inside of the closed surface. For the STL representation of the surface, there are many exceptions that may negate this rule (Figure 3.2), including rays that intersect nodes of the surface triangles or computational nodes that lie exactly on the surface. To overcome these difficulties, the present implementation extends three rays along coordinate directions and determines the point's position by the majority result.

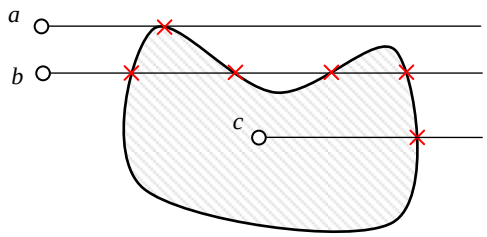

Figure 3.2: Ray-tracing will properly indicate points *b* and *c* as outside and inside of the body, respectively. However, it may fail at point *a* by determining it to be inside.

Each ray intersection with a surface STL triangle is computed by determining whether or not the intersection of the ray and the infinite plane defined by the triangle lies within the boundaries of that triangle. This classic 2D point-in-polygon problem can be solved by using a second 2D ray-tracing algorithm, the winding number method (Chinn and Steenrod [75]), which involves too many trignonometric computations to be efficient for low order polygons, or by computation of the cross product between vectors connecting the 4 points involved. Originally the present code used a vector cross product calculation, and approximately 90% of the boundary node identification time was spent in this cross product calculation. A more efficient technique that takes advantage of the

fact that the polygon is a triangle involves barycentric coordinates. Given the vertices of a triangle, (x_1, y_1, z_1), (x_2, y_2, z_2) and (x_3, y_3, z_3), any point (x, y, z) in the plane defined by the triangle can be represented by a weighted sum of the vertex coordinates:

$$\begin{aligned} x &= \lambda_1 x_1 + \lambda_2 x_2 + \lambda_3 x_3 \\ y &= \lambda_1 y_1 + \lambda_2 y_2 + \lambda_3 y_3 \\ z &= \lambda_1 z_1 + \lambda_2 z_2 + \lambda_3 z_3 \end{aligned} \tag{3.1}$$

where λ_1, λ_2, and λ_3 are constants subject to the constraint:

$$\lambda_1 + \lambda_2 + \lambda_3 = 1 \tag{3.2}$$

After substituting this constraint in to Equation (3.1), one solution of the resulting system of equations for the unknown constants is:

$$\lambda_1 = \frac{(y_2 - y_3)(z_3 - z) - (z_2 - z_3)(y_3 - y)}{(z_2 - z_3)(y_1 - y_3) - (y_2 - y_3)(z_1 - z_3)} \tag{3.3}$$

$$\lambda_2 = \frac{(z_1 - z_3)(y_3 - y) - (y_1 - y_3)(z_3 - z)}{(z_2 - z_3)(y_1 - y_3) - (y_2 - y_3)(z_1 - z_3)} \tag{3.4}$$

$$\lambda_3 = 1 - \lambda_1 - \lambda_2 \tag{3.5}$$

Because the system of Equations (3.1) – (3.2) is over-constrained (four equations in three unknowns), this solution is non-unique. The particular solution in Equations (3.3) – (3.5) is singular if the plane is perpendicular to the z-axis. Analogous cases arise for other solutions with respect to the other coordinate axes. In these cases, the present code selects a non-singular alternate solution. Because Equation (3.1) represents a *linear* combination of the vertex coordinates and the coefficients sum to 1, it can be shown [73] that if the coefficients λ_1, λ_2, and λ_3 are all positive, then Equation (3.1) also represents a *convex*

combination of the vertex coordinates and the point (x, y, z) must lie within the convex hull of the vertices, i.e. within the triangle in question. Determining the intersection of rays and triangular faces by simply testing the signs of λ_1, λ_2, and λ_3 provides a dramatic speed advantage over the other techniques suggested.

3.2 Interpolation Methods

Having flagged all interior nodes using a 3D-ray tracing algorithm and a 2D barycentric point-in-polygon solver, those nodes closest to the boundary are flagged as "boundary nodes" at which the direct forcing will be applied. In some formulations, boundary nodes are defined as interior nodes that have at least one neighbor that is outside of the body. Conversely, boundary nodes can also be defined as exterior nodes that have at least one neighboring interior node. The literature is divided on this choice; for example Balaras [57] and Fadlun et al. [50] preferred the latter approach, whereas Mittal et al. [76] and Kim et al. [77] preferred the first definition. Still, there is a consensus that the choice makes little computational difference [53]; however, it is recognized that only the first definition prevents assignment of boundary conditions within the flow. However, if boundary nodes are taken to be inside of the surface, as in the first method, problems may arise at sharp corners where a unique surface normal may not exist. Nevertheless, the present work adopts the first method of defining boundary nodes primarily because of its apparent reduced interference with the external flowfield.

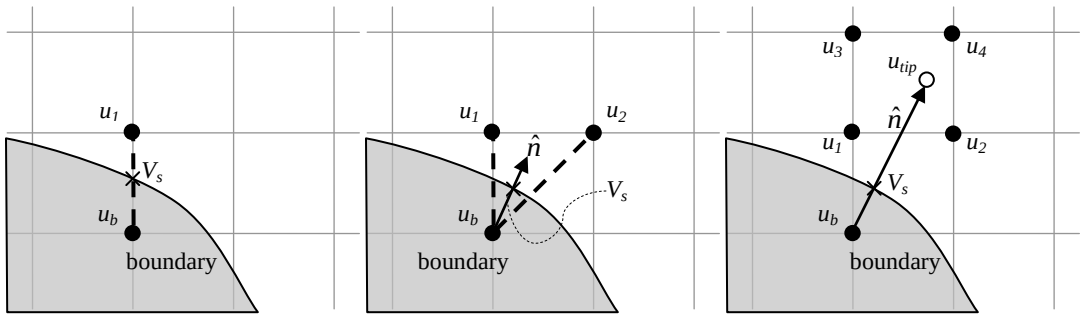

(a) (b) (c)

Figure 3.3: Boundary reconstruction interpolation stencils. (a) linear (b) compact multi-dimensional (c) bilinear used in present work.

The goal then is to directly apply a velocity, pressure, or other scalar (such as eddy viscosity) at each internal boundary node such that an interpolation involving the external surrounding nodes will result in the desired value of the flow parameter at the physical boundary. The use of second-order spatial discretization schemes has led to a number of second-order interpolation stencils for this immersed boundary reconstruction. A 1D reconstruction, similar to that adopted by Fadlun et al. [50], chooses a coordinate direction (preferably the direction with the largest surface normal component) and computes the value at the boundary node by linear extrapolation based on the physical boundary value V_s and the first exterior node u_1 (Figure 3.3a). In the context of a multidimensional simulation, this reconstruction is only formally second-order accurate if the immersed surface is aligned with a coordinate axis. Along highly curved portions of the immersed body this is not possible, which reduces the accuracy near the surface in these areas. Furthermore, as in Figure 3.3a, a unique choice for the interpolation coordinate direction does not always exist; note that the extrapolation could also take place along the horizontal grid line. The result is an increased user input necessary to

ensure that reasonable coordinate directions are chosen. Nevertheless, with adequate resolution near the immersed surface, these problems can be mitigated and good results can be obtained. Table 3.1 presents results from a study of a 2D cylinder wake at *Re* = 40 and *Re* = 100 using 1D-linear reconstruction, a staggered variable arrangement and second-order central spatial discretization on all terms. Reasonable agreement is found with the experimental results of Taneda [78] as well as with the numerical results of Russell and Wang [79] and the high-order computations of Ponta [80].

	Re = 40		Re = 100
	L	θ	*St*
1D Interpolation Study			
162x162	2.25	52.80^o	0.168
354x322	2.32	53.87^o	0.170
514x514	2.33	54.09^o	0.170
Tandea [42]	2.15	-	0.164
Ponta [43]	2.29	-	0.164
Russell and Wang [44]	2.32	53.10^o	0.165

Table 3.1: Separation point, laminar bubble length and Strouhal number computation using 1D linear interpolation for immersed boundaries.

Recent work by Yang and Balaras [81] and Iaccarino and Verzicco [53] has favored the compact multidimensional linear reconstruction in Figure 3.3b. This stencil interpolates the boundary node value using two external nodes (in 2D) and the physical boundary value, resulting in a second-order approximation even for surfaces that are not aligned with coordinate axes. The choice of triangular stencils depends on the orientation of the unique surface normal at each marker or surface point. Yang and Balaras reported that the compact stencil reduces the need for overlapping meshes when block parallelization is used. Additionally, interpolation coefficients are directly related to

values of the strain rate tensor which is helpful when considering fluid/structural coupling problems. If a higher order interpolation is desired, Iaccarino and Verzicco show that the extension to a quadratic interpolation stencil is relatively straightforward.

The method employed in this work is also a multidimensional linear reconstruction, however it uses a tri-linear interpolation taking information from eight external nodes and the physical boundary value. Figure 3.3c illustrates the 2D version of this (bi-linear interpolation and four external nodes), but the 3D extension is straightforward. This scheme is slightly more expensive and difficult to implement because of the increased number of interpolation coefficients, however the resulting stencil is larger, providing more support from external nodes. To determine the boundary node value, a line normal to the surface nearest the boundary node is extended into the flow. This *probe* extends until its tip is surrounded by eight external nodes which then become the *interpolation nodes*. The value of the flow variable at the probe tip can be expressed as a weighted sum of the values of the interpolation nodes. For the 2D case:

$$u_{tip} = c_1 u_1 + c_2 u_2 + c_3 u_3 + c_4 u_4 \tag{3.6}$$

It should be noted that in some circumstances (e.g. in Figure 3.3c) the probe could be allowed to extend only far enough to be surrounded by three external nodes. While this is easily handled mathematically, as interpolation nodes get closer to the body, excessively large boundary node values may be required to satisfy the boundary condition. This can result in stability issues at the boundaries, thus in order to minimize this possibility, the probe is always extended to be surrounded by four nodes. The coefficients $c_1, c_2, c_3,$ and c_4 are given by a standard bilinear interpolation for a Cartesian distribution of points:

$$c_1 = \frac{y_3 - y}{y_3 - y_1}\frac{x_2 - x}{x_2 - x_1} \tag{3.7}$$

$$c_2 = \frac{y_3 - y}{y_3 - y_1}\frac{x - x_1}{x_2 - x_1} \tag{3.8}$$

$$c_3 = \frac{y - y_1}{y_3 - y_1}\frac{x_2 - x}{x_2 - x_1} \tag{3.9}$$

$$c_4 = \frac{y - y_1}{y_3 - y_1}\frac{x - x_1}{x_2 - x_1} \tag{3.10}$$

where x and y are the coordinates of the probe tip and $x_3 = x_1$, $x_2 = x_4$, $y_2 = y_1$ and $y_3 = y_4$. The extension to 3D requires eight coefficients obtained from a standard trilinear interpolation at the probe tip location. Once u_{tip} is determined, the boundary node value is calculated by a linear extrapolation along the surface normal line using u_{tip} and the known physical surface value. For stationary bodies, these coefficients and those required for the final linear extrapolation need only be calculated once as a preprocessing step.

Instead of the linear interpolation represented by Equation (3.6), we could derive a quadratic relation using the four points in 2D. The quadratic interpolation is significantly more expensive and its increased accuracy is negated by the use of linear interpolations to the boundary node value, and the planar representation of the STL facets. However, a convenient benefit of the quadratic formulation is that derivatives at the probe tip in an arbitrary direction $\hat{n} = (n_x, n_y)$ can be calculated directly from the quadratic coefficients in an efficient manner. In 2D:

$$\frac{\partial u_{tip}}{\partial n} = (b_2 + b_4 y)n_x + (b_3 + b_4 x)n_y \tag{3.11}$$

where

$$\begin{Bmatrix} b_1 \\ b_2 \\ b_3 \\ b_4 \end{Bmatrix} = \frac{1}{(y_3 - y_1)(x_2 - x_1)} \begin{Bmatrix} x_2 y_3 u_1 - x_1 y_3 u_2 - y_1 x_2 u_3 + x_1 y_1 u_4 \\ y_3(u_2 - u_1) + y_1(u_3 - u_4) \\ x_2(u_3 - u_1) + x_1(u_2 - u_4) \\ u_1 - u_2 - u_3 - u_4 \end{Bmatrix} \quad (3.12)$$

These efficiently calculated derivatives are used in the imposition of the surface pressure boundary condition, and the calculation of surface forces.

The most significant cost associated with the interpolation procedure is the determination of appropriate normal vectors for all computational nodes that have been identified as IB nodes. Because the surface is represented in STL format, the surface normals for each triangular face are computed and stored during the creation of the geometry. The task is to determine which pre-computed surface normal to use for each boundary node. We require that the normal line for a given triangle, drawn through the boundary node, intersects the plane defined by the triangle within the boundaries of that surface triangle. Then, the desired normal is taken as the normal of the nearest surface triangle that meets these requirements. Thus two searches are needed: one to determine which triangles meet this criteria and a second to determine the closest of those triangle to the boundary node. The first search reduces to the point-in-polygon problem over a search of all surface triangles for each boundary node. This process is performed using the barycentric coordinates technique described in the previous section. The second search is typically not expensive, involving only the sorting of a small list of floating point numbers.

3.3 Imposing Immersed Boundary Conditions

Immersed boundary conditions are applied each time that conventional boundaries are updated. To enforce the linear interpolation from the probe tip to the boundary node we

$$u_b = \frac{V_s - u_{tip}\Delta_{node}}{\Delta_{tip}} \tag{3.13}$$

apply Equation (3.13) at each boundary node, where V_s is the surface velocity, Δ_{node} is the normal distance from the boundary node to the surface, and Δ_{tip} is the normal distance from the probe tip to the surface. The pressure boundary condition approximation for stationary bodies, $dp/dn = 0$, is enforced at the surface by applying $u_{bound} = u_{tip}$ at each boundary node. Care must be taken however since this modifies the Poisson equation at the boundary nodes. To reflect this in the discrete equations, the 5-diagonal (7-diagonal in 3D) spatial discretization matrix, *A*, and source term, *b*, in the discretized governing flow equations must be modified accordingly. Since this matrix equation represents a linear system of equations, each row of the *A* matrix specifies the dependence of every node (*i,j*) with its four neighbors in 2D (*i,j-1*), (*i-1,j*), (*i+1,j*) and (*i,j+1*). At boundary nodes, since Equation (3.13) already includes the influence of neighboring points on the pressure at u_{bound}, the coefficients of the four neighbors are set to zero and the coefficient of the boundary node is set to 1. In matrix form this appears as:

$$\begin{bmatrix} & & & & & & & & & & \\ \ddots & \ddots & \ddots & & \ddots & & & & & & \\ S_{l-1} & & W_{l-1} & C_{l-1} & E_{l-1} & & N_{l-1} & & & & \\ 0 & & 0 & 1 & 0 & & 0 & & & & \\ & S_{l+1} & & W_{l+1} & C_{l+1} & E_{l+1} & & N_{l+1} & & & \\ & \ddots & & \ddots & \ddots & \ddots & & & \ddots & & \end{bmatrix} \begin{Bmatrix} \\ \\ \\ \vdots \\ u_{bound} \\ \vdots \\ \\ \\ \\ \end{Bmatrix} = \begin{Bmatrix} \\ \\ \\ \vdots \\ u_{tip} \\ \vdots \\ \\ \\ \\ \end{Bmatrix} \tag{3.14}$$

The technique for achieving this in an algorithm is commonly referred to as "blanking" or "iblanking." In an array, often called *iblank*, each mesh node is flagged with a *0* if it is a boundary node, and is flagged with a *1* otherwise. In this way, when the vectors *S,W,E,N* (coefficients of Equation (2.10)) are formed, multiplying them by the node's *iblank* value will create the necessary modification of the *A* matrix. Note that we cannot simply multiply the vector C by *iblank* because this would result in a row of all zeros and a singular matrix. The vector C may be modified by: $C = (1 - iblank) + (iblank)C$. Note also that at boundary nodes, the right-hand-side of Equation (2.10) must be set to u_{tip} to complete the discrete pressure equations. With the present semi-implicit schemes, similar matrices must be inverted for the momentum equations (Equation (2.9)) and iblanking in a similar form is used to ensure that the matrix equations represent the correct boundary conditions.

3.4 Handling Interior Nodes

If the interior nodes that are not boundary nodes are left untreated, a flow will develop inside the body that may be affected by the external flow through a dependence on the boundary nodes. In a fully elliptic system, each node value depends on the value at every other node. The blanking and immersed boundary imposition processes seek to limit this by separating the computational domain into exterior and interior regions whose nodes only depend on other nodes in that region. Mathematically this is possible, however in practice, the interpolation and blanking near irregular or sharp geometries may permit some level of contamination of the external flow by the internal flow. Nevertheless, in the literature, studies that discuss internal nodes have found that the

internal treatment of the body has little effect on the external flowfield ([50], [53]). In the present work, to ensure that no erroneous information is passed from the interior to the exterior of the immersed body, the internal values of velocity, pressure, *iblank* and all relevant source terms are set to zero. For *fixed* bodies this is a reasonable solution that should not adversely affect convergence or accuracy. For non-stationary bodies however, the imposition of zero quantities slows the convergence of the iterative pressure solver.

3.5 Force and Power Calculation

Calculation of the viscous and pressure forces is performed using the standard incompressible stress relation:

$$\sigma_{ij} = -P\delta_{ij} + \mu\left(\frac{\partial u_i}{\partial x_j} + \frac{\partial u_j}{\partial x_i}\right) \tag{3.15}$$

However, for immersed boundary methods this is complicated by having to evaluate the stress tensor at the body's surface, which does not necessarily coincide with the computational nodes. Therefore, the interpolations of pressure and velocity gradients are needed again, similar to the imposition of the immersed boundary conditions themselves.

As mentioned in Chapter 2, the pseudo-pressure ϕ used to enforce the divergence-free condition in the fractional-step methods is actually not the physical pressure needed to compute the normal force on the element. They are related by the Laplacian: $P = \frac{1}{2}\nu\Delta t\nabla^2\phi$. With physical pressure calculated, P is interpolated to the centroid of each triangle of the STL body using the same tri-linear interpolation method in Section 3.2. It is critical to note that since we are assuming that the pressure and (shear) are constant across each STL facet, if the STL mesh has high aspect ratio triangles, or triangles that

are too large to represent the gradients of forces across the surface, then the accuracy of the computed forces suffers. This is a key reason why the surface mesh refinement in the preprocessing of the STL immersed body as discussed in Section 3.1 is important.

Calculating the velocity gradient tensor at the centroid of each facet can be accomplished by computing the velocity gradients using the quadratic interpolation coefficients discussed in Section 3.2. This results in a computationally efficient calculation with a compact stencil. Finally, stresses at each facet are multiplied by the facet area to give local force vectors at each surface element. The resultant body force is then just the summation of these local forces over the body, and similarly, power is computed by summing the dot product of the local force and local body velocity, $\sum(\vec{F} \cdot \vec{V})$, for all surface mesh elements.

3.6 Verification and Validation

Validation of the immersed boundary implementation combined with the baseline solver in Chapter 2 is performed for two representative cases: Low Re flow over a sphere ($Re = 20 - 300$) and moderate Reynolds number over a flat plate ($Re = 8026$). Additional verification and validation cases may be found in [82] .

3.6.1 3D Sphere

In three-dimensions, a canonical analogue to the two-dimensional cylinder problem is found in computing the flow over a sphere. This problem encompasses multiple flow regimes for the low Reynolds numbers under consideration, however the present validation focuses on verifying the immersed boundary solver in the steady axisymetric

wake regime at $Re < 250$, and qualitatively comparing the flowfield with expected results in the unsteady asymmetric flow regime at $Re = 300$. Steady axisymmetric flow is computed in a domain of $26D_0 \times 16D_0 \times 16D_0$ with 215×130×130 points in the streamwise and two cross-stream directions, respectively. This 3.6×10^6 point mesh is generated such that a uniform spacing of $0.02D_0$ is present at the sphere surface. The computed forces and surface pressure distributions did not significantly differ with a uniform surface spacing twice as small, however the finer mesh was required to accurately capture the flow separation point. With this steady computational mesh, approximately 9.3×10^3 boundary nodes are generated. The mesh used for the unsteady asymmetric flow at $Re = 300$ covers a $44D_0 \times 18D_0 \times 18D_0$ domain with 260×150×150 points in the streamiwse and two-cross stream directions, respectively. The surface mesh for the sphere for all cases is tessellated into 1,368 triangles.

The steady flow regime for the sphere is characterized by a laminar separation vortex in the wake of length L_0 whose center is fixed at some position x_c, y_c in a plane passing through the center of the sphere. Figure 3.4 plots the nondimensional vortex length and nondimensional vortex position as compared with the experimental findings of Taneda [78] and the body-fitted computations of Johnson and Patel [83]. Although the trend is captured well, there is a slight underprediction of the experimentally measured vortex length for each Reynolds number. It should be noted however that the present results are in good agreement with the published body-fitted computational results, indicating that the immersed boundaries are most likely not the cause of this consistent underprediction across methodologies. The computed vortex locations shown in Figure 3.4b are in excellent agreement with the experimental and body-fitted results.

At $Re = 300$ the dominant vortical structures in the unsteady flow include a standing horseshoe vortex that envelops the sphere, and hairpin vortices formed in the wake whose tails and head are oriented along a single streamwise plane (in this case the x-z plane). Flow remains symmetric about the x-y plane (Figure 3.5). Isosurfaces of the second invariant of the velocity gradient tensor, Q-criterion, are plotted in Figure 3.5 and are compared with the computed wake structures of Johnson and Patel [83].

The general topology of the two computations is similar. Shown at the beginning of the shedding cycle, hairpin vortex legs are seen emanating from the sides of the sphere in the x-z plane. These roll-up to form the first vortex head at approximately 4.5 diameters downstream for the present computations. However, the present vortices appear stretched in the streamwise direction as compared with the Johnson and Patel results, which appear to stretch radially away from the wake centerline. These phenomena are most likely attributed to differences in the non-uniform computational meshes. In the wake region, the Cartesian mesh used for the present results is stretched in the streamwise direction but unavoidably remains uniform in cross-stream directions. This results in high aspect ratio cells which may account for an artificial streamwise diffusion of vorticity. Similarly, the spherical body-fitted mesh of Johnson and Patel stretches radially away from the sphere which may account for some artificial diffusion in that direction.

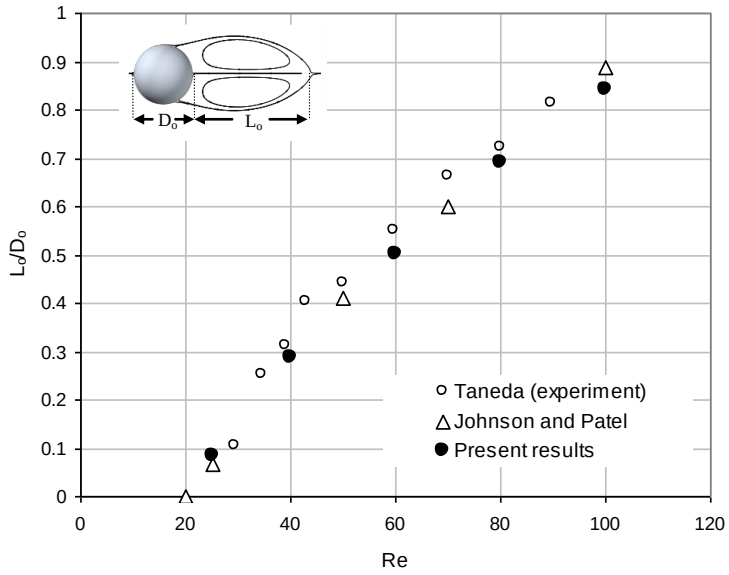

(a)

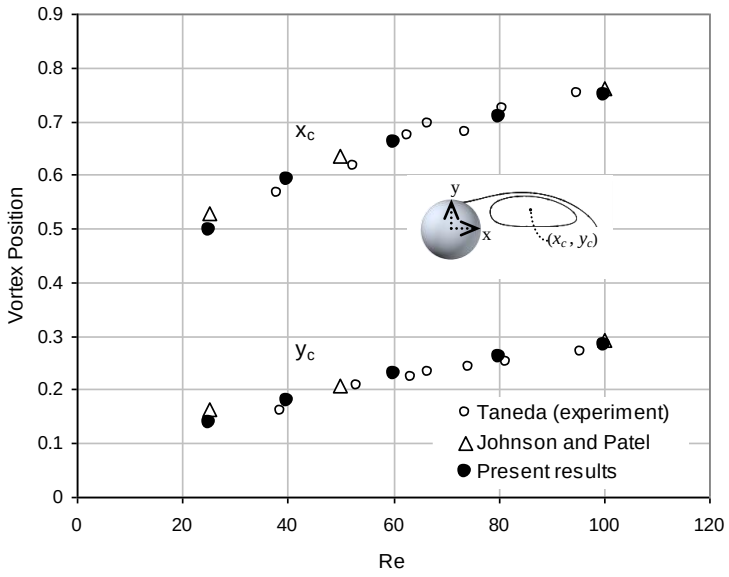

(b)

Figure 3.4: Computed 3D cylinder flowfield parameters at various Re; (a) steady seperation vortex length, (b) steady separation vortex position.

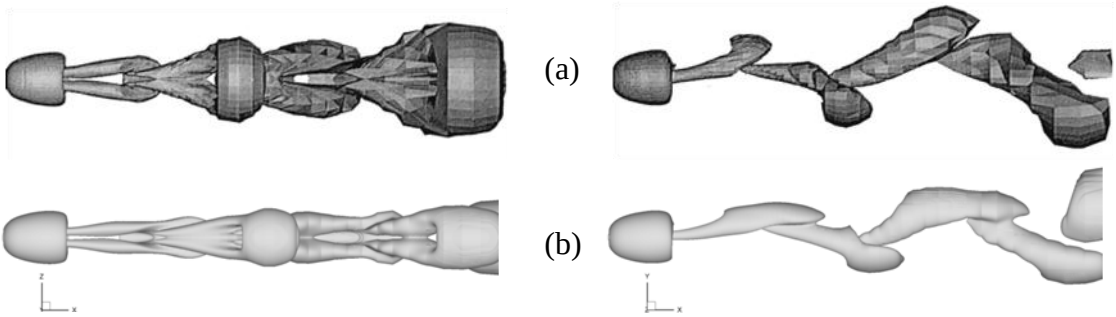

Figure 3.5: Unsteady vortical structures in the *x*-*z* and *x*-*y* planes of a sphere at $Re = 300$ as computed by (a) Johnson and Patel [83] and (b) present immersed boundary.

3.6.2 3D Flatplate

The PIV data of Kaplan et al. [84] are used in validating the flow solver at higher Reynolds numbers. In the experiment, tip vortex measurements were made using a rectangular flat plate of aspect ratio 2, a thickness-to-chord ratio of 0.015, an angle of attack $\alpha = 10°$, and at a moderate Reynolds number of 8028. The 1.1×10^7 point, 16-block computational mesh is shown in Figure 3.6. The mesh is refined for accurate vortex capture through 3 chords downstream of the trailing edge.

Figure 3.7 shows the swirl velocity profile through the center of the tip vortex at three downstream locations, where $x/c = 0$ indicates the trailing edge of the plate. At the $x/c = 0.1$ station, the velocity peak magnitudes are captured well. In both experiment and computations the depression in swirl velocity at the outboard peak is most likely the result of continued influence from the nearfield attached vortex sheet. This depression is much stronger in the computations, however by $x/c = 1.0$, this depression is not present and the computed velocity profiles are qualitatively similar to the experiment. The computed vortex decays more rapidly than the experiments resulting in a 6% lower swirl velocity magnitude at the $x/c = 2.0$ station. Considering the second-order viscous

discretization and the upwinded convective terms, this may be a result of numerical diffusion; a problem which might be mitigated with appropriate grid refinement. Nevertheless, the vortex core radius is consistently in agreement with experiment at each station. In spite of the apparent peak-locking in the PIV data, the comparisons of streamwise vorticity in Figure 3.7 further illustrate the agreement of the computations with experiment. Both the vortex size and position at each downstream station are qualitatively quite similar.

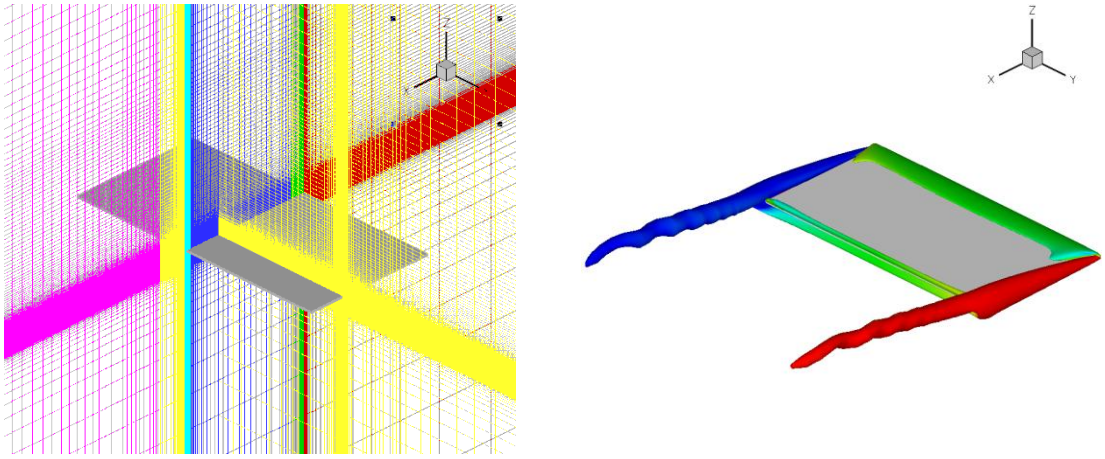

(a) (b)

Figure 3.6: (a) 1.1×10^7 point computational mesh for $Re = 8026$, $\alpha = 10^o$, (b) Sample flow solution visualized by isosurfaces of the second invariant of the velocity gradient tensor. Contours highlight streamwise vorticity.

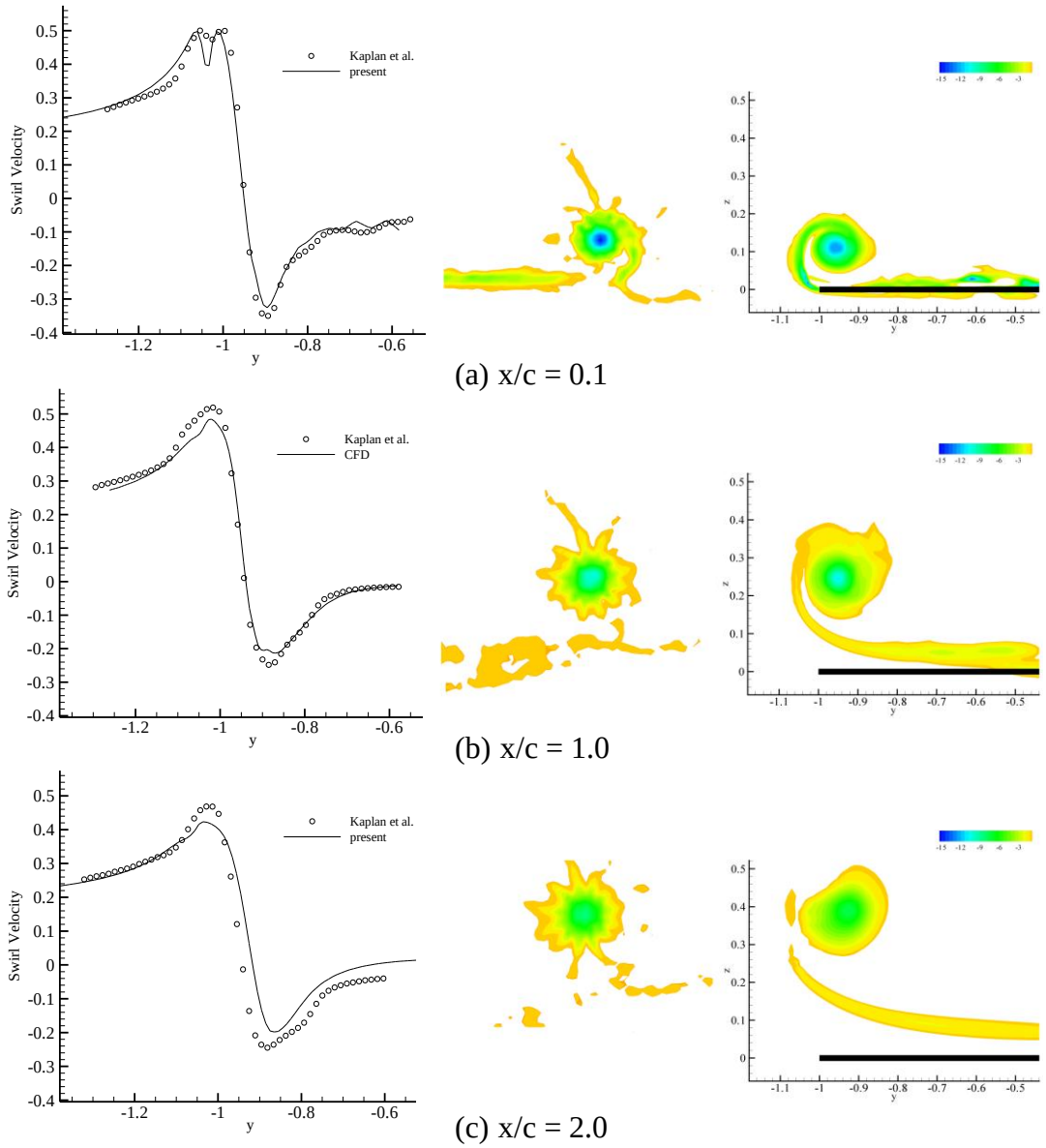

Figure 3.7: Nondimensional tip vortex swirl velocity comparison with Kaplan et al. [84], (left). Contours of experimental nondimensional streamwise vorticity in the tip vortex (center). Computational streamwise vorticity (right).

3.7 Summary: The IBINS Solver

The immersed boundary implementation described above is applied to the baseline incompressible Navier-Stokes solver described in the previous chapter to form the Immersed Boundary Incompressible Navier-stokes Solver (IBINS). The following is a summary of the features of the developed code:

- Cartesian Incompressible variable viscosity pressure-velocity formulation of the Navier-Stokes equations
- Kim and Moin fractional-step pressure-velocity coupling
- Time discretization options:
    - 2^{nd} order Adams Bashforth (all terms)
    - 3^{rd} order Runge-Kutta (all terms)
    - Option to treat viscous terms implicitly with 2^{nd} order Crank-Nicolson
- Spatial discretization options:
    - 2^{nd} order central (all terms)
    - 3^{rd} order modified non-uniform QUICK (convective terms)
    - 2^{nd} order limited upwinding with VanLeer's monotanized central limiter or Roe's Superbee limiter (convective terms)
- Pressure Poisson solution computed with an approximate incomplete LU decomposition, the strongly implicit procedure (SIP)
- External flow boundaries handled with the Orlanski outflow condition
- Option for Dynamic Smagorinsky Subgrid Scale LES model for high Reynolds number flows
- Discrete Immersed boundaries

    - Efficient barycentric interior node identification methodology
    - 2^{nd} order tri-linear interpolation coefficients for boundary variable enforcement.
- Block parallelization with explicit block boundary communication using the MPICH standard

Chapter 4 –

Quasisteady Rotation Simulations

The following two chapters describe the application of the immersed boundary solver to two types of flapping-wing low-Reynolds number model problems. The goal is to use these simplified cases to draw conclusions about the fundamental parameters affecting the force production during full flapping flight. The first model problem consists of an impulsively started wing rotating at a fixed pitch angle and rotational velocity. This problem does not take into account unsteady or returning-wake ("wake-capture") effects and thus allows the forces on the wings to develop based only on kinematics and geometry. To build these unsteady effects into the simulations, the second set of model problems involves adding time varying pitch and rotational velocities in such a way as to simulate the idealized kinematics of flapping insects such as *Drosophila*.

There are a number of simplifications made to the kinematics, geometry and flow conditions for all results in this work. Wings are modeled as rigid bodies with relatively large thickness-to-chord ratios. While most insects and current MAVs use thin wings flexible enough to undergo significant deformation during their typical strokes [11], the finite thickness of the present simulated wings is a computational requirement imposed by the immersed boundary formulation to keep simulation costs practical. The effects of this artificially larger thickness-to-chord primarily manifest in the unsteady flapping cases during stroke reversal, as will be discussed. Nevertheless, the rigid wings give insight into the more fundamental parameters affecting force generation for these

simplified motions, such as wing-wake interaction, and leading-edge vortex (LEV) generation and retention.

4.1 Geometry and Flow Parameters

The wing geometry is similar for all of the following cases:

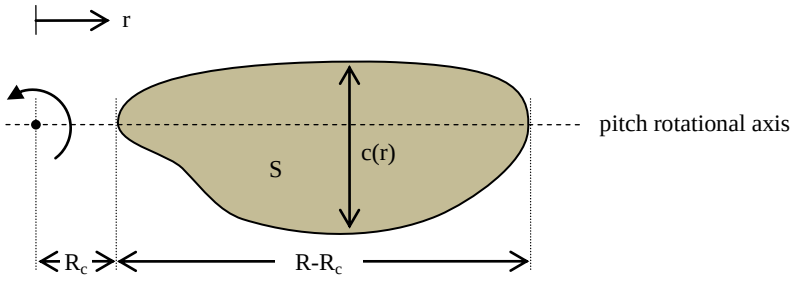

Figure 4.1: Schematic of modeled wing geometry. Wing surface area (S), chord as a function of radial position (c), root offset (R_c), wing length (R).

A significant portion of flapping-wing literature has adopted a definition of Reynolds number based on the mean wingtip velocity over a single stroke, $\overline{V}_{tip}$, and mean *geometric* chord, $\bar{c} = S/R$:

$$Re = \frac{\bar{c}\bar{V}_{tip}}{\nu} \tag{4.1}$$

Writing in terms of kinematic stroke parameters, Reynolds number can be expressed:

$$Re = \frac{\bar{c}\bar{V}_{tip}}{\nu} = \frac{R\,(\bar{\omega}R)}{\nu\,A_r} = \frac{SR(2\Phi f R)}{R^2\nu} = \frac{2S\Phi f}{\nu} \tag{4.2}$$

where A_r is the aspect ratio for a single wing. When cast in these forms, it is seen that Re is only geometrically based on the surface area of the wing and its aspect ratio. However,

clearly the force production of the flapping wing is dependent on the specific planform of the wing as well. Furthermore, because the characteristic velocity that the Reynolds number is based on is a rotational velocity, it makes sense that we would want to include the effects of each spanwise section of the wing operating at a different rotational velocity, and thus a different effective Re. In order to do this, we can construct a velocity-weighted mean chord as follows.

The geometric area, S, of the wing in Figure 4.1 is given by the integral:

$$S = \int_0^R c(r)dr$$

The standard definition for weighting of forces uses the dynamic pressure $0.5\rho V_\infty^2$, where the freestream velocity is $V_\infty = \Omega R$. A velocity-weighted surface area then can be written:

$$S_w = \int_0^R \frac{0.5\rho(\Omega \mathrm{r})^2}{0.5\rho(\Omega \mathrm{R})^2} c(r)dr = \int_0^R \left(\frac{r}{R}\right)^2 c(r)dr = R\int_0^1 \hat{r}^2 c(\hat{r})d\hat{r} \qquad (4.3)$$

where $\hat{r} = r/R$. An equivalent mean-chord would then be the chord which would arise from assuming that this weighted chord was uniform in $\hat{r}$ [84]:

$$R\int_0^1 \hat{r}^2 c(\hat{r})d\hat{r} = R\bar{c}_w \int_0^1 \hat{r}^2 d\hat{r}$$

Therefore, solving for the weighted mean chord:

$$\bar{c}_w = 3\int_0^1 \hat{r}^2 c(\hat{r})d\hat{r} \qquad (4.4)$$

Equation (4.4) accounts for the variation in planform shape, and weights the portions of the chord more heavily towards the tip where local incident velocities are highest. This relation is similar to that derived in [84] for the thrust weighted equivalent chord for a rotorcraft.

This weighted mean chord gives a proper basis for comparison across multiple flapping-wing planform shapes. However, as stated, most relevant literature, including all experiments and computations referenced in this work, parameterize their studies using the geometric mean chord. Therefore, in order to facilitate direct comparison, this work will also use the geometric definition of mean chord and the Reynolds number as given in Equation (4.2). Consequently, care must be taken when comparing results and when scaling between computational and experimental space, to maintain the wing planform shape. Therefore for the results presented in this work, in addition to the traditional characteristic dimensions of geometric mean chord and aspect ratio, geometric scaling is also based on the second moment of area about the rotational axis of the wing.

4.2 Incompressibility and Reduced Frequency

A major assumption in this work is that of incompressibility. While intuitively the low velocities associated with insect flight as compared with the speed of sound would indicate that incompressibility should be a reasonable approximation, the high flapping frequencies of *Drosophila* and similar insects means that problems can be highly unsteady. This section will demonstrate that the kinematics that create this unsteadiness for the class of problems under consideration, do not generate significant compressibility effects which would require a more complex compressible analysis. Furthermore, in order to justify both the comparison of computational results to experimental results, and the scaled experimental results to the physical insect flapping, we need to consider the incompressibility relating to both experiment and actual insect scale flapping.

The experimental flapping studies used as a basis of comparison for the simulations in this work were conducted by moving the scaled model wing through mineral oil with Reynolds number matched to typical *Drosophila* values. Properties of the experimental setup will be discussed in greater detail in the following sections, but a summary of the relevant parameters for determining incompressibility and reduced frequency is as follows:

Mineral oil (at standard conditions):

- Density, ρ = 880 kg/m^3
- Bulk Modulus, K = 1.83 GPa
- Sound propagation speed, $a = \sqrt{(\rho/K)}$ = 1440m/s

For the impulsively started rotational cases in this chapter, the wing is rotated at a constant rotational velocity $\omega_r = 1.192\, rad/s$. The wingtip is at $R = 0.26\, m$. Velocity at the 75% span location is then $(0.75)\omega_r R = 0.23\, m/s$. Mach at 75% span is $M = 0.23/1440 = 1.6 \times 10^{-4}$. Since this rotation is steady and there are no other sources of forced oscillations, this Mach number, which is much less than 0.3, indicates that the incompressible assumption should work well.

For the flapping cases, the wing undergoes time-varying rotational and pitch rates. Each must be considered separately to ensure that their resulting velocities don't violate the incompressible assumption. For the unsteady cases in the next chapter the peak rotational rate is $\omega_r = 1.182\, rad/s$, which is a constant value that occurs during 64% of the full up/down stroke. The wingtip is at $R = 0.25\, m$. Velocity at the 75% span location is then $(0.75)\omega_r R = 0.30\, m/s$. Mach at 75% span is $M = 0.30/1440 = 2.1 \times 10^{-4}$. This again is well within reasonable incompressible assumption limits.

The pitch oscillations for the unsteady flapping cases introduce a second source of unsteadiness. The maximum pitching rate, which occurs just before stroke reversal, for the experimental and computational cases considered is $\omega_p = 1.55\,\mathrm{rad/s}$. Using the mean chord $\bar{c} = 0.0668\,m$ as the rotational arm (a conservatively large value since the wing pitches about the 45% mean chord line), the peak pitching velocity is $\omega_p \bar{c} = 0.104\,m/s$. Mach number for this condition is $M = 0.104/1440 = 7.2 \times 10^{-5}$.

The dimensionless reduced frequency parameter compares a forced frequency of a body's oscillation to a freestream velocity in order to characterize the unsteadiness of a problem. This is analogous to the Strouhal number in which (often) a vortex generation frequency associated with an unsteady fluid flow is compared with the flow's bulk velocity. For the unsteady cases, the kinematics simulate the hover condition, therefore the bulk velocity is zero and so the reduced frequency is zero by definition (or undefined). However, if we take the bulk velocity to be the rotational velocity, and the oscillating component to be the pitch oscillations, we can define a reduced frequency as:

$$k(\tau) = \frac{\omega_p(\tau)\bar{c}}{(0.75)2\omega_r(\tau)R} \tag{4.5}$$

Where $\omega_p(\tau)$ is the pitching rate at time τ, $\omega_r(\tau)$ is the rotational rate at time τ, $\bar{c}$ is the mean chord, and this reduced frequency is calculated at the 75% span location. Reduced frequency for the baseline case of Chapter 5 is plotted in Figure 4.2 for a full up/down stroke. Stroke reversal occurs at integer multiples of $\tau = 0.25$.

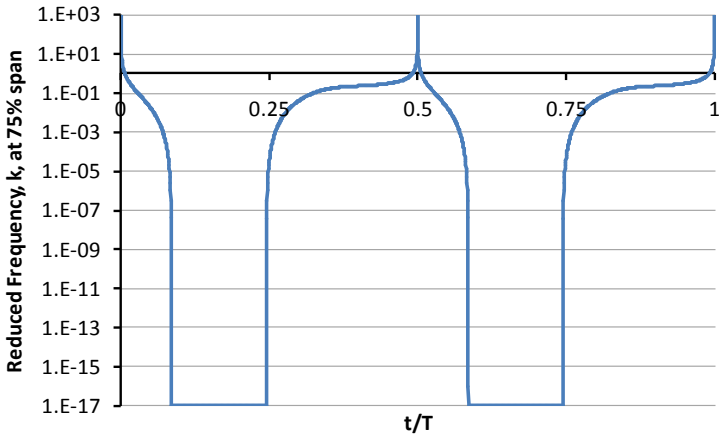

Figure 4.2: Reduced frequency time history at 75% span for representative flapping case.

Reduced frequencies above 0.05 are usually considered unsteady [85], therefore as Figure 4.2 shows, significant portions of the stroke surrounding the stroke reversal will likely not follow steady or quasisteady models without those models specifically accounting for this unsteadiness [11], [14]. The unsteadiness of the problem is accounted for implicitly in the solution of the incompressible Navier-Stokes equations, so no specific modifications need be made based on the unsteadiness of the problem. However, is it still important to compute the reduced frequency because the quantity $M(\tau)k(\tau)$ should also remain small relative to unity in order to justify incompressibility for unsteady cases [84]. Figure 4.3 shows that this constraint is not violated, as the product of Mach number and reduced frequency remains well below 1 throughout the entire stroke.

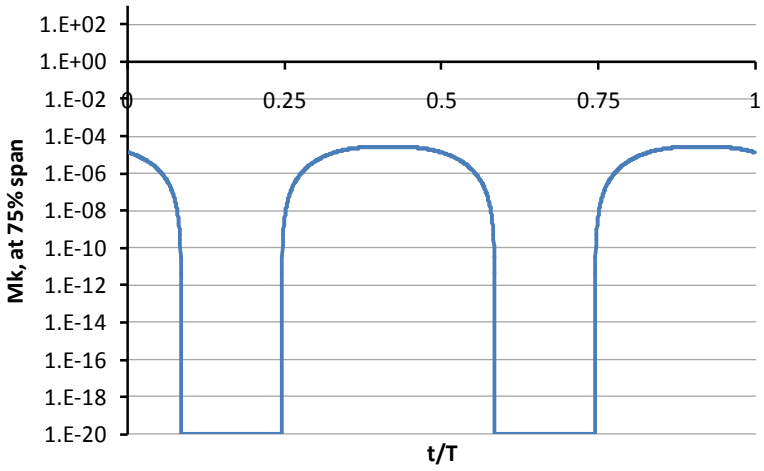

Figure 4.3: Product of Mach number and reduced frequency at 75% span time history for representative flapping case

Computations and experiments both simulated dynamically scaled kinematics, based on Reynolds number, not Mach number. Therefore, we should also ensure that the incompressibility of the problem is not dissimilar between the physical *Drosophila* and the experiments/computations. Speed of sound in air at sea level standard conditions is approximately $340 m/s$. Mean *Drosophila* wingtip velocity is approximately $2.8 m/s$ [86]. Thus, the rotational velocity at 75% span is $2.1 m/s$, and the Mach number is $M = 2.1/340 = 0.0061$.

Assuming similarly scaled pitching/rotational rates between experiment and the actual *Drosophila*, the maximum pitch velocity is $\omega_{p,max} = (2.1/0.30)\, 0.104\, m/s = 0.73\, m/s$. Therefore, $M_{max} = 0.73/340 = 0.0021$, which is again well within the incompressible assumption limits.

4.3 Impulsively Started Rotation

Although a highly simplified motion compared to the actual kinematics of hovering insects and flapping MAVs, an impulsively started constant pitch-angle rotating wing is a rough approximation to the initial downstroke seen in the more complex motions [87]. This motion is also well suited to visualizing and characterizing the formation and structure of the LEV without interference from the shed vorticity from previous strokes. An understanding of this simplified case can greatly improve the understanding of the more complicated interactions that occur as a result of a full flapping motion, and Chapter 5 will explore the connection between this chapter's quasisteady motion and more complicated kinematics.

4.3.1 Computational Setup

The simulation parameters correspond to the experimental conditions of Birch et al. [88] who used the Robofly apparatus to rotate a single wing at a constant angular velocity and pitch at two Reynolds numbers, $Re = 120$, and $Re = 1400$, based on chord and wingtip velocity. The wing is assumed to be rigid and the planform geometry is taken from a computational study of Drosophila flight mechanics by Emblemsvag and Candler [44]. The computational wing fills in this inboard geometry with the approximate shape of a typical *Drosophila* wing. The computational wing area is $0.0173m^2$ with a span of $0.26m$. The planform of the experimental setup was truncated from $0.1m$ to the rotational center to allow for the presence of a mounting arm and load cells. Their study employed a wing thickness of 3.7 times that of the experiment that they were simulating. The authors were able to show that modifying the modeled wing thickness was able to

affect the computed forces in an unsteady flapping case by as much as 15% at stroke reversal. Therefore, in an effort to minimize this effect and generally more faithfully represent the experimental conditions, the thickness of the present computational wing is taken to be $4.5mm$, 1.8 times the experimental value. As mentioned, while a wing model with the same thickness as the experiment would be ideal, the increased thickness is taken in an effort to minimize the number of computational nodes necessary to resolve both the flow features and the geometry. The Cartesian mesh used in each low Re case contained 17.8×10^6 nodes with a uniform resolution over the wing path of $1.5mm$. Computations at $Re = 1400$ were carried out using an approximately 30×10^6 node mesh with a minimum resolution of $1.0mm$ in directions parallel to the stroke plane, and $1.3mm$ in the third normal direction.

At each pitch angle the wing is rotated a total of $\Phi = 180°$ at a constant angular velocity of $1.192\ rad/s$. From rest, the angular velocity is exponentially increased to this constant value according to the function $\phi(t) = (1 - e^{t/t_c})/R$, where the characteristic time is taken to be $t_c = 0.2s$. This time constant is reported by Poelma et al [87] to reasonably approximate the acceleration of the Robofly experimental mechanism. Computational transients from the initial conditions and physical transients from the imposed acceleration are negligible after approximately $70°$ of rotation. After this point, mean forces are averaged over an additional $80°$ of rotation (see Figure 4.4).

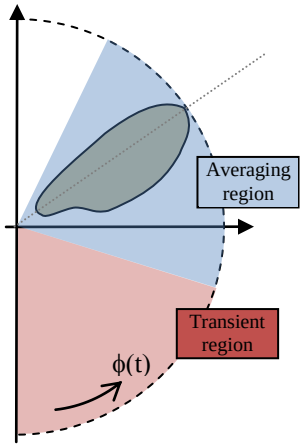

Figure 4.4: Stroke schematic and averaging region for the quasisteady cases

4.3.2 Force and Flow Visualization

The computed forces for $Re = 120$ and $Re = 1400$ for the given range of pitch angles are plotted in Figure 4.6. These forces are represented by a force component normal to the wing's surface computed directly from the pressure forces, and a tangential force component computed directly from shear forces. This standard decomposition of the resultant force will prove useful in isolating viscous and inviscid mechanisms of force production, especially for the flapping cases of the next chapter. Here, for example, note that above a pitch angle of approximately 5°, the pressure forces for both high and low Reynolds numbers dominate the shear tangential forces—i.e the viscous contribution to force production is negligible over most to the pitch angle range, even for these "low" values of Re.

The more common representation of the resultant forces in flapping-wing literature is to resolve the normal and tangential forces into a force normal to the stroke-plane, and a force parallel to the stroke plane that acts opposite the flapping direction (Figure 4.5). The normal component is often termed "Lift", although the true definition of lift is the

resolution of the force perpendicular to the relative wind, not the stroke plane. The tangential in-plane force is termed "Drag", although again, the true aerodynamic definition of drag is the force resolved parallel to the relative wind. To facilitate comparison with literature, throughout the rest of this work, the terms "Lift" and "Drag" will refer to forces normal and tangent to the stroke plane, respectively. Furthermore, it should be noted that the "Pressure" force and "Shear" forces refer to the forces normal and tangential to the wing, respectively (see Figure 4.5).

Figure 4.7 resolves the pressure and shear forces into lift and drag, and plots the computed values against experimental [88] lift-to-drag ratio (L/D) for pitch angles ranging between $0° - 90°$ (note: independent measurements of lift and drag were not available for the experimental data). Taking into account differences in wing geometry, the L/D characteristics of the computations are reasonably consistent with the experiment. At both values of Reynolds number, the computational wing appears to reach its peak L/D at a slightly higher angle of attack than in the experiment, however both sets of results show the characteristic collapse of L/D values at higher pitch angles, as pressure drag dominates force production. A note on the grid-independence of these results: Refining the mesh by 66% along the stroke path for both Reynolds numbers improved (reduced) the predicted L/D values for $\alpha \leq 20°$ by 5% – 7%, indicating some small but acceptable level of grid dependence. It is to be noted that for pitch angles greater than $20°$, the finer meshes yielded L/D results within 1% of those found on the coarse meshes.

Flow separates at a small angle of attack ($\alpha < 5°$) for these flat-plate wings, therefore all of the data points collected are in the post-stall regime. The lift curve rises

and falls symmetrically about the 45° pitch angle in a parabolic arc qualitatively similar to post-stall lift recovery regions observed for high Re airfoils (both cambered and non-cambered) under certain conditions (see, for example, Ostowari and Naik, 1985 [89]). Drag for these low Re cases also shows the characteristic 'S' curve that is symmetric about the 45° pitch angle for the post-stall regime.

The peaks in computed lift occur at just below $\alpha = 50°$ for both Reynolds numbers, making this a point of interest for the flow visualizations to follow. L/D at α = 50^o however is approximately equal for $Re = 120$ and $Re = 1400$, therefore we will also look at the α =30^o case where the difference in L/D is more significant but lift is still relatively high. Each visualization is made at $\phi = 144.5°$, well after the force time histories indicate that the nearfield flow has reached a quasisteady state. In addition to the force time-histories, flow visualizations of vorticity and Q-criterion were studied to confirm that the nearfield flow features were not significantly different at translational positions 45^o earlier or later.

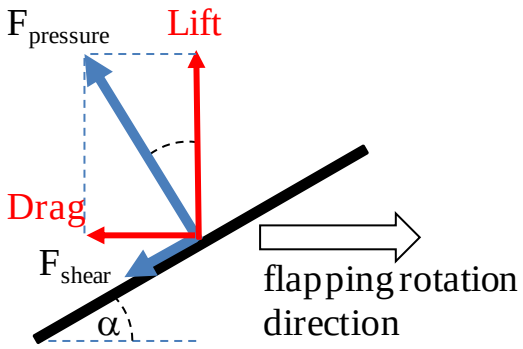

Figure 4.5: Force terminology used throughout this work.

For Figures 4.8 – 4.13, all streamlines are computed using the body-fixed reference frame velocity field. This prevents the apparent fluid motion resulting from the motion of the wing from obscuring the nearfield vortical structures. In regions where the flow can be considered to be steady, this also means that body-fixed streamlines are equivalent to streaklines. In contrast, all spanwise flow contours in the following plots are computed in the inertial frame to avoid contamination from off-axis components of spanwise flow that would appear in the body-fixed frame. Velocities are all normalized by tip velocity.

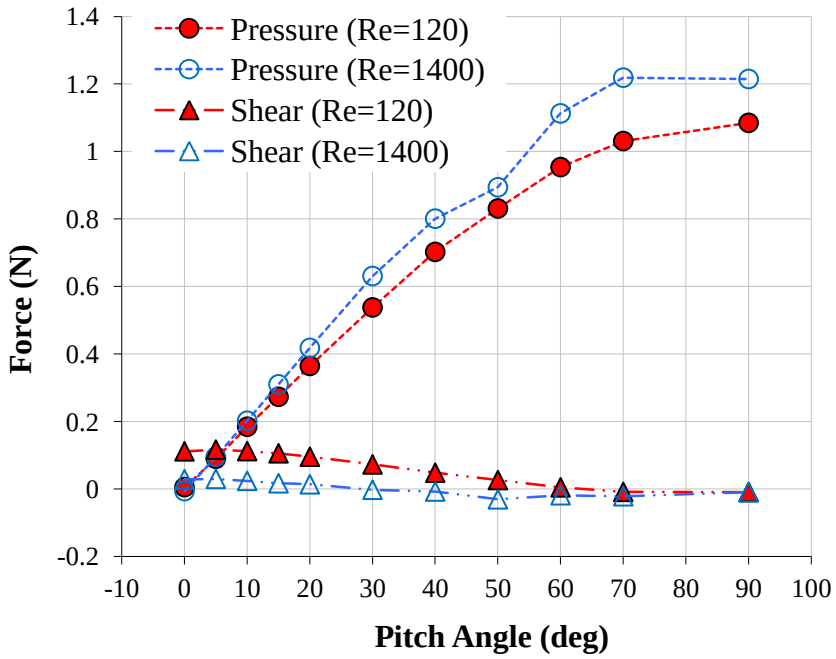

Figure 4.6: Computed pressure (normal) and shear (tangential) force variation with pitch angle for quasi-steady cases.

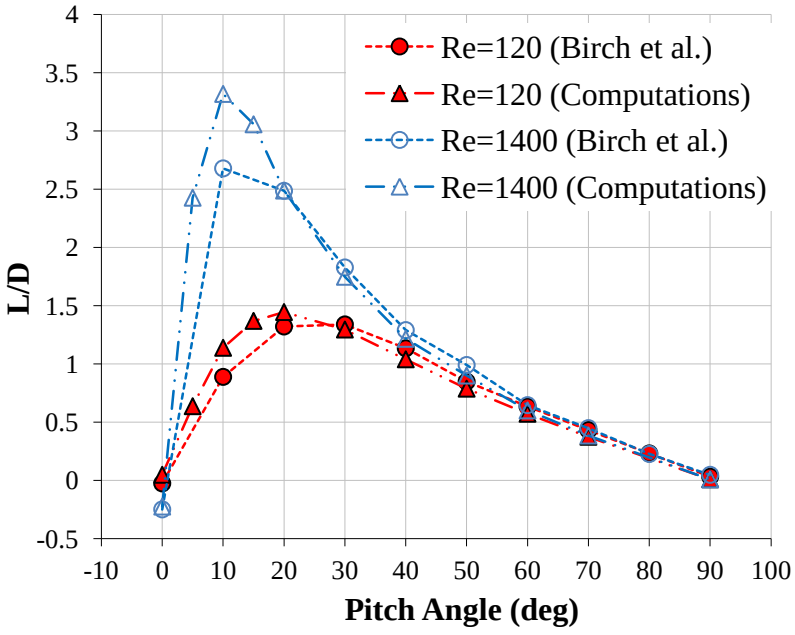

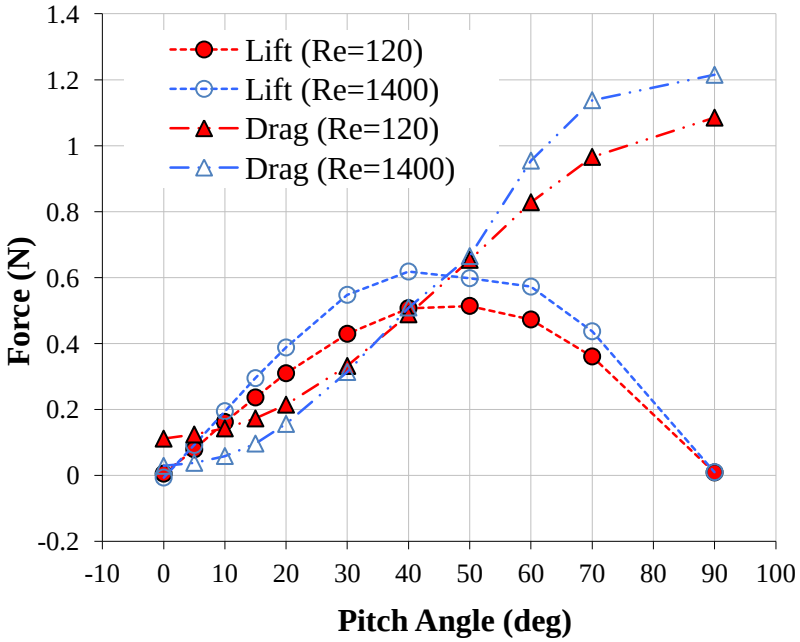

Figure 4.7: (top) Comparison of computed lift-to-drag ratio for impulsively started wing rotation at $Re = 1400$ and $Re = 120$ with the experimental results of Birch et al. [88]. (bottom) Computed lift and drag variation with pitch angle.

Figure 4.8 plots 2D streamlines for $Re = 120$ constrained to a plane parallel to and approximately 0.5 wing thicknesses above the upper surface of the wing. Similar in nature to oil-flow visualization experimental techniques, these surface plane visualizations are useful in identifying many phenomena such as separation and reattachment regions, the location and extent of tip vortex influence, and the strength of the surface spanwise flow. The low Re cases exhibit relatively simple flow patterns. As seen in Figure 4.8a, at $\alpha = 30°$ a small LEV is formed that remains attached and close to the leading edge through $r/R = 0.65$. Downstream of the LEV, the separated flow reattaches at approximately the 40% chord location. This attached flow is indicated in Figure 4.8a by streamlines with streamwise velocity components in the downstream direction. The attached region exists primarily over the aft portions of the wing. Closer to the leading edge, the streamlines show either a small or negative streamwise flow component which, for these simple cases, is indicative of a separated flow. For this low Reynolds number case, the spanwise flow reaches a peak in the trailing edge region and is thus not directly associated with the LEV. This tendency for insect-scale low *Re* flapping to generate peaks in spanwise flow that are not coincident with the LEV is similar to that noted previously by Birch [89]. Nevertheless, the outboard components of the streamlines in Figure 4.8a shows that the spanwise flow is still strong in comparison to the streamwise flow at the surface, even in regions where flow may be considered to be attached. Just downstream of the trailing edge, spanwise flow reaches a peak normalized value of 0.47 at $r/R = 0.65$ and 0.50 at $r/R = 0.75$. Increasing the angle of attack to 50^o results in a larger LEV with separated flow over the entire length of the chord. Although visible in Figure 4.10b, this separation is again shown in the surface

plane of Figure 4.8b by noting that the streamwise component of the streamlines is in the upstream direction over a majority of the wing. In Figure 4.9b note that the primary rotational motion constituting the LEV persists from $r/R = 0$ through $r/R = 0.65$, although as a prelude to it separating and turning to form the tip vortex, the rotational center has moved aft to approximately mid-chord. Outboard of this spanwise station, although not shown here, at $r/R = 0.75$ no distinct rotational center was observed. Spanwise flow velocity is slightly greater for this $\alpha = 50°$ case, with a peak value of 0.72 at $r/R = 0.65$ and 0.79 at $r/R = 0.75$.

Whereas the surface plane streamlines in Figure 4.8 at $Re = 120$ are essentially uniformly spaced and predominantly oriented in the same direction, the streamlines in Figure 4.11 at $Re = 1400$ indicate the more complex nature of the higher Re flow. Comparing the LEV as seen in Figure 4.9 to the respective LEV at each angle of attack in Figure 4.12, we see that the higher Reynolds number produces a more compact vortex with the characteristic highly centralized spanwise flow through its core. The most predominant difference in LEV structure at the two Reynolds numbers however are the secondary and tertiary vortices formed upstream of the primary LEV at $Re = 1400$. These are clearly visible in Figure 4.12a at $r/R = 0.55$, in Figure 4.12b at $r/R = 0.45$, as well as in Fig. 4.13. The development of these structures is well mapped by the topology of the streamlines in Figure 4.11, which for this higher Re shows surface patterns of streamlines that coalesce to form *ridges* and disperse to form *valleys*. At $\alpha = 30°$, three primary ridges ($R1 - R3$) and four valleys ($V1–V4$) indicate the size and position of the three LEV structures (shown in Figure 4.11a). Beginning at the wing root, only ridge $R1$ is present. Because this inboard portion of the wing is effectively acting at

a lower Reynolds number than outboard portions, a singular LEV is formed that separates at the leading edge and reattaches at $R1$. Indeed for a majority of the span, $R1$ serves as the demarcation between separated flow (above $R1$) and attached flow (valley $V1$, below $R1$). Near $r/R = 0.25$, $R1$ branches to form ridge $R2$ which marks the initial formation of a smaller vortex with the same rotational sense as the primary LEV. By $r/R = 0.50$, a secondary vortex is formed with the opposite rotational sense, as indicated by the branching of $R2$ to form $R3$. The three primary vortices that exist near mid-span inhabit valleys $V2$–$V4$. The vortices with the same rotational direction in $V2$ and $V3$ both show a strong positive spanwise flow at the surface. It is interesting to note however that the tertiary vortex that occupies $V4$ is associated with a zero or a slightly negative spanwise flow. This region extends towards the tip and expands to become a large region of low spanwise flow indicative of the separated region of the tip vortex. The primary LEV inhabiting valley $V2$ is bounded from above by this region of low spanwise flow and is turned towards the trailing edge beginning at approximately $r/R = 0.65$. Another indicator of the separation of the LEV is the dispersion of $R1$ at this same spanwise position. Even still, as seen in Figure 4.12a, the rotational center remains intact through $r/R = 0.75$.

At $\alpha = 50°$, the flow topology in Figure 4.11b is similar to the lower pitch angle case. In this case however, the bifurcation of the ridges occurs at earlier spanwise locations. At $r/R = 0.45$, the tertiary LEV as well as the $V4$ valley (which is larger and contains lower spanwise velocities than its lower angle of attack counterpart) are already well formed. For this case, the high positive spanwise flow in the $V2$ and $V3$ valleys extends over a greater portion of the surface and begins its turn towards the trailing edge

at approximately $r/R = 0.45$, occurring sooner than in the $\alpha = 30°$ case. This earlier separation is also highlighted by both the relatively rapid dispersion of the $R1$ ridge just before mid-span and the disappearance of the strong spanwise flow through the LEV at $r/R = 0.55$ (Figure 4.12b). After separation, there is an additional ridge, $R4$, which forms at the termination points of $R2$ and $R3$. This chordwise oriented ridge separates a region of low spanwise flow at the tip from the inboard sections. The rotating streamlines in this region, $V5$, are most likely associated with flow traveling out of the plane to join the tip vortex.

For $\alpha = 30°$, spanwise velocity reaches a peak of 1.25 at $r/R = 0.65$. At $\alpha = 50°$, spanwise velocity peaks at 1.61 at the more inboard $r/R = 0.45$ station, before a sharp decline in axial velocity that leaves the axial velocity at $r/R = 0.65$ at only 1.13. The location of peak velocity for the $\alpha = 50°$ case is also disassociated from the vortex center (Figure 4.12b), which indicates that the LEV begins to lose its coherent structure beginning near $r/R = 0.45$. Birch et al. [87] report that at $\alpha = 45°$ the peak axial velocity is approximately 1.52 at $r/R = 0.65$, indicating that the LEV remained coherent and attached at least up to that station for this slightly reduced pitch angle. In order to resolve this potential discrepancy and ensure that the loss of LEV structure at 50^o represents the simulation capturing a physical phenomenon instead of a numerically induced weakening of the vortex, the simulation was also performed at $\alpha = 45°$. For $\alpha = 45°$, spanwise velocity reaches a peak of 1.45 at $r/R = 0.65$, with the LEV remaining well-defined through $r/R = 0.65$. Therefore, the loss of coherent LEV flow outboard of $r/R = 0.45$ for $\alpha = 50°$ is likely a physical phenomenon, and this vortex breakdown in the quasisteady case begins between pitch angles of $45°$ and $50°$. Drag for

both values of Re is relatively insensitive with changes in pitch angle between 40° and 60°. Conversely, lift is most sensitive to changes in pitch angle across the same range. Correspondingly, in the next section describing the unsteady flapping simulations, it will be seen that the lift is more difficult to predict than drag during the pronation and supination points of the stroke, when the angle of attack of the wing changes rapidly across that range of pitch angles.

4.3.3 Power

Figure 4.14 plots the mean aerodynamic power required for a number of pitch angles for both values of Reynolds Number. It should be emphasized that these results are for aerodynamic power only and thus do not account for the inertial forces required to accelerate the wing. Therefore, for example, when plotting the power loading (Figure 4.15), the values will be higher than would be expected for physical systems. For these quasisteady cases, each set of data displays the expected increase in power with pitch angle. However, note that for α below approximately 15°, the higher Re case requires less power as a result of the lower shear drag in the less viscous and attached flow. Above $\alpha = 15°$, as the flow detaches at both values of *Re* and begins to form a small LEV, the lower pressure leading edge vortex of the higher *Re* case begins to dominate the power contribution, and the power required for the $Re = 1400$ case is consistently higher than the $Re = 120$ case. A similar result is seen in the lift and drag (Figure 4.7) where although the stronger LEV of the $Re = 1400$ case contributes to a greater lift across all angles of attack, the lower *Re* case benefits from lower quasisteady drag for angles of attack above 30°. These opposing effects result in similar power loading values between the higher and lower Reynolds number cases (Figure 4.15) for pitch angles between 25°

and $50°$ degrees. This range where power loading is less sensitive to *Re* is of prime interest to flapping wing drosophila hover, as the mid-stroke pitch angles are typically bounded within it. For pitch angles lower than 20°, the $Re = 120$ case's power loading decreases, where the power loading for the $Re = 1400$ case continues to increase until a peak at $\alpha = 10°$. Again, this is the result of the power falling more rapidly with decreases in α for lower angles of attack with the reduced viscous power losses.

Figure 4.14 and Figure 4.15 also plot a mean lift and power data point for the baseline flapping case to be discussed in the following chapter. It is interesting to note that the quasisteady predictions in this case are quite close to the *mean* unsteady predictions, in spite of the more complex kinematics and the resulting dynamic loading. This relationship will be explored further in the following chapter.

To better visualize the force and power generation by the wing, Figure 4.16 and Figure 4.17 plot the distribution of lift, drag and power *per unit area* on the upper surface of the wing for three pitch angles of the $Re = 120$ and $Re = 1400$ cases. In this context, power per unit area is the product of drag per unit area and the local rotational velocity. Note that in order to emphasize the qualitative relative location of zones of force generation, the contours in these plots are each normalized to their own local peak values. As a result, comparing the apparent magnitude of the contours across plots will be misleading.

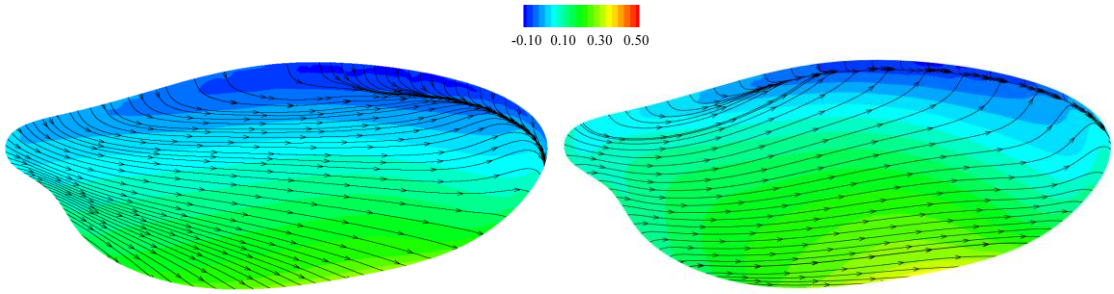

(a) (b)

Figure 4.8: Upper surface flow topology visualized by 2D streamlines constrained to a plane parallel to and approximately 0.5 wing thicknesses above the upper surface. Contours are of spanwise flow in the fixed inertial frame whereas streamlines are computed using the body-fixed frame velocity field. *Re* = 120, (a) $\alpha = 30^{o}$, (b) $\alpha = 50^{o}$.

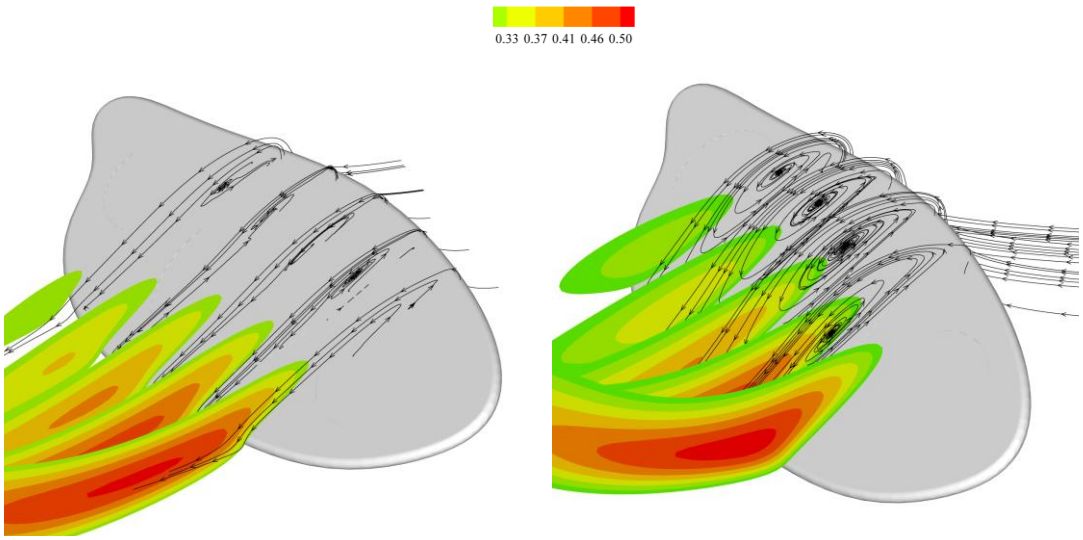

(a) (b)

Figure 4.9: 2D streamlines constrained to spanwise planes at *r/R* = 0.35, 0.45, 0.55, 0.65 and 0.75. For clarity, streamlines are not shown at all stations. *Re* = 120, (a) $\alpha = 30^{o}$, (b) $\alpha = 50^{o}$.

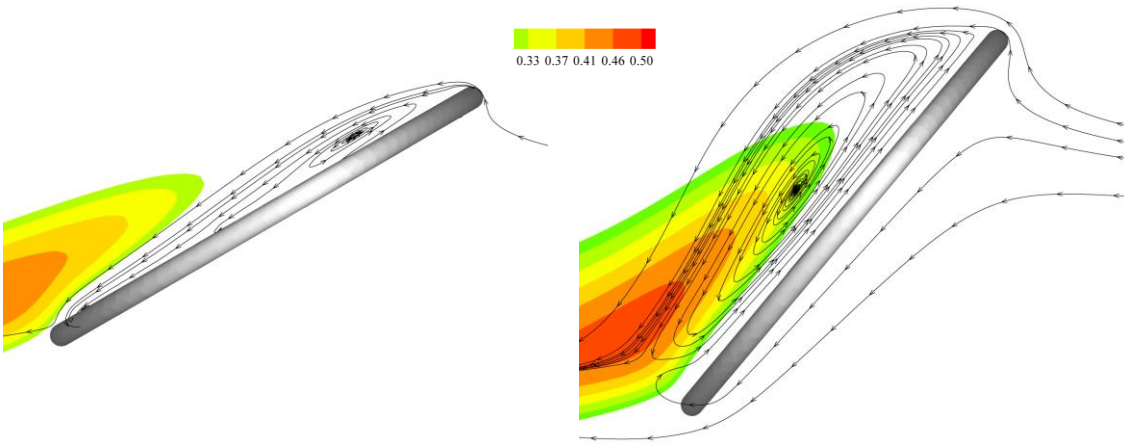

(a) (b)

Figure 4.10: Detail of r/R = 0.65 station from previous figure. Re = 120, (a) $\alpha = 30°$, (b) $\alpha = 50°$.

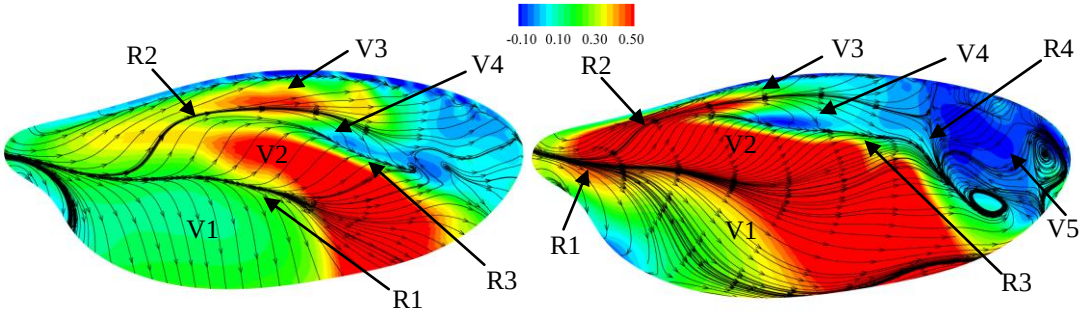

(a) (b)

Figure 4.11: Upper surface flow topology visualized by 2D streamlines constrained to a plane parallel to and approximately 0.5 wing thicknesses above the upper surface. Contours are of spanwise flow in the fixed inertial frame whereas streamlines are computed using the body-fixed frame velocity field. *Re* = 1400, (a) $\alpha = 30^o$, (b) $\alpha = 50^o$.

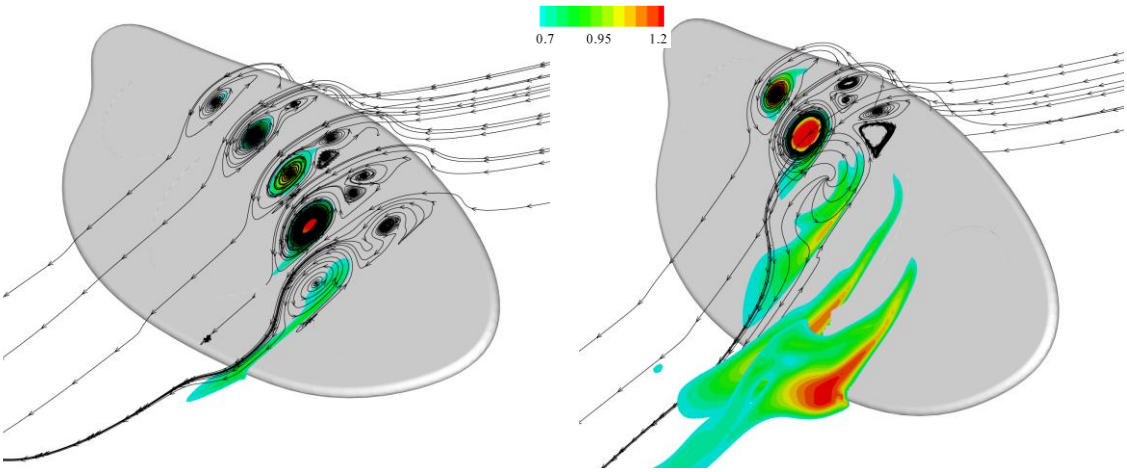

(a) (b)

Figure 4.12: 2D streamlines constrained to spanwise planes at *r/R* = 0.35, 0.45, 0.55, 0.65 and 0.75. For clarity, streamlines are not shown at all stations. *Re* = 1400, (a) $\alpha = 30^{o}$, (b) $\alpha = 50^{o}$.

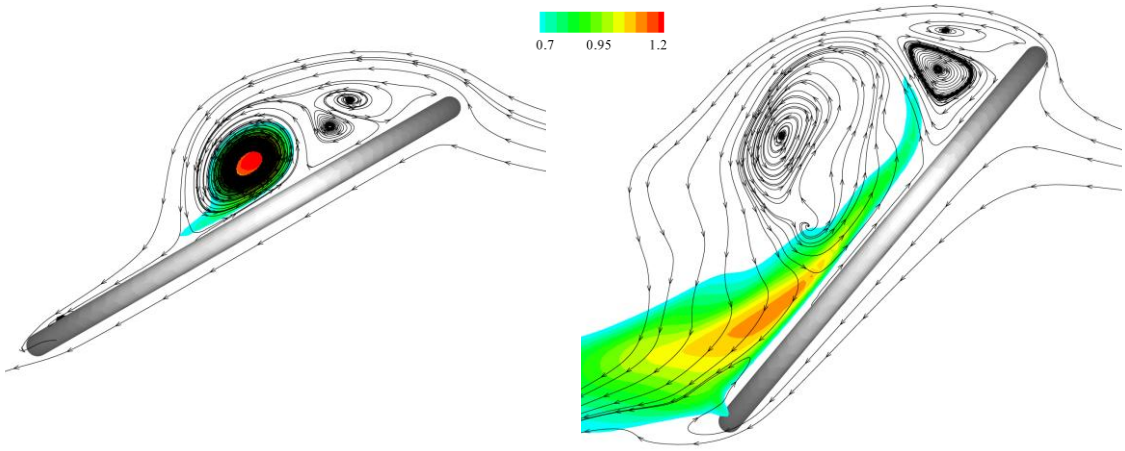

(a) (b)

Figure 4.13: Detail of *r/R* = 0.65 station from Figure 4.12. *Re* = 1400, (a) $\alpha = 30^{o}$, (b) $\alpha = 50^{o}$.

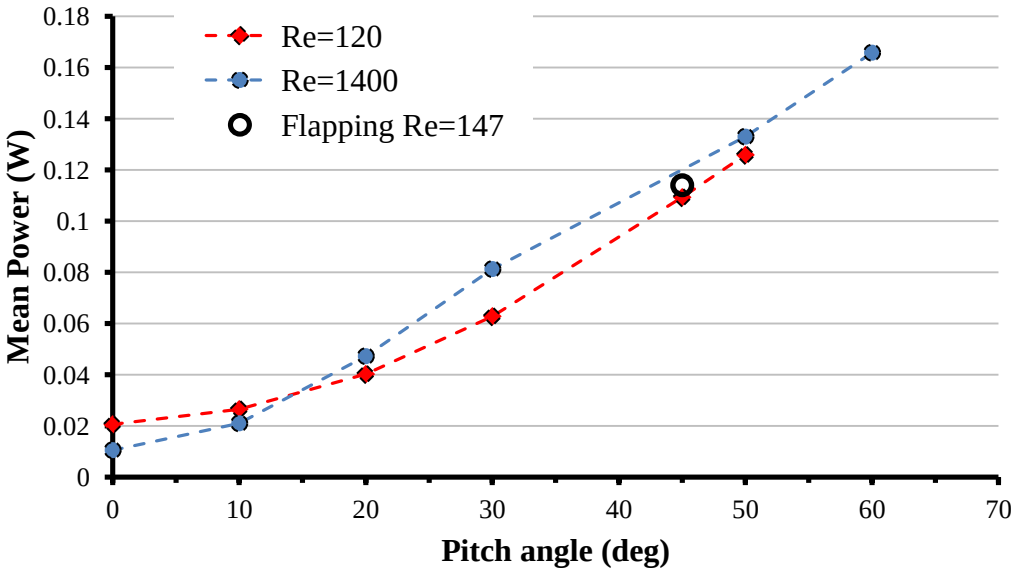

Figure 4.14: Mean power for impulsively started steady rotations at $Re = 120$ and $Re = 1400$. Mean power for the unsteady flapping simulation with a mid-stroke pitch of 45° is plotted as well for comparison.

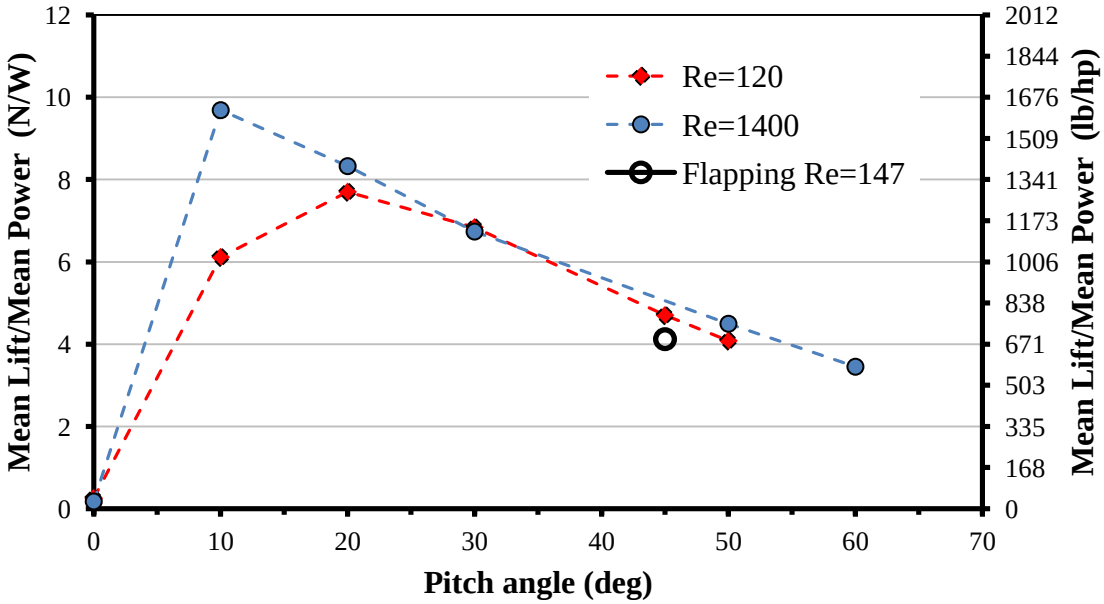

Figure 4.15: Lift to power ratio (power loading) for impulsively started wings rotation for $Re = 120$ and $Re = 1400$. Mean power loading for the unsteady flapping simulation with a mid-stroke pitch of 45° is plotted as well for comparison.

Pressure forces dominate shear forces, even for the low Reynolds number cases (this will be quantitatively shown in Chapter 5). Therefore, the regions of peak force generation correspond closely with the locations of the low pressure regions. In Figure 4.16 for the lower Re case, this manifests a large lift and drag generation region along the forward outboard portion of the wing, where the separation bubble seen in Figure 4.9 exists. For the higher Re case in Figure 4.17, the increase in magnitude of the low pressure region and the relative decrease in shear force influence makes the relationship between pressure and force even more apparent. Lift and drag begin being generated toward the inboard leading edge as the LEV forms, and the regions of peak force generation follow the path of the LEV from that edge to the aft outboard edge. This pattern is particularly pronounced at $\alpha = 50°$, and is indicative of the LEV path seen in Figure 4.12.

With increasing pitch angle on both the high and low Reynolds number cases, the effective spanwise location of forces tends to move inboard as an increasing amount of separation occurs on the inner portions of the wing. This effect seems to be more pronounced for the higher Re case, as compared with the lower Re case. That is, the spanwise location of the higher Re case is more inboard than the corresponding low Re case. This conclusion does not seem to agree with the predicted power. Note in Figure 4.7 that for pitch angles less than 40°, drag is lower for $Re = 120$ than for $Re = 1400$. However this is reversed for the power predictions seen in Figure 4.14. Since for this quasisteady rotation power is directly proportional the product of drag and local tangential velocity, and rotational velocity is fixed between the two Reynolds number cases (fluid viscosity is changed), then the increase in power for the $Re = 1400$ case

would indicate that the effective spanwise location of drag has moved *outboard* where its product with the higher tangential velocities would be larger. Similarly, comparing Figure 4.15 of mean lift/power to the lift/drag plot in Figure 4.7, it is seen that the power ratio is similar for the two Reynolds numbers for pitch angles greater than 20°. However, the lift/drag ratio is predicted to be much higher in the $Re = 1400$ case than at $Re = 120$ below pitch angles of 40°. Again, this conclusions seems counterintuitive when compared with the apparent spanwise locations of the peak force and power locations in Figure 4.16 and Figure 4.17.

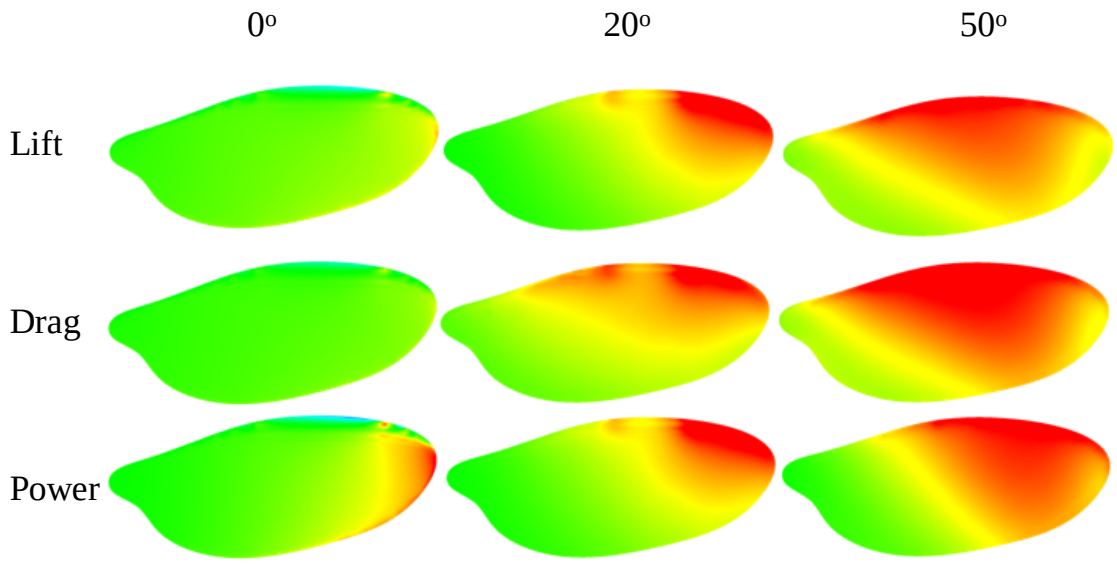

Figure 4.16: Distributions of lift, drag, and power per unit area on the upper surface of the wing for the 0°, 20° and 50° cases. $Re = 120$. Note: each image contour values individually scaled to better highlight peak force locations.

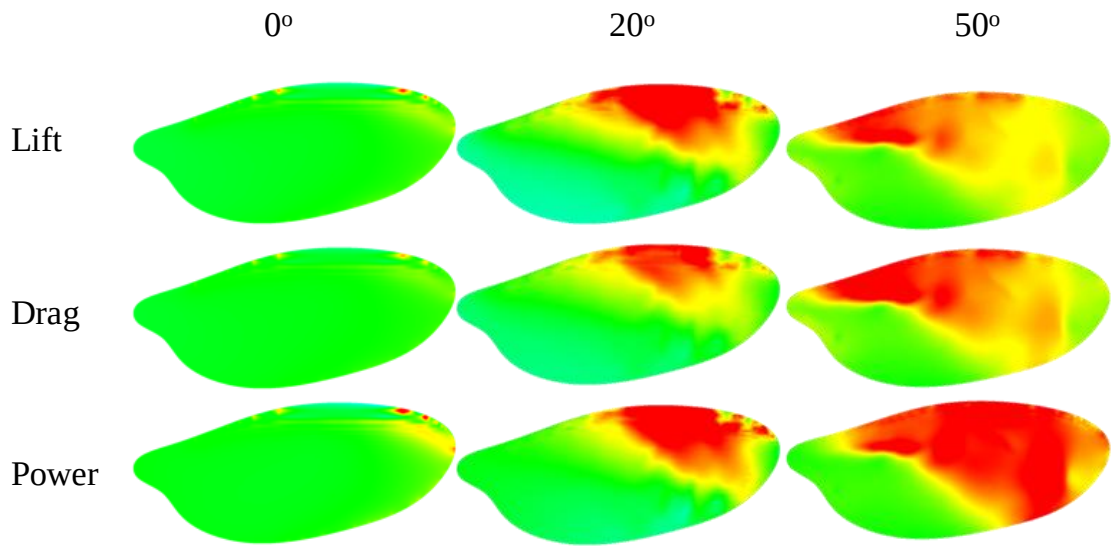

Figure 4.17: Distributions of lift, drag, and power per unit area on the upper surface of the wing for the 0°, 20° and 50° cases. $Re = 1400$. Note: each image contour values individually scaled to better highlight peak force locations.

4.4 Summary

The computed lift-to-drag agreed well with experimental results found in literature. In general, the largest discrepancies appeared in the lift computations, which is potentially the result of the artificially thicker computational wing.

A steady LEV was observed for all cases at pitch angles above 10°, the size, strength and shape of which varied significantly with Reynolds number and pitch angle.

- At $Re = 120$, the change in α from 30° to 50° produced a marked effect on the size of the separated flow region and a 60% increase in peak spanwise velocity. The LEV spanwise separation point was however not significantly affected by the change in angle of attack.

- At $Re = 1400$, the structure of the LEV was found to strongly depend on the spanwise station. Inboard sections exhibited the typical singular separation vortex, however near $r/R = 0.25$ for $\alpha = 30°$, a smaller vortex formed which bifurcated by $r/R = 0.55$ to form a secondary vortex to the primary LEV. This vortex system remained relatively intact through r/R = 0.75 although the chordwise position of the LEV rapidly shifted towards the trailing edge after $r/R = 0.55$. At $\alpha = 50°$, a similar LEV structure was found, however, the strong centralized spanwise flow that remained present through $r/R = 0.65$ in the lower angle of attack case dispersed before $r/R = 0.55$ at $\alpha = 50°$. The tertiary vortices, as well as a weak rotational LEV region were still present at the $r/R = 0.65$ station.
- A concentration of spanwise flow was observed for all cases with a LEV. For the $Re = 120$ cases, the peak spanwise flow was found just aft of the wing's trailing edge, and it was not coincident with the center of the LEV. In the $\alpha = 30°$ case, the peak spanwise velocity was 50% of the tip velocity. For the $\alpha = 50°$ case, the peak spanwise velocity reached 79% of the tip velocity. At the higher $Re = 1400$, the peak in spanwise velocity centered in the LEV. For the $\alpha = 30°$ case, the peak spanwise velocity was 125% of the tip velocity. For the $\alpha = 50°$ case, the peak spanwise velocity was found to be 161% of the tip velocity, although this occurred farther inboard, at the 45% span location, than other cases. However this result seems consistent with similar experimental results [87].

Power requirements increase with increasing pitch angle at a similar rate at both Reynolds numbers above $\alpha = 15°$. Below this, the predicted power curves cross and the mean power for the lower *Re* case, becomes larger than for the higher *Re* case. Peak L/P is higher for the $Re = 1400$ case, and does not taper off with decreasing pitch angle until $10°$, where for the $Re = 120$ case, the peak occurs at the higher $20°$ pitch angle.

Comparisons of drag and power predictions between the two Reynolds number cases seem to indicate that for pitch angles below $40°$ the spanwise location of the drag peak must move outboard with increased Re. However, flow visualization at the wing's upper surface appear to indicate that the peak spanwise location moves *inboard* with increases in Re.

4.5 Conclusions

These quasisteady results serve as a validation of the methodology's ability to predict unsteady forces in low *Re* unsteady flows, however the key understanding to be gained from this chapter's computational results are the sensitivities of the forces and flowfield to changes in pitch angle and Reynolds number in a *quasisteady* sense for these low values of *Re*.

Between pitch angles of $0°$ to $40°$, Reynolds number has a strong effect on the magnitude of L/D, with the larger $Re = 1400$ cases showing more than twice the L/D ratio of the L/D of the $Re = 120$ cases at their peaks. These peaks were also shifted to lower values of pitch angle for the higher Reynolds number. This would indicate that the higher *Re* case begins the post stall lift recovery more rapidly than the lower *Re* case. Above $40°$, as the wings move deeper into the post-stall regime, the L/D curves collapse

as both approach bluff body flow. For the baseline flapping motions examined in the next chapter, the wings remain at constant pitch angles of 45° or less throughout a majority of the stroke, with departures to higher pitch angles only when flipping to reverse the stroke direction. In a quasisteady sense, it would follow then that L/D over a majority of the stroke should be higher for the higher *Re* cases, but near stroke reversal the forces should be similar. Similarly, in a quasisteady sense, we could conclude that and optimal steady stroke angle for the flapping cases should be between 10° to 20° to maximize L/D and minimize power per unit of lift. In the next chapter we will see how the unsteady flowfield affects these quasisteady predictions.

Chapter 5 –

Flapping Simulations

With the conclusions drawn about the quasisteady forces and flowfield, we can begin to generate a more realistic flapping simulation by adding unsteady pitching and rotational kinematics. The unsteady flapping simulation results are organized in three major parts.

(1) Flapping kinematics based on an experimental study by the Dickinson Lab at Caltech conducted on the Robofly flapping apparatus serve as a baseline low Reynolds number simulation case. The wake structure and unsteady forces generated in this baseline case are detailed.

(2) To build on these conclusions and to facilitate comparison with the quasi steady results from the previous section, the $45°$ mid-stroke angle of the baseline case is modified to $20°$ and $30°$.

(3) Finally, the baseline simulation kinematics are repeated with the higher Reynolds number LES solver at $Re = 1400,$ again to facilitate comparison with the quasisteady results, but also to study the difference in the flowfield at Reynolds numbers closer to what hovering MAVs experience.

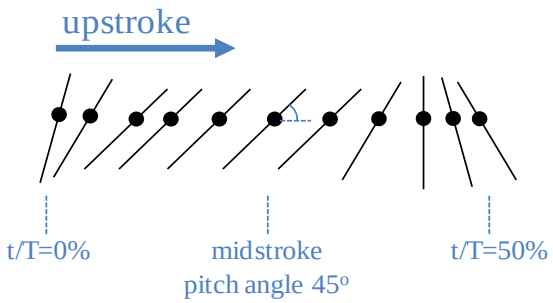

Figure 5.1: Stroke schematic depicting the kinematics of the baseline flapping case. The dots indicate the position of the pitch axis.

5.1 Baseline Flapping Cases

As compared to the quasisteady cases, the actual wing motion for typical insects in hover is generally complex, including passively deformable thin wings, asymmetric strokes, and a tip path that deviates from the stroke plane in an irregular manner [11]. Because of the difficulty involved with measuring and reproducing these kinematics, capturing the salient flow features of the actual stroke becomes more practically tenable if an idealized motion is adopted [14]. The present baseline idealized insect wing motion consists of a model *Drosophila* wing translating in rotation through a $\Phi = 180°$ arc at a nearly constant angular velocity and geometric angle of attack, $\alpha = 45°$, except near the stroke reversal points at the ends of the arc in which the wing flips (pitches) about an axis at 45% chord (Figures 5.1 and 5.2). The pitching axis remains in the stroke plane throughout the motion and the up and downstroke arcs are kinematically symmetric. The idealized stroke motion uses an 'advanced' flip, in which the midpoint of the flip, $\alpha = 90°$, occurs before the wing reaches the end of the upstroke (pronation) or the end of the downstroke (supination). This class of idealized flip timings, as opposed to a 'symmetric' flip or a 'delayed' flip, in which the mid-point of the flip occurs at or after

stroke reversal, has been experimentally [14] and computationally [90], [34] found to give the largest mean force values for this idealized motion. The cause of this will be explored in the subsequent sections, but we have already seen with the quasisteady results from Chapter 4 that peak lift occurs near a pitch of 45°. Furthermore, with regard to the unsteady forces, at stroke reversal, a mid-stroke pitch angle of 45° positions the wing at an angle of attack well-suited to take advantage of vorticity generated from the previous stroke; this is the so-called 'wake capture' effect.

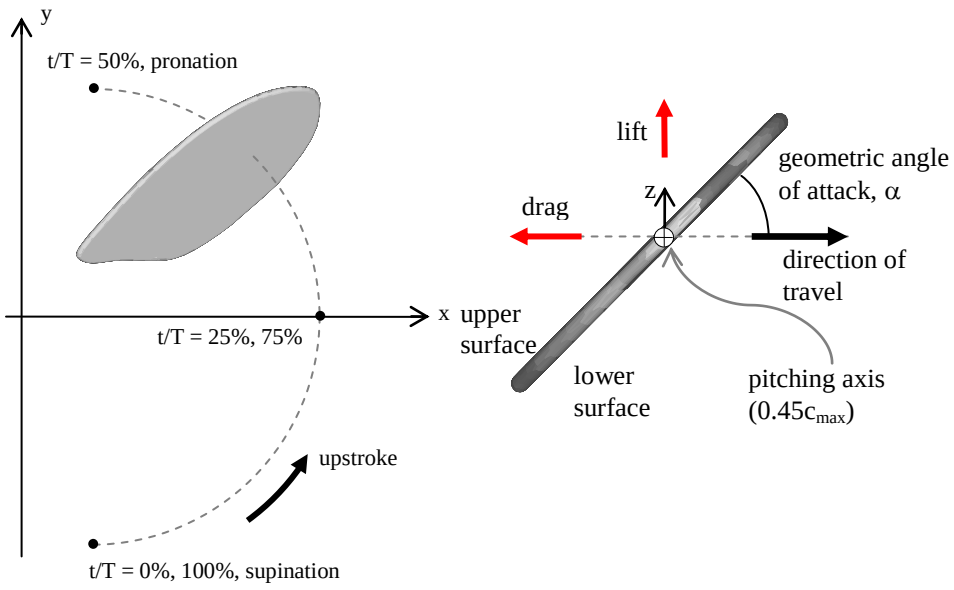

Figure 5.2: Illustration of conventions used throughout this work. The upper surface is defined as the surface opposite the direction of travel. The geometric angle of attack, α, is defined with respect to the direction of travel, thus it's time history is discontinuous at supination and pronation

5.1.1 Computational Setup

The present simulation flow conditions for the baseline flapping case correspond to the experimental conditions of Birch and Dickinson [17] on the Robofly apparatus with the exception that the present computational flapping motion and the experimental data obtained directly from the Dickinson Lab used for comparison traverse a full 180^o flapping arc (as opposed to the 160^o of the experiment documented in [17]). The wing planform is similar to the quasisteady cases, having a single-wing dimensional surface area of $S = 0.0167m^2$ with a total wing radius of $R = 0.25m$. The inboard 24% of the experimental wing was taken up by the presence of the mounting apparatus and force measurement devices. Since these are not required by the computations, the inboard portion of the wing profile, which is not present in the experiment, is approximated based on the rough shape of a typical *Drosophila* wing. The resulting computational wing has a spanwise length of $R - R_c = 0.22m$, compared with the $R - R_c = 0.19m$ of the experiment, which means that approximately the outboard 76% of the wingspan profile is matched to the actual wing geometry. The experiments are conducted in oil with a kinematic viscosity of 1.2×10^{-4} m^2/s and a density of $880kg/m^3$. Based on the mean tip velocity, these conditions lead to a Reynolds number of approximately *Re* = 147. No image/symmetry plane or second wing is used in either the experiment or the CFD.

The wing is assumed to be rigid and the thickness of the present computational model is taken to be 4.5mm, approximately 2 times the experimental value. The primary computational mesh contains 33.5×10^6 nodes with a uniform resolution over the wing path of 1.25mm. The mesh used for flow visualization of the wake used the same near

body resolution, however the more finely resolved wake region below the stroke plane required a 37.1×10^6 node mesh.

The experimental full stroke period was approximately T = 5.89s (f = 0.170Hz), which given the specific kinematics described below, resulted in a peak rotational angular velocity of 1.182 rad/s during the stroke. At mid-stroke ($\tau = t/T = 25\%, 75\%$) the wing translates at a constant angular velocity and geometric pitch angle, $\alpha = 45°$. At some time $\tau_{0,f}$, the wing begins to flip about its pitching axis, reversing its pitch angle for the next half stroke (Figure 5.3). The mid-point of this flip, where the geometric angle of attack is $\alpha = 90°$, occurs at τ_f, and the total flip time is $\Delta\tau_f$. Note that the plotted pitch angle function in Figure 5.3 is not continuous at the mid-stroke due to the definition of α with respect to the direction of rotation. The rotational translation is defined by the time that deceleration begins, $\tau_{0,r}$. To ensure smooth transitions between the steady rotational portions of the stroke and the accelerating portions near stroke reversal, the angular acceleration functions themselves are defined such that they are smooth and continuous over the entire stroke. Analytically integrating the trigonometric acceleration functions gives the angular pitch and rotation velocities. As an example, the equations for the stroke reversal occurring at $\tau = 1$ are given by Equation (5.1),

$$\dot{\alpha}(\tau) = \begin{cases} \dfrac{T\,\ddot{\alpha}_{max}}{2}\left[\tau - \tau_{0,f} - \dfrac{1-\tau_{0,f}}{2\pi}\sin\left(2\pi\dfrac{\tau-\tau_{0,f}}{1-\tau_{0,f}}\right)\right]; \\ \qquad \text{where} \qquad \tau_{0,f} < \tau < \tau_f \\ 2\dot{\alpha}_{max} - \dfrac{T\,\ddot{\alpha}_{max}}{2}\left[\tau - \tau_{0,f} - \dfrac{1-\tau_{0,f}}{2\pi}\sin\left(2\pi\dfrac{\tau-\tau_{0,f}-\tau_f+1}{1-\tau_{0,f}}\right)\right]; \\ \qquad \text{where } \tau_f < \tau < \tau_{0,f} + \Delta\tau \end{cases} \tag{5.1}$$

$$\omega(\tau) = \frac{\mathrm{T}\,\ddot{\phi}_{max}}{2}\left[\tau - 1 - \frac{1-\tau_{0,r}}{\pi}\sin\left(\pi\frac{\tau-\tau_{0,r}}{1-\tau_{0,r}}\right)\right]; \quad where\ \tau_{0,r} < \tau < \tau_{0,r} + \Delta\tau_r \tag{5.2}$$

where $\dot{\alpha}_{max}$, $\ddot{\alpha}_{max}$, and $\ddot{\phi}_{max}$ are constant functions of the total pitch angle change per stroke, α_{total} (the total rotational angle change), Φ, and the period per stroke, T:

$$\dot{\alpha}_{max} = \frac{\mathrm{T}}{2}\ddot{\alpha}_{max}(1-\tau_{0,f}) \tag{5.3}$$

$$\ddot{\alpha}_{max} = \frac{2\alpha_{total}}{\mathrm{T}^2(\frac{1}{2}(1+\tau_{0,\mathrm{f}}^2) - \tau_{0,\mathrm{f}}^2} \tag{5.4}$$

$$\ddot{\phi}_{max} = \frac{2\Phi}{\mathrm{T}^2\left[(1-\tau_{0,\mathrm{r}})\left((1+\tau_{0,\mathrm{r}}) - \frac{4(1-\tau_{0,\mathrm{r}})}{\pi^2} - 2\right) + (1-2\tau_{0,\mathrm{r}})\right]} \tag{5.5}$$

In the context of the simulations, these angular velocity functions are then numerically integrated using either a 3rd order Runge-Kutta scheme or a second order Adams-Bashforth scheme (remaining consistent with the time integration of the convective terms) to obtain the angular position and angle of attack at a given time. The resulting position functions are C^3 continuous, however the kinematic patterns used in the experiment are formed using low pass filters on triangular and trapezoidal waveforms [14], thus the present functions will not exactly match those of the experiments. However, by choosing appropriate values of the flip and translation parameters, the total L_2 norm of the difference per full stroke between the present position functions and the experimental kinematics has been reduced to less than 0.81^o for pitching, and less than 0.60^o for the rotational position (azimuth). It should be noted that the maximum instantaneous errors in prescribed position, and consequently velocity and acceleration, occur near stroke reversal where the effects of these errors may be most significant. Emblemsvåg and Candler [44] showed that even minor variations in the pitching

description can change the force peaks, lift more so than drag, quite significantly (approximately 25% change in lift peaks near stroke reversal in some cases).

For all cases in Sections 5.1and 5.2, simulations are run with a maximum CFL of 0.3 for the AB2 scheme, and a max CFL of 0.75 for the RK3 scheme. The residuals on the pressure Poisson equation are converged a minimum of 3 orders of magnitude for each time step.

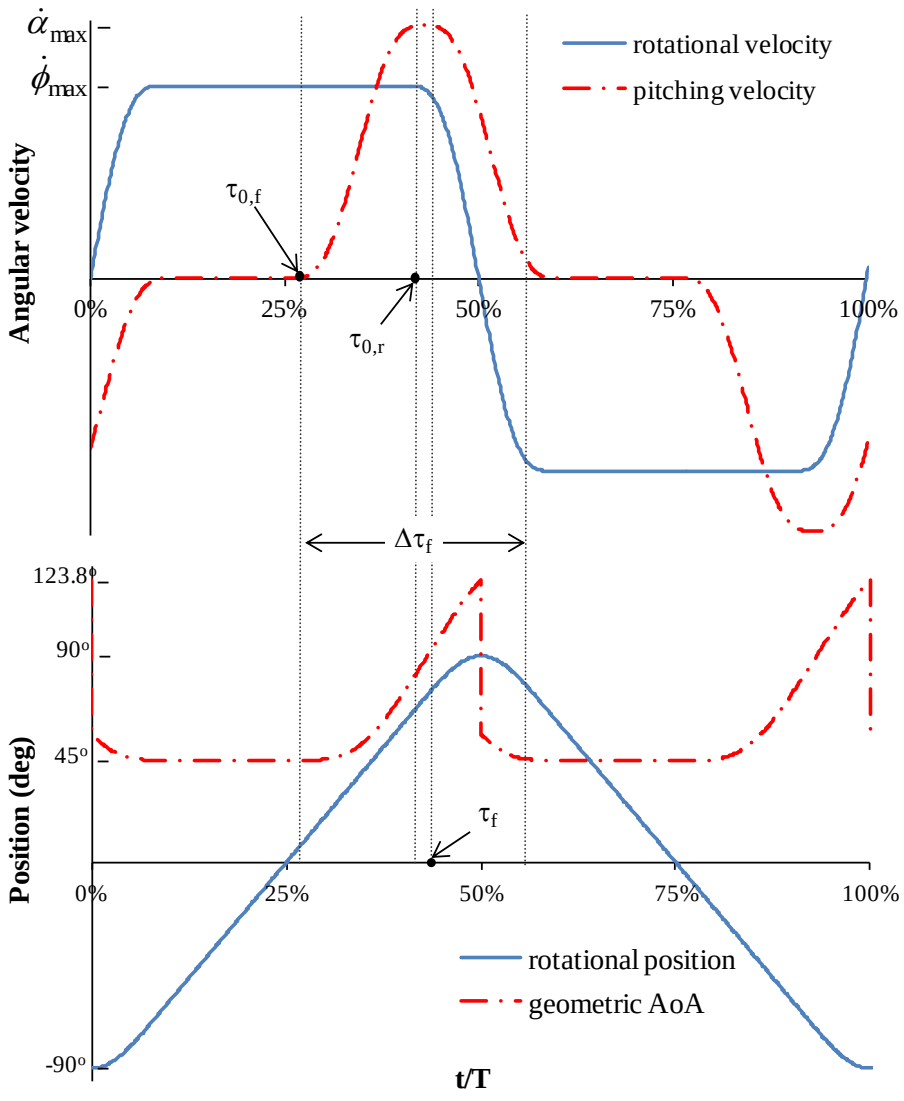

Figure 5.3: Kinematics description of pitching and rotational position and velocity.

5.1.2 Results and Discussion

The force time histories (Figure 5.4) and the flow visualizations to be presented will be those obtained during the fourth full stroke for all computations and the experiment, unless otherwise noted. For most cases, simulations were actually computed through eight full strokes, however comparison of later cycles with the third and fourth strokes revealed no significant differences in forces or nearfield flow structures (Figure 5.5). This rapid stabilization of the flowfield is due in part to the rapid convection of the initial starting vortices away from the stroke plane, as will be discussed later. It should be noted that while the up and downstrokes in the computations were symmetric by even the second full cycle as one would expect, the force time histories from the experiment never appeared to reach a fully symmetric up/down stroke cycle. From computational experimentation, the asymmetries are consistent with slightly differing mid-stroke pitch angles on the up and down strokes, however this could also indicate some recirculation or boundary effects from the experimental oil tank, some inaccuracies in the mechanical device's kinematics or force measurement errors.

5.1.2.1 Stroke Description

Figure 5.6 presents pressure contours, body-frame streamlines, and spanwise vorticity contours at the 60% span location at specific times within the stroke. At each of these times, Figure 5.6 also shows the corresponding spanwise vorticity isosurfaces. Figure 5.7 gives the surface distribution of nondimensional pressure relative to freestream at the 60% span.

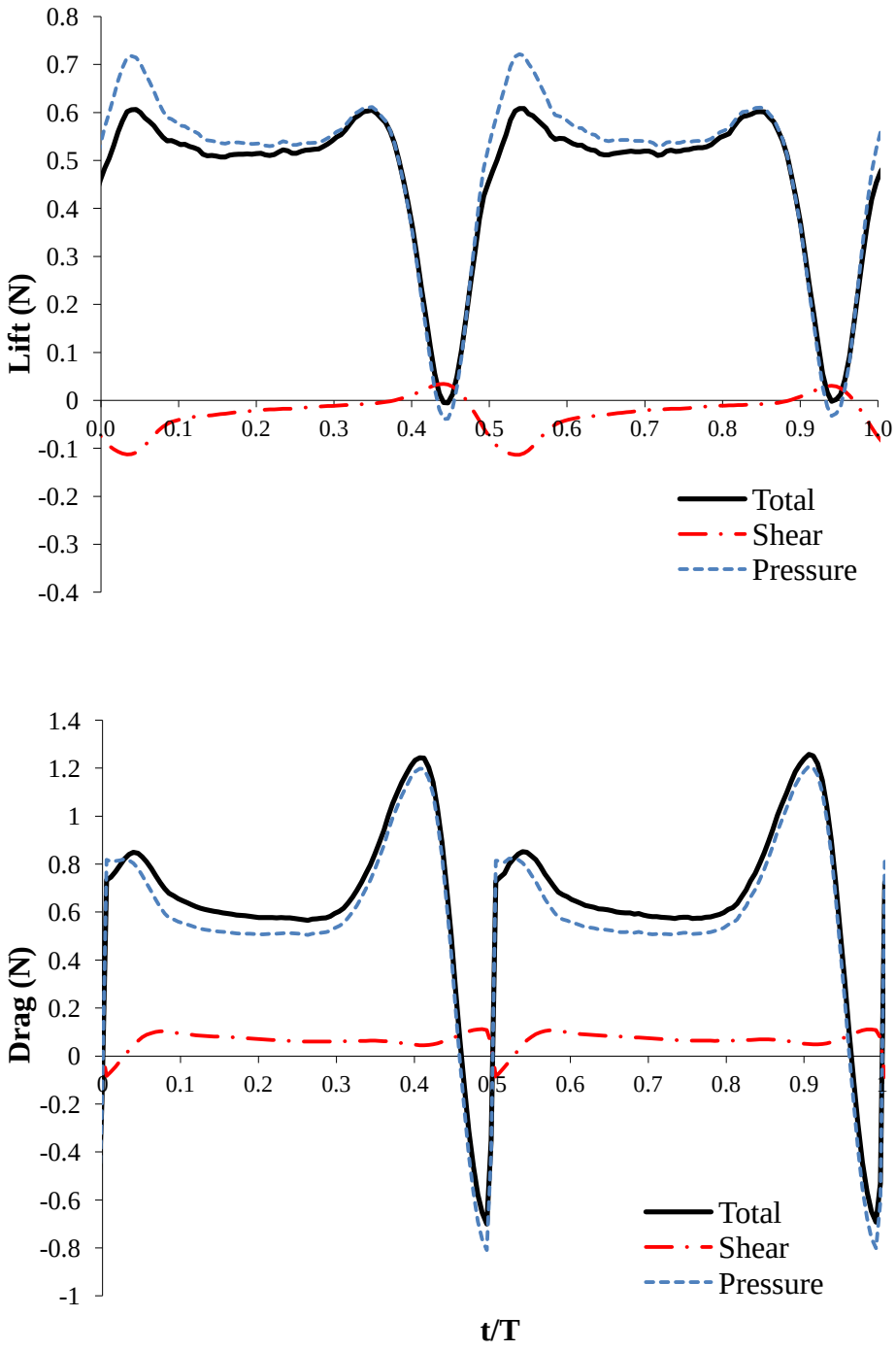

Figure 5.4: Computed forces for the baseline flapping case decomposed into pressure (normal) and shear (tangential) components.

At 9% of the upstroke, the wing finishes the rotational acceleration started after supination (stroke reversal after downstroke), and begins a constant angular velocity rotational translation. Similar to a fixed wing linear translation, the rotating wing develops and sheds a starting vortex at the trailing edge, as can be seen in the spanwise vorticity contours of Figure 5.6a. The corresponding spanwise vorticity isosurfaces in Figure 5.6a show the expected leading edge and starting vortices, however the starting vortex is clearly distorted near mid-chord. As will be shown in Section 5.1.2.3, this twisting is a result of an interaction with the root vortex and other shed vortices of the previous half stroke.

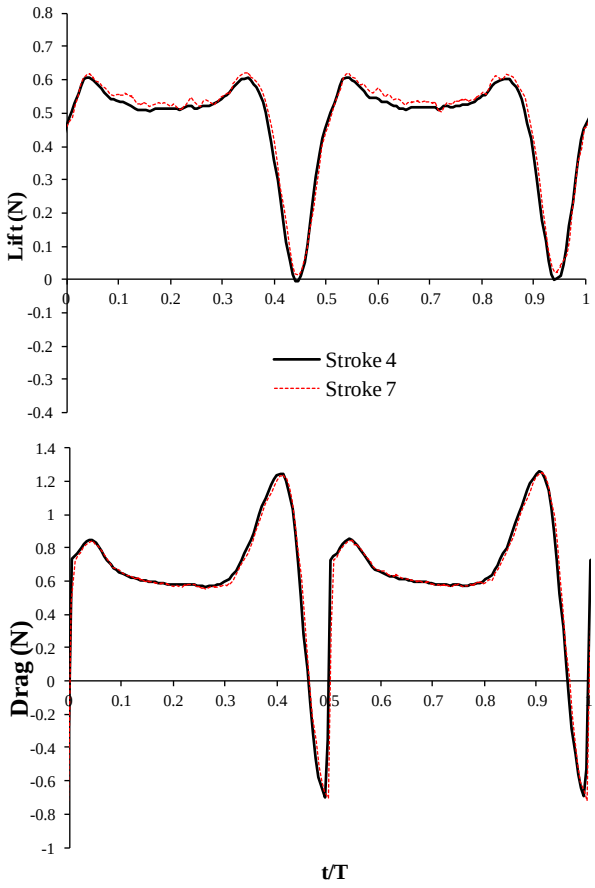

Figure 5.5: Computed force time histories for strokes 4 and 7 of the baseline case demonstrating periodicity is achieved after 4 strokes

The wing finishes its supination flip from the previous downstroke at t/T = 10%, after which it remains at a constant 45^o geometric angle of attack until t/T = 26%. During this steady rotation (Figure 5.6b – c) which covers 64.5^o of azimuth, the low pressure zone associated with the LEV grows with the vortex such that by t/T = 24.5% the zone spans from the leading edge to approximately mid-chord (at the 60% span location in Figure 5.6c). The flowfield is notably similar to that of the $Re = 120$, $\alpha = 50°$ quasisteady case shown in Figure 4.9 with an attached LEV through about 75% span. The lift and relative surface pressure is reasonably stable during this steady rotation portion of the stroke, with a linear increase of pressure along the wing upper surface aft of the suction peak, and the corresponding linear decrease of surface pressure aft of the stagnation point on the lower surface (Figure 5.7a). The peak suction pressure drops 10% between t/T=16% and 24.5%, accompanying the gradual decay of the pressure-lift (Figure 5.7), however shear-lift increases, as the recirculation region grows to cover a progressively larger portion of the upper surface of the wing. Total lift remains relatively constant, since this gradual increase in shear-lift roughly balances the falling pressure-lift. Because the wing is at a constant $\alpha = 45°$, the pressure-drag decreases in a manner similar to the pressure-lift. However, since the recirculation region provides some amount of negative viscous-drag, and the size of the attached region is roughly inversely proportional to the size of the recirculation region at each spanwise station, the shear-drag also decreases, which results in a gradual but steady decrease of total drag over this portion of the stroke.

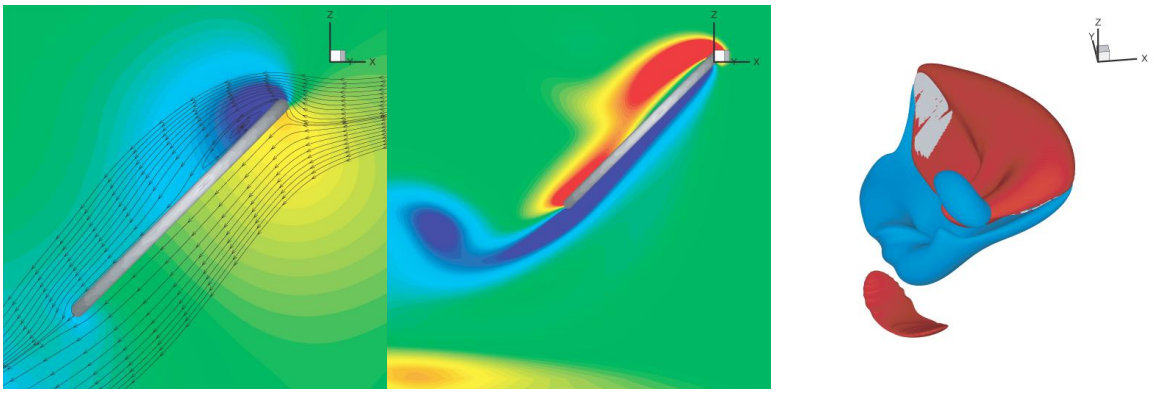

(a) Pressure contours, spanwise vorticity contours, spanwise vorticity isosurfaces at t/T = 9%

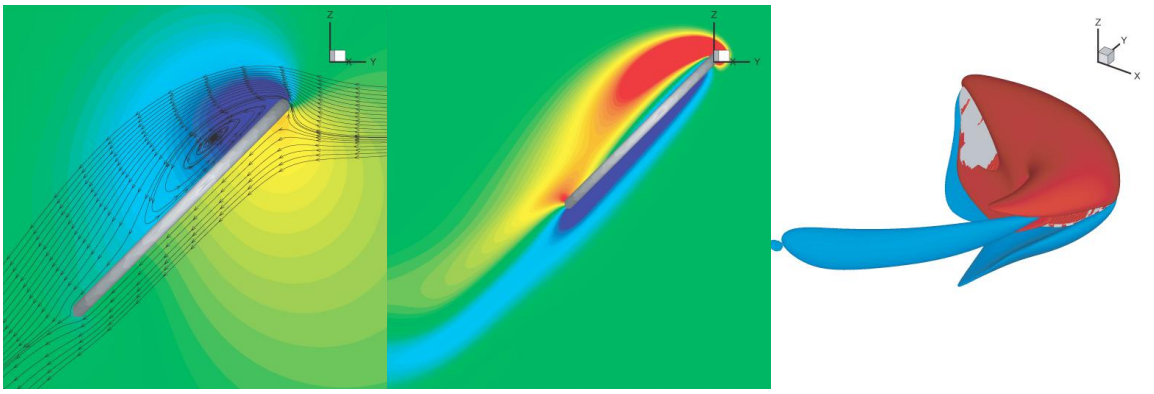

(b) Pressure contours, spanwise vorticity contours, spanwise vorticity isosurfaces at t/T = 16%

Figure 5.6: Left: Pressure contours ($P - P_\infty$) at various times covering the steady rotation and flipping portions of the stroke (blue, negative). Streamlines are computed in the body-fixed frame, and as shown are constrained to the plane (60% span). Streamlines are not shown at all times for clarity. Center: Corresponding spanwise vorticity contours (red, counter-clockwise) at the 60% span location. Right: Corresponding spanwise vorticity isosurfaces (red, counter-clockwise).

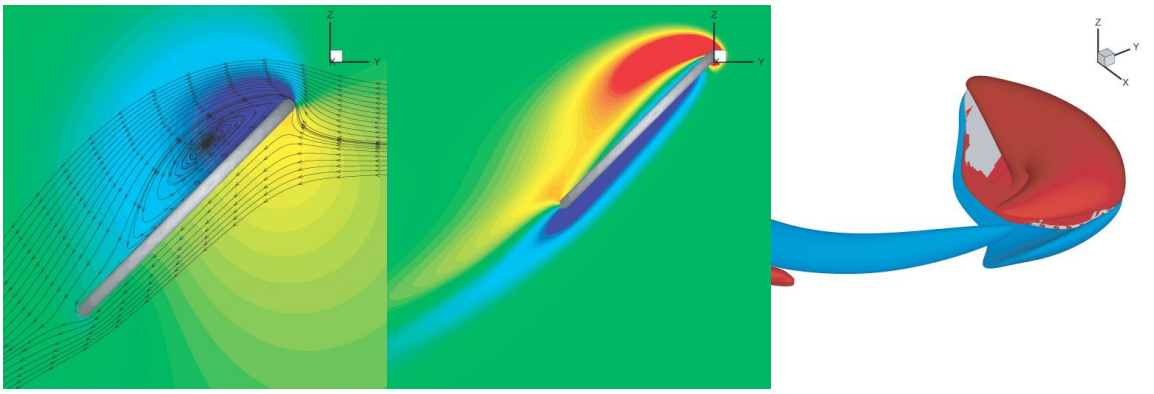

(c) Pressure contours, spanwise vorticity contours, spanwise vorticity isosurfaces at t/T = 24.5%

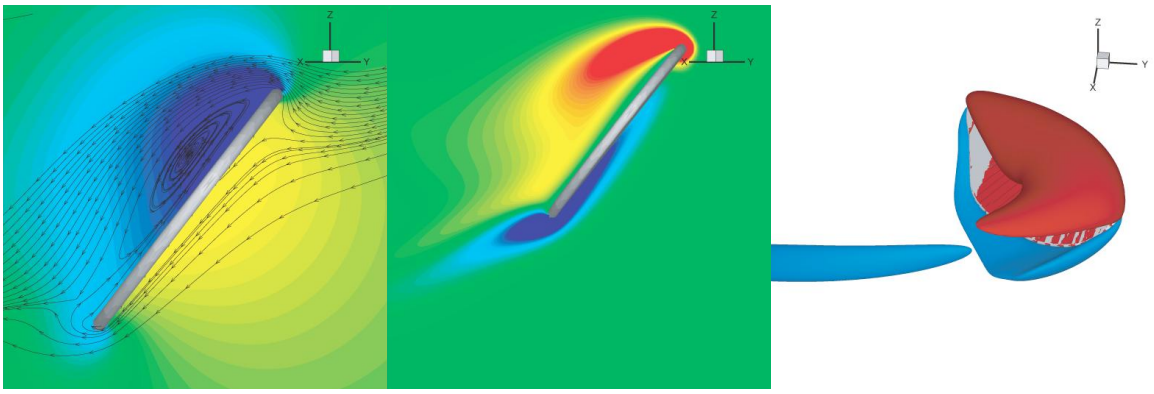

(d) Pressure contours, spanwise vorticity contours, spanwise vorticity isosurfaces at t/T = 34.5%

Figure 5.6 (continued): Left: Pressure contours ($P - P_\infty$) at various times covering the steady rotation and flipping portions of the stroke (blue, negative). Streamlines are computed in the body-fixed frame, and as shown are constrained to the plane (60% span). Streamlines are not shown at all times for clarity. Center: Corresponding spanwise vorticity contours (red, counter-clockwise) at the 60% span location. Right: Corresponding spanwise vorticity isosurfaces (red, counter-clockwise).

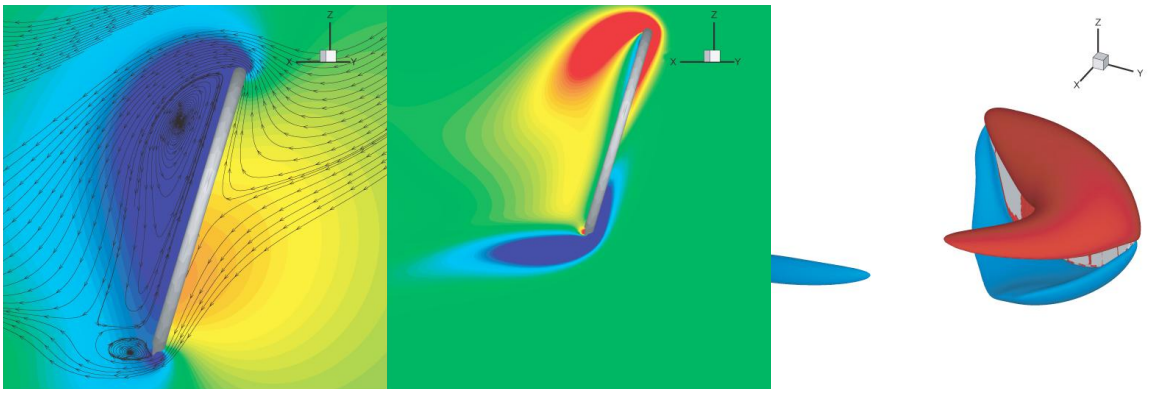

(e) Pressure contours, spanwise vorticity contours, spanwise vorticity isosurfaces at t/T = 40%

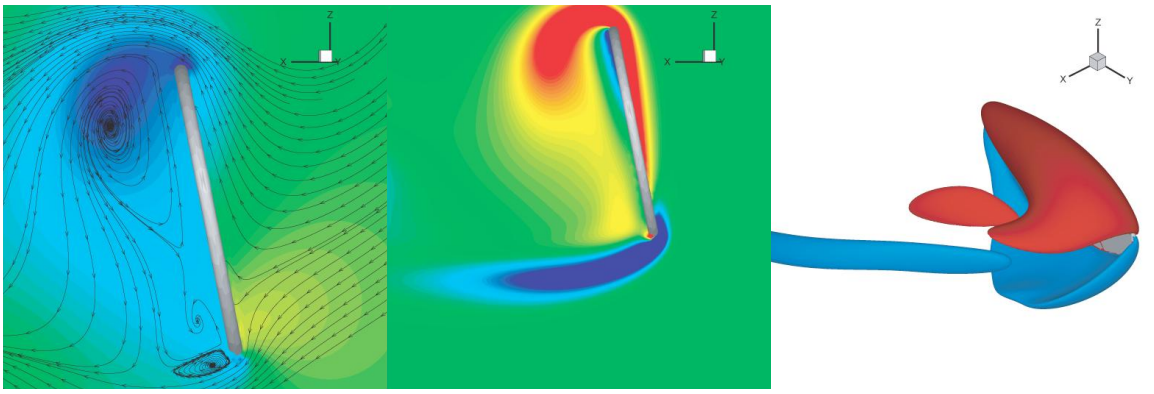

(f) Pressure contours, spanwise vorticity contours, spanwise vorticity isosurfaces at t/T = 45%

Figure 5.6 (continued): Left: Pressure contours ($P - P_\infty$) at various times covering the steady rotation and flipping portions of the stroke (blue, negative). Streamlines are computed in the body-fixed frame, and as shown are constrained to the plane (60% span). Streamlines are not shown at all times for clarity. Center: Corresponding spanwise vorticity contours (red, counter-clockwise) at the 60% span location. Right: Corresponding spanwise vorticity isosurfaces (red, counter-clockwise).

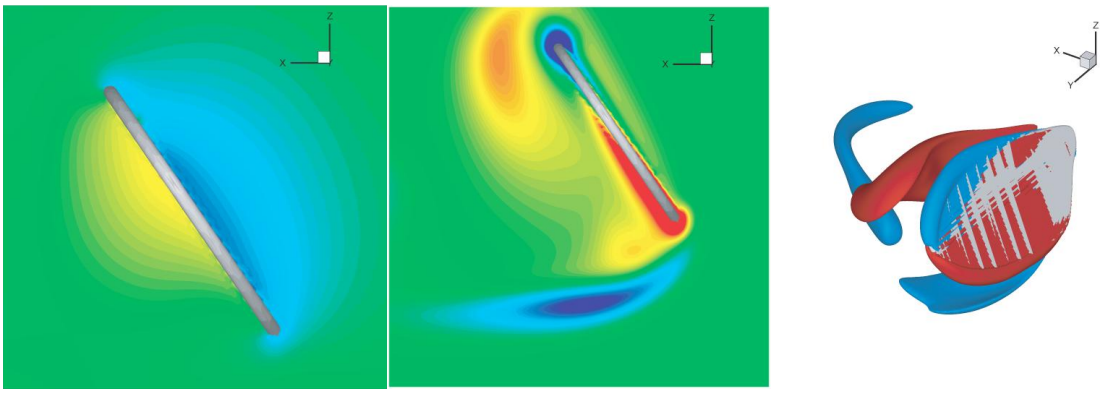

(g) Pressure contours, spanwise vorticity contours, spanwise vorticity isosurfaces at t/T = 50%

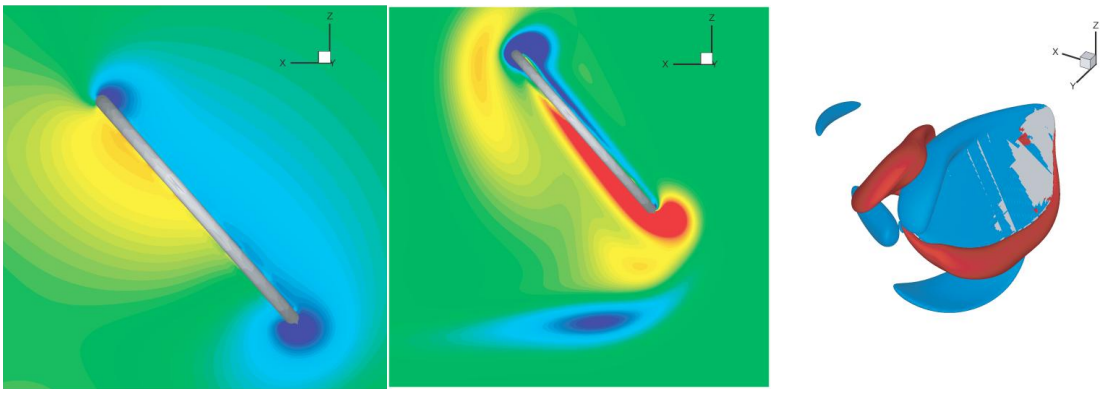

(h) Pressure contours, spanwise vorticity contours, spanwise vorticity isosurfaces at t/T = 53%

Figure 5.6 (continued): Left: Pressure contours ($P - P_\infty$) at various times covering the steady rotation and flipping portions of the stroke (blue, negative). Streamlines are computed in the body-fixed frame, and as shown are constrained to the plane (60% span). Streamlines are not shown at all times for clarity. Center: Corresponding spanwise vorticity contours (red, counter-clockwise) at the 60% span location. Right: Corresponding spanwise vorticity isosurfaces (red, counter-clockwise).

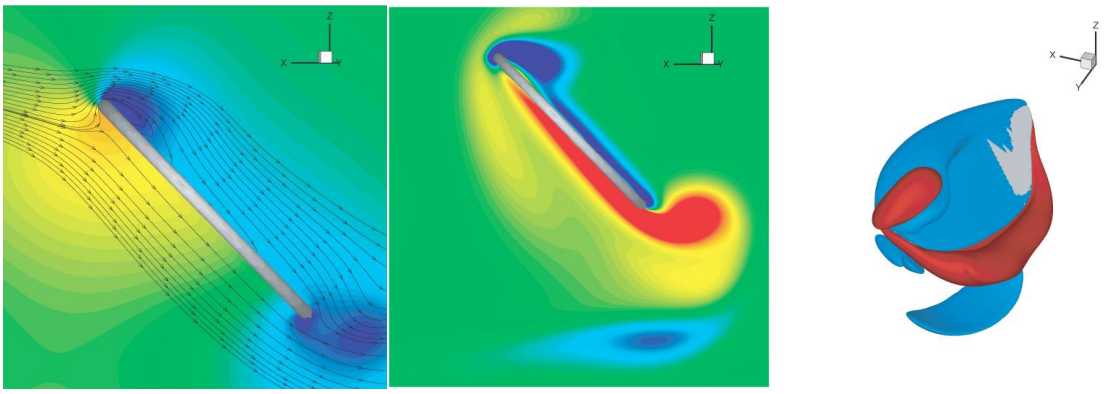

(i) Pressure contours, spanwise vorticity contours, spanwise vorticity isosurfaces at t/T = 55.5%

Figure 5.6 (continued): Left: Pressure contours ($P - P_\infty$) at various times covering the steady rotation and flipping portions of the stroke (blue, negative). Streamlines are computed in the body-fixed frame, and as shown are constrained to the plane (60% span). Streamlines are not shown at all times for clarity. Center: Corresponding spanwise vorticity contours (red, counter-clockwise) at the 60% span location. Right: Corresponding spanwise vorticity isosurfaces (red, counter-clockwise).

Recall in Chapter 4, it was shown that for the impulsively started constant pitch angle rotation, the leading edge separation bubble grows to reach a quasisteady size that varies along the span of the wing. This LEV size (at the 65% span location) was shown to become stable after approximately 70^o of travel from an impulsively started rotation. As seen by the streamlines in Figures 5.6a – c, the LEV in the present unsteady flapping case continues to grow throughout the constant angular velocity portion of its stroke, even though between t/T = 0% – 24.5% (corresponding to Figure 5.6c), the wing has traveled a total of 87.9^o past stroke reversal. Notably however, the present case is dissimilar from the impulsively started case in that the first 29^o of the upstroke includes a significantly more gradual acceleration from zero rotational velocity combined with a downward pitching from $\alpha = 56.3°$ to $\alpha = 45°$.

At t/T = 26%, just after the middle of the upstroke, the wing begins to pitch up for its flip at stroke reversal. This is accompanied by an increase in lift and drag in a dynamic stall-like process that results in a peak lift of 0.6N at t/T = 35.0% and $\alpha = 53.8°$. Note that this dynamic pitching allows a lift greater than what one would expect from the quasisteady result. Figure 5.6d highlights pressure and vorticity in the flowfield at t/T = 34.5%, where $\alpha = 51.6°$, just before the lift peak. The pitching motion causes a reduction in the absolute rotational velocity of the leading edge, and an increase in the absolute rotational velocity of the trailing edge. This results in an expansion of the leading edge vorticity region further into the wake as it begins to shed, and the formation of a region of vorticity at the trailing edge which arises from the strengthening shear layer created by the flow around the lower portions of the wing. Comparing Figures 5.7a and 5.7b, the leading edge peak suction pressure remains relatively stable between t/T=9% and

t/T=34.5%, although the chordwise pressure distribution along the downstream portions of the span become more linear (Figure 5.7b). On the lower surface, the stagnation point begins to move from the leading edge towards the trailing edge and at this particular point in the stroke, the lower surface pressure is nearly constant across the chord. As indicated by the spike in pressure lift and drag (Figure 5.4), it is this combination of upper and lower surface pressure changes that contributes heavily to the peaks in total lift and drag. With the LEV still attached and growing, and no new recirculation regions formed at the wing surface, the shear-related lift and drag continue the trends established during the steady portion of the stroke.

However, the shear-lift increases rapidly after the lift-stall begins to occur near t/T = 35%. This can be explained as the result of a combination of factors. The continued presence and growth in intensity of leading-edge recirculation region on the upper surface increases the near-wall velocities. This coupled with the redirection of the total shear vector due to the flip gives a greater lift contribution from the viscous effects associated with the LEV. Finally, the lower surface begins to play a larger role in the viscous lift generation, as the near wall velocity in the positive lift direction increases along the wing as it pitches towards $\alpha = 90°$ (Figure 5.6e). The drag peak occurs just before the $\alpha = 90°$ point at $\alpha = 86.8°$. Considering the kinematics, it is reasonable to expect that this peak occurs before mid-flip, since at this point the wing has already begun its azimuthal velocity deceleration, which acts to decrease drag. Figures 5.6e and 5.6f capture the wing just before and just after this mid-flip point. The corresponding sectional relative pressure distributions in Figure 5.7b show that between t/T = 34.5% and t/T = 40% the magnitude of the upper surface suction peak rapidly increases from what had been a relatively

constant value around -0.8 up to to -0.93. By t/T = 45% though, this peak dramatically falls to -0.48 just after the mid-flip $\alpha = 90°$ point. Simultaneously, the relative pressure towards the leading edge on the upper surface changes signs and decreases to negative values (i.e. contributes to positive lift). This loss of the strong suction peak on the upper surface is an indication of the weakening and detachment of the LEV (at the 60% span location). The detachment is also apparent in that the initial formation of the LEV for the coming downstroke can be seen as regions of spanwise vorticity of opposite sign to the upstroke LEV forming near the leading edge in Figures 5.6e and 5.6f. Near the trailing edge, a region of spanwise vorticity of the same sign as the upstroke LEV forms and is associated with a small recirculation region that began to develop with the shear vorticity region just after the initiation of the upstroke flip.

Although the wing is still moving in the upstroke direction between t/T = 45% – 50% (moving towards the right between Figures 5.6f – 5.6g), the wing's deceleration, coupled with the induced in-plane flow from previous portions of the upstroke, creates an induced flow that is effectively also oriented in the upstroke direction. This puts the wing at an effective aerodynamic angle of attack of less than 90^o with respect to the oncoming flow. A result of this is the development of the low pressure regions to the right of the wing seen in Figures 5.6f – 5.6g. More significantly, combined with a peak in shear-lift at t/T = 44.0%, these low pressure regions appear to contribute to a rapid rebound of the total lift after a brief, low magnitude interval of negative lift values between t/T = 43.9% – 45.0%. Accompanying the increase in lift is a sizable decrease in drag, leading to a strong drag peak at t/T = 50% of -0.72N. The drag peak for the entire stroke which occurred near

t/T=41.2% is 1.24N, meaning that within a 9% stroke duration, the drag fluctuates approximately 1.96N.

At pronation (t/T = 50%), although the wing continues its counterclockwise flip (as viewed in Figure 5.6g), the instantaneous azimuthal rotational velocity is zero ($\phi(t) = 0$). Note that for the surface pressure distributions at times greater than or equal to t/T = 50%, because the stroke direction has reversed, what was formerly called the "upper surface" for the upstroke becomes the "lower surface" for the downstroke. The spanwise vorticity contours and isosurfaces at this point show a variety of structures in various states of growth and decay. The spanwise vorticity isosurfaces in Figure 5.6g clearly illustrate that the upstroke LEV is definitively separated from the wing. We also see that without the motion of the wing to maintain its size and strength, the detached LEV weakens (Figure 5.6g, vorticity), and in its place a small LEV of the opposite sign grows to form the downstroke LEV. At the trailing edge, the large shear vorticity region has separated from the wing and starts to convect below the stroke plane into the wake. In its place at the trailing edge are two structures, with the predominant one being the translational starting vortex for the coming downstroke. Note that the induced flow from the upstroke has promoted the formation of both the starting vortex and the LEV before the wing has begun to translate for the downstroke. The second structure is the vortical region associated with the small recirculation region formed during the upstroke flip. It does not appear to be enveloped into the starting vortex, but instead remains slightly below it and dissipates accordingly without its shear-layer energy source. At this spanwise station, the shear layer vorticity region formed near the trailing edge on the upstroke remains intact, weakening only slightly as it is pushed under the wing as the

wing moves back above it. The separated upstroke LEV along the inboard portions of the wing dissipates rapidly as the wing directly reencounters it on the downstroke, however the outboard portions remain intact as they are pushed up and over the wing and out towards the wingtip (Figure 5.6g – i). A more detailed description of the evolution and dissipation of the separated LEV will be given in the wake structure section.

As the wing begins the translation at the beginning of the downstroke (Figure 5.6h – i), the lift and drag both reach local maxima at t/T = 54.0%. A major part of these peaks are again attributed to corresponding pressure force peaks (Figure 5.4), and a portion of those forces may be attributed to the low pressure regions formed by the starting vortex and the developing LEV (Figure 5.6i, shown just before force peaks). The negative peak of the viscous lift and the relatively high values of positive viscous drag indicate that no significant recirculation region has developed on the wing surface by t/T = 55.5% to counteract the attached flow shear forces. As the low pressure region associated with the trailing edge starting vortex moves downstream, the pressure-related and total lift and drag forces begin to decrease. This can be seen in the sectional relative pressure distributions as an increase in the upper surface pressure along the aft portion of the wing. Note that the suction peaks approach their steady rotation values fairly quickly, with the upper surface suction peak at -0.7 by 5.5% of stroke after pronation. As the total lift and drag approach their steady rotation mean values, the remainder of the downstroke becomes qualitatively similar to the upstroke. Minor variations in the computed values will be discussed in the next section.

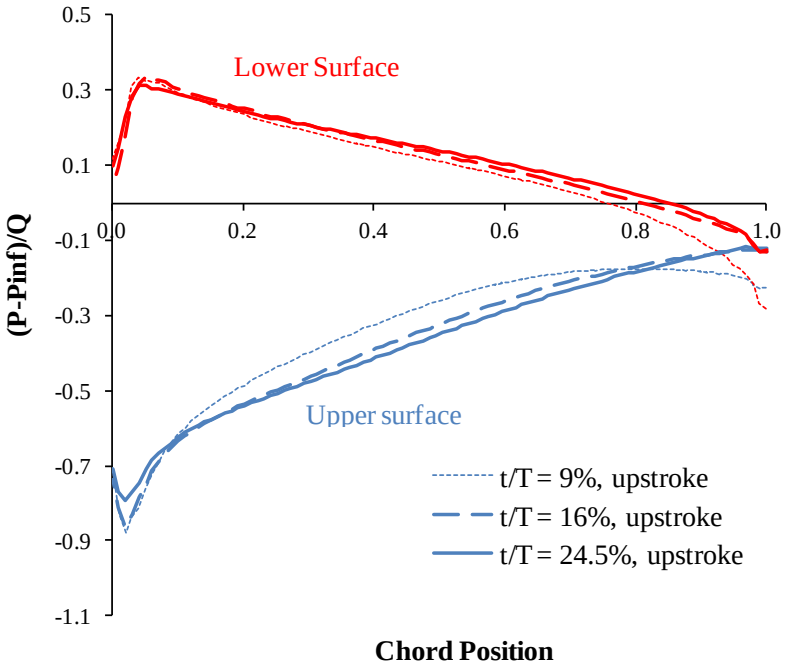

(a)

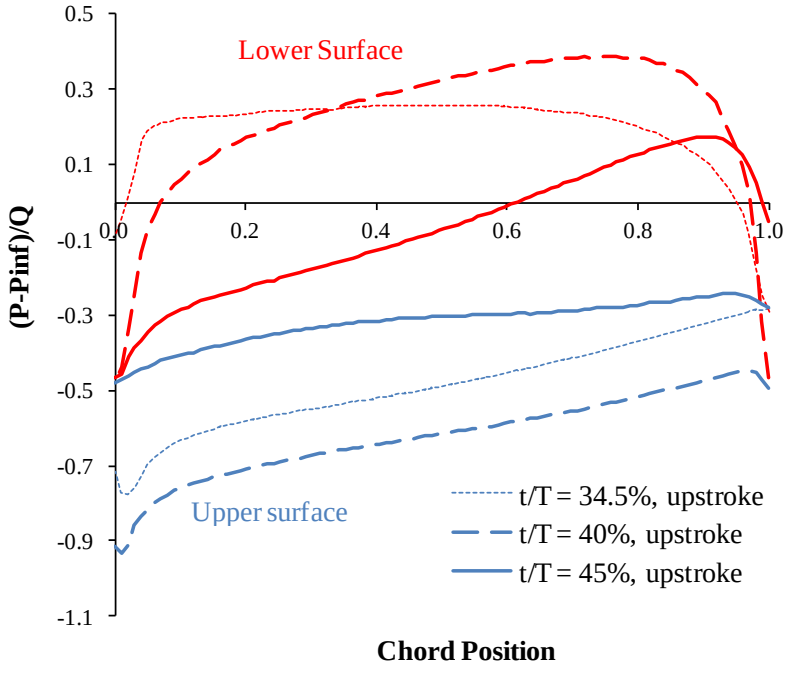

(b)

Figure 5.7: Sectional relative pressure distributions at 60% span at various stroke times, nondimensionalized by freestream dynamic pressure based on mean wingtip velocity.

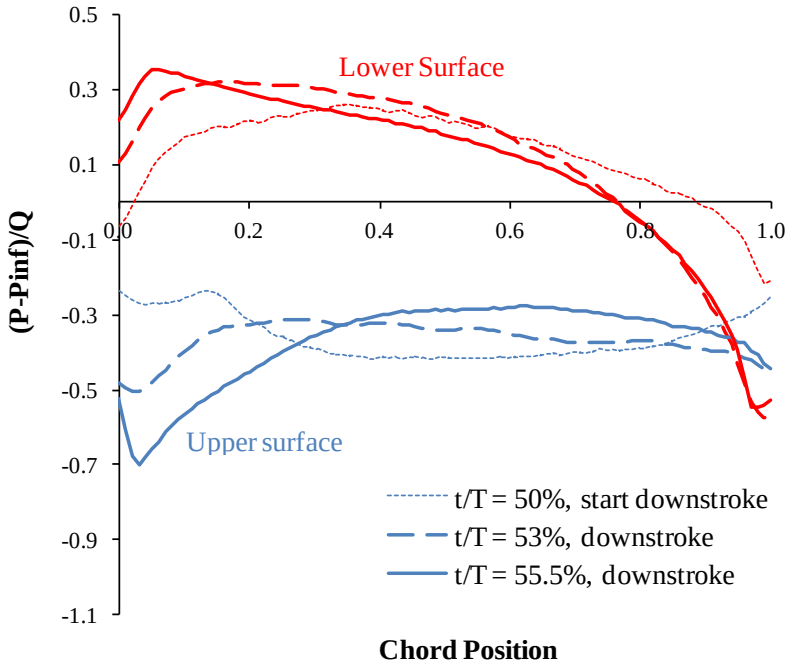

(c)

Figure 5.7 (continued): Sectional relative pressure distributions at 60% span at various stroke times, nondimensionalized by freestream dynamic pressure based on mean wingtip velocity.

5.1.2.2 Comparison with Experiment

The primary discrepancies between the simulation parameters of the experiment and the baseline computations are the thicker wing used for the computational model, the modified wing geometry at the root, and small discrepancies in the prescribed kinematics that are largest near stroke reversal. Nevertheless, although the general trends are captured well, the computed instantaneous force time histories at the fourth stroke (Figure 5.8) show some differences with the experiment, particularly during stroke reversal. Mean values for experimental and computational lift are 0.41N and 0.47N, respectively, which represents a 15% computational overprediction. This discrepancy is mostly fed by the underprediction of the lift peak magnitudes, which are, in some cases, 19% lower than the experiment. Because the stroke reversal drag peaks are captured more accurately, the mean drag is much closer to experiment, with the computational value of 0.63N being only 3% greater than the experimental mean of 0.61N. It is also of note that the experiment seems to exhibit an asymmetry in the both the lift and drag results for the up and downstroke, even during the fourth stroke when the CFD shows essentially periodic half stroke force time histories.

As noted, during the steady rotation phases of the upstroke and downstroke (t/T = 10% – 26% and t/T = 60% – 76%), a qualitative comparison may be made with the previous quasisteady rotating wing results at $Re = 120$. Recall Figure 4.9 which shows the wing in an impulsively started steady rotation at $\alpha = 30°$ and $\alpha = 50°$ with contours of outboard spanwise flow. For both angles of attack, note the concentration of radial flow towards the trailing edge that peaks at 50% of mean tip velocity. It is seen that for the similar conditions of the present flapping case, a comparable concentration of

spanwise flow with a peak value approaching 49% of the tip velocity exists near the trailing edge during the steady rotation phase.

For this steady portion of the stroke, the CFD overpredicts both the mean lift and drag values, where the experimental mean lift and drag are 0.45N and 0.48N, respectively. The computational mean lift and drag during this same period are 0.52N and 0.59N, respectively. Therefore the discrepancy appears to be related, at least in part, to some steady effect (Figure 5.8). Noting that the wing is operating at a geometric $\alpha = 45°$ during these phases of the stroke, we might expect that the lift and drag should be fairly close in value. Although this is essentially the case for both the computations and the experiment, relative to the experiment, the difference between the drag and the lift is greater in the computations. This supports the idea that during the steady rotational portion of the stroke, the computations are operating at a different effective angle of attack than the experiments, the most likely cause of which is a difference in the strength of the induced flow through the stroke plane. From Figure 5.6a – c, the inclination of the streamlines upstream of the wing highlights that the result of this induced flow is an effective reduction in the aerodynamic angle of attack. In general, the result of this is a reduction in both lift and drag [91], thus if this mechanism is to be held accountable for the differences in forces, the induced inflow resulting from previous strokes must be less significant in the CFD than in experiment. While Birch and Dickinson [17] report and attempt to quantify this effective change in angle of attack, it is difficult to make direct comparisons with the present computational results. We can however note that a potential cause of any variation of inflow may be directly linked to the modified wing root geometry in the computations.

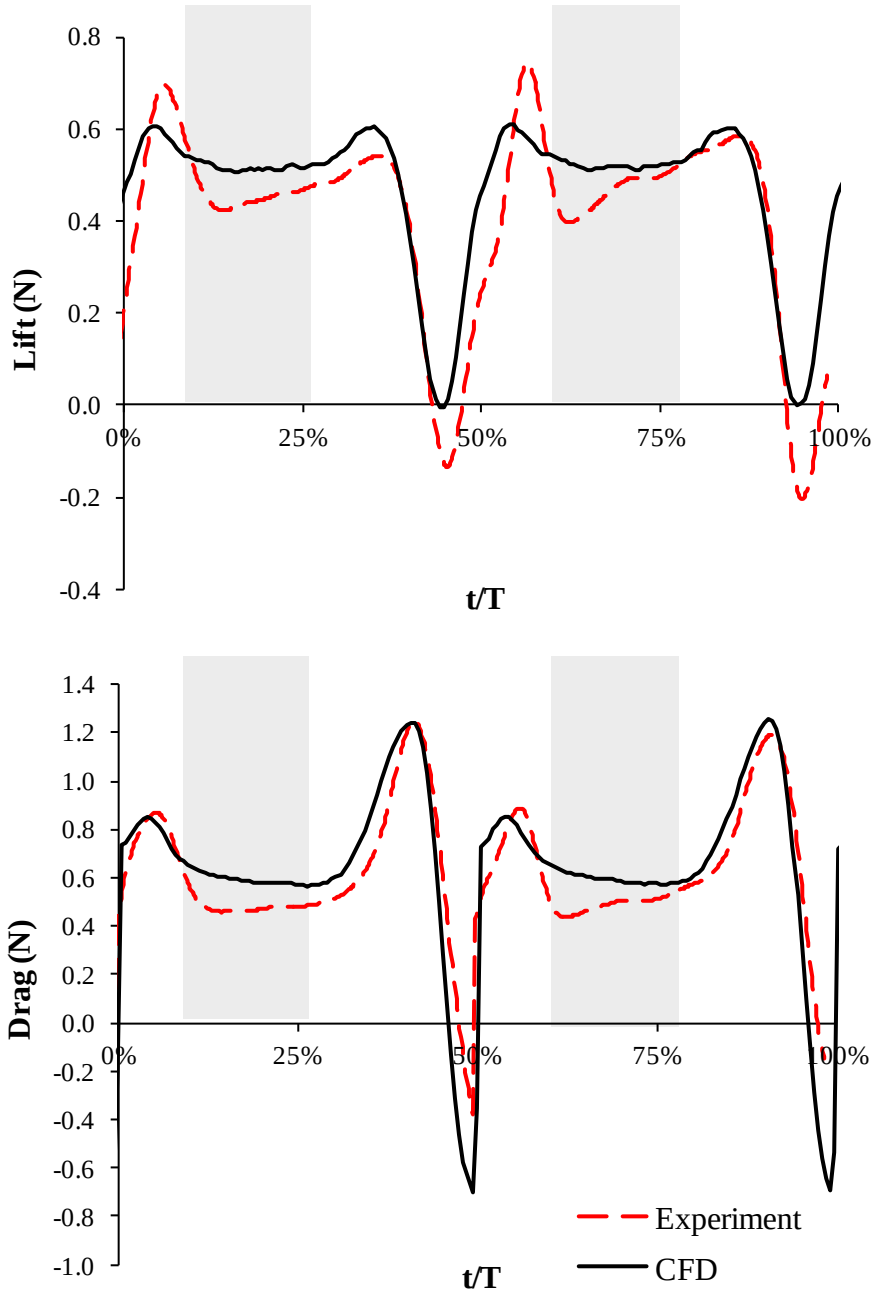

Figure 5.8: Experimental and computational force time histories. Shaded regions indicate the phases of travel during which the rotational angular velocity is constant and the pitching velocity is zero.

Figure 5.9 shows contours of vorticity normal to the plane y = 0 (see Figure 5.10 for orientation of coordinate system). The pitching axis is contained within this vertical plane at mid-stroke. The axes values have been normalized to the stroke radius and the wingtip is facing towards the right. The streamlines are computed in the fixed inertial frame (including corrections for the pitching velocity where appropriate). Just after the wing passes through this plane (Fig 5.9a, t/T = 32%), the counter-rotating root and tip vortices begin to convect downwards away from the stroke plane. While the tip vortex maintains a relatively vertical convection path, the root vortex moves steadily outboard such that at increasing wake ages, the interaction of the two vortices produces a fluid jet that is oriented downwards, away from the stroke plane. The increasing strength of this jet with time is indicated by the contraction of the 2D streamlines between the vortex pair in Figs 5.9b – d. Thus, in addition to any inflow that may result from a momentum analysis of the stroke plane based on the integrated lift, this low aspect-ratio wing effect provides a mechanism for additional inflow near mid-stroke. This additional inflow is dependent on the size, strength and development of the root vortex, and therefore in order to accurately predict the experimental inflow, and ultimately the associated forces during mid-stroke, it is apparent that a better representation of the experimental inboard geometry and possibly of obstructions due to mounting apparatuses may be required. Induced inflow through the rotor plane will be looked at in more detail in Section 5.1.2.3.

The peak in lift accompanying the upwards pitching of the wing near the end of each stroke is overpredicted for the upstroke by 11%, however the overprediction at the corresponding event in the downstroke is only 2.8%. Since the peak in computed lift changes by only 0.5% between the up and downstrokes, this difference is again due to an

asymmetry in the experimentally measured lift values. The computational drag during the upwards pitching phase increases at a rate similar to the experiment, reaching a peak of 1.24N which is in good agreement with experiment during the upstroke, however a slight increase in the computed drag peak combined with a slight decrease in the experimental drag peak during the downstroke results in a more sizable 5.6% overshoot in predicted peak downstroke drag. All significant peaks in both lift and drag occur slightly earlier than in the experiment. Early lift and drag peaks were also observed by Ramamurti and Sandberg [90] in a CFD study of similar kinematics. While a cause for this discrepancy is difficult to pinpoint, a likely contributing factor is the precise definition of the pitching acceleration, whose peak roughly coincides with the pre-stroke reversal lift peak. While this is not a true dynamic stall event, we still should expect that the penetration depth of the increase in lift for the present case is sensitive to pitching acceleration and reduced frequency [85], and as seen in Figure 4.2 the magnitude and gradients of the reduced frequency are largest near the stroke reversals. The peak phase differences may also be related to the aforementioned inflow discrepancy, since a change in aerodynamic angle of attack modifies the dynamic force generation process. We will see in the next section how pitch rate affects these force peaks.

As the wing continues to pitch up, the drag increases until the rotational deceleration begins at t/T = 41% and $\alpha = 79.4°$. This deceleration acts to reduce drag and this effect quickly overpowers the effects of the continued pitching. The result is a sharp decrease in drag beginning at t/T = 41.5%. Continuing to pitch upwards beyond this point, the lift decreases such that at a geometric angle of attack of 90^o at t/T = 43%, the computed and experimental lift values are 0.04N and 0.06N, respectively. These near zero values are

expected considering that only viscous shear forces or differential pressures on the thin leading and trailing edges could cause any lift generation at this instantaneous stroke position. After this point, as mentioned in the previous section, the computed lift almost immediately begins to increase and the drag continues its rapid fall to a peak near -0.72N (58% of its maximum value for the entire stroke). In contrast, the experimental drag continues to decrease to only -30% of its maximum value for the entire stroke. This represents a 40% overprediction of the negative experimental drag peak. The increased lift and reduced drag in the computations both indicate a stronger influence of the in-plane component of induced flow that the low pressure regions above the wing in Figure 5.6f – g were attributed to. Similarly, the overprediction of the rise in lift over the last 5% of the up and downstrokes is consistent with the idea that the computations are seeing less induced inflow normal to the stroke plane than the experiment, and thus are operating at a higher aerodynamic angle of attack, leading to larger lift and drag forces. This idea however is not necessarily supported by the 16% underprediction in the peak lift at the start of the downstroke. Although this lift peak coincides with a negative peak in shear-lift (indicative of an induced inflow through the plane), if the computational inflow is speculated to be weaker than the experiment, one might expect an *overprediction* of this peak as opposed to the underprediction seen. Nevertheless, without a more comprehensive picture of the highly three-dimensional flowfield of the experiment near stroke reversal, we cannot say definitively whether or not other discrepancies in the vortical structures (such as those that may be produced by differences in wing root geometry) contribute to any of the computation's inaccurate predictions during stroke reversal.

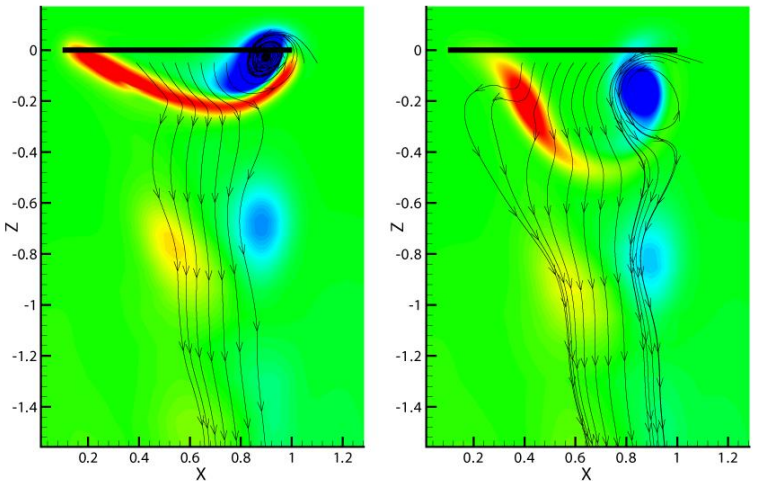

(a) t/T = 32%

(b) t/T = 41%

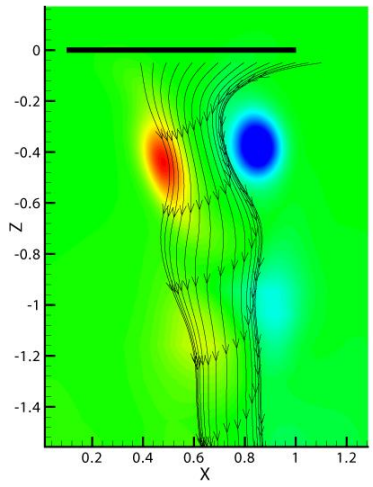

(c) t/T = 56.5%

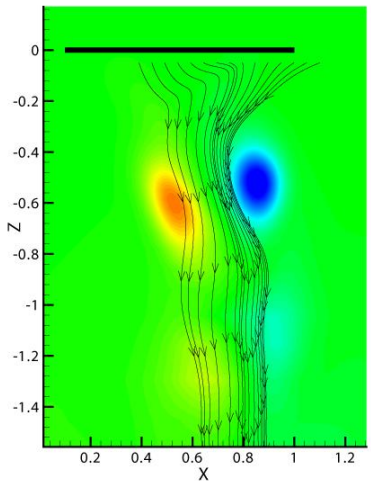

(d) t/T = 67%

Figure 5.9: Spanwise mid-stroke plane with contours of vorticity normal to the plane at various stroke times. 2D streamlines are computed in the fixed inertial frame. The position of the wing's pitch axis at mid-stroke is indicated by the black bar. Distances have been nondimensionalized by wing radius, R, and the wingtip is towards the right of each panel. Note the vortex jet that forms between the root and the tip vortices.

5.1.2.3 Wake Structure

5.1.2.3.1 Mid-stroke root and tip vortex evolution

Figure 5.9 demonstrates that the trailed root and tip vortices, because of their size, strength and close proximity to the stroke plane over the course of a full stroke, can have significant effects on the nearfield flow and thus on the force time histories. To study the wake system, a case using similar parameters as the previous results, but with a more finely resolved mesh below the stroke plane, was run through the sixth full stroke. The difference in mean forces and force peak values between the two cases is less than 1%, with the finer wake mesh case showing slightly larger forces, presumably due to less numerical dissipation of the trailed wake system. These results are used for the visualizations in the rest of this section on wake structure.

Figure 5.10 shows isosurfaces of the second invariant of the velocity gradient tensor, Q, at mid-upstroke, t/T = 25%. Coherent vortex identification using isosurfaces of Q attempts to isolate the vorticity caused by flowfield rotation (the desired vortices) from vorticity caused by shear. Figure 5.11 shows the root and tip vortices every $1/8^{th}$ of a stroke over the course of the fourth/fifth strokes in the same spanwise plane as Figure 5.9, y = 0, using contours of vorticity normal to the plane. The figure progression begins at mid-upstroke (t/T = 25%) when the viewing plane is parallel to the pitching axis of the wing. At this position, the vortex sheet that rolls up to form the root and tip vortices is visible at the stroke plane, still attached to the wing. Finally, Figure 5.12 plots the mid-stroke wake trajectory of the root and tip vortices, calculated by finding the peak Q values in the vortex regions.

Noting that the wake has achieved reasonable periodicity by the sixth stroke, we can use Figure 5.12 to see that at mid-upstroke, the root and tip vortices from the previous downstroke, visible in the center of Figure 5.11a have convected approximately 0.73R and 0.62R below the stroke plane, respectively. As discussed in the previous section, the fluid jet created by this vortex pair induces some additional downwash on the wing. As the wing passes into the page past the viewing plane (Figure 5.11b, t/T = 37.5%) the trailing edge vortex sheet begins to roll up to form the root vortex. As seen in the quasisteady cases, at this low Reynolds number in constant rotation, a concentration of positive (outboard) spanwise velocity is developed just *downstream* of the trailing edge (e.g. Figure 4.9). The strong radial flow, (at its peak, approximately 49% of the tip velocity) provides a mechanism for the rapid convection of the root vortex towards the tip in the time period just after the wing passes through the plane.

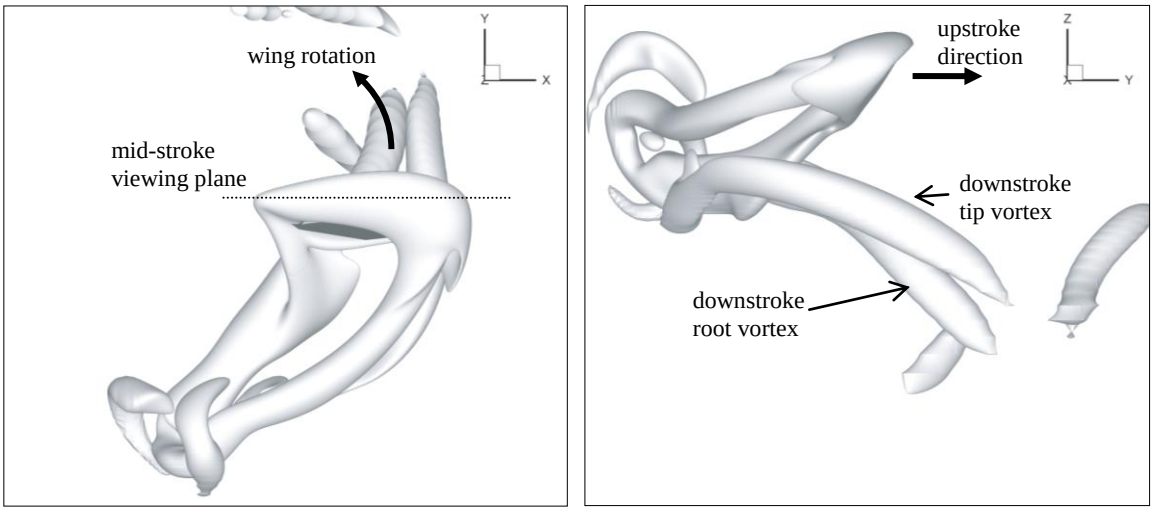

Figure 5.10: Top and stroke-plane views of Q-criterion isosurfaces at mid-upstroke.

Ultimately, a result is the root vortex situated at $0.38R$ at only $0.18R$ below the stroke plane at $t/T = 37.5\%$ (Figure 5.12). Although at this point in the stroke the wing has translated 50^{o} past the mid-stroke plane, the positioning of this vortex, which is most likely also governed in part by the wing root geometry, plays a key role in the amount of downwash created by the vortex jet, as well as the amount of any upwash created in the wing root region of the field due to the inboard portion of the root vortex. The tip vortex, stronger in magnitude than the root vortex, begins a slight inboard contraction immediately after its formation, but maintains a relatively vertical trajectory for a majority of its evolution. By $t/T = 50\%$ (Figure 5.12c), the inboard vortex sheet still has not completed its roll up, as noted by the root vortex's vertical elongation. However, by $t/T = 62.5\%$, as the wing is approaching the shed vortex pair on the downstroke, both vortices have assumed a coherent and fairly circular shape. At mid-downstroke (Figure 5.11e), the vortex positions are essentially the same as their mid-upstroke counterparts in Figure 5.11a, and the remainder of the stroke (Figure 5.11e – h) exhibits this symmetry as well.

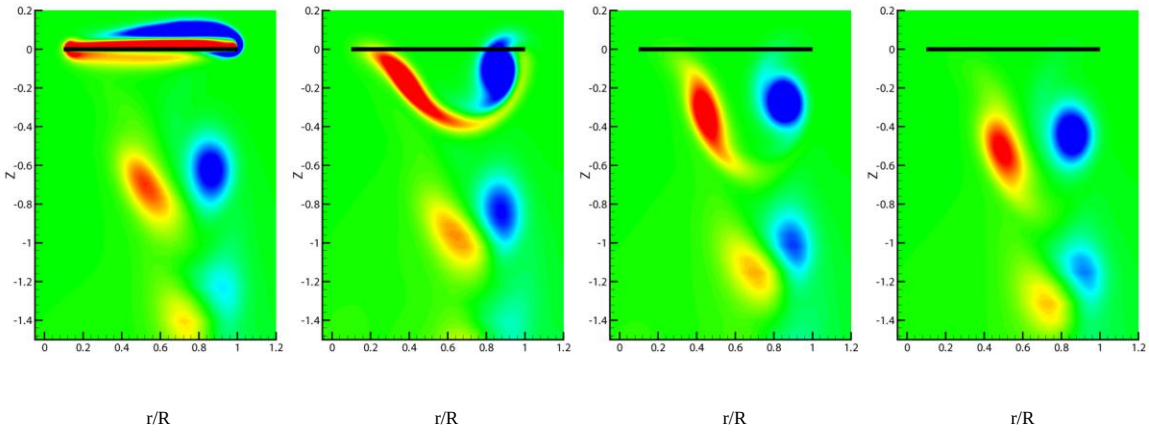

(a) t/T =25% (b) t/T = 37.5% (c) t/T = 50% (d) t/T = 62.5%

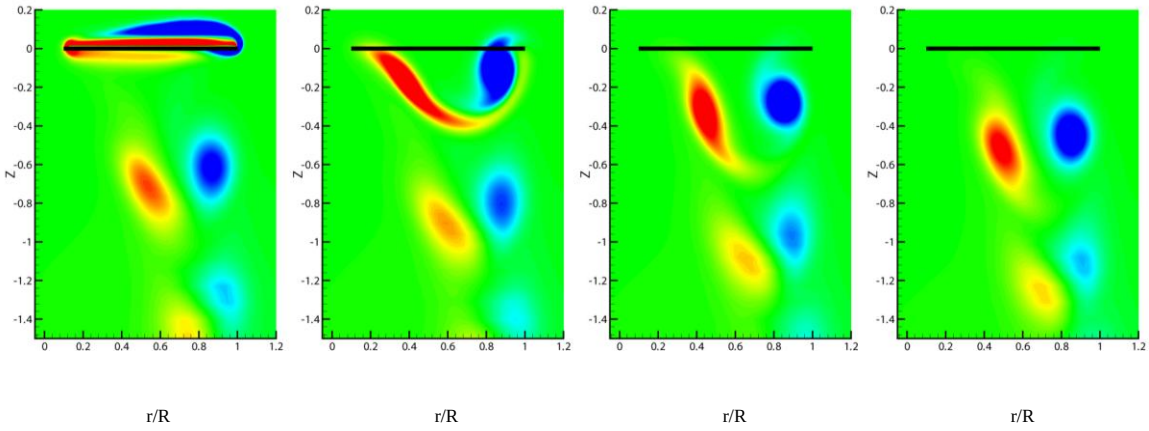

(e) t/T = 75% (f) t/T = 87.5% (g) t/T = 100% (h) t/T = 112.5%

Figure 5.11: Spanwise mid-stroke plane with contours of vorticity normal to the plane at various stroke times. The position of the wing's pitch axis at mid-stroke is indicated by the black bar. The z-coordinate has been nondimensionalized by wing radius, R, and the wingtip is towards the right of each panel.

5.1.2.3.2 Vortical structures at stroke reversal

Figure 5.13 shows isosurfaces of Q for the supination stroke reversal between the fourth and fifth strokes. As seen in previous sections, the dominant structures during the mid-stroke constant velocity rotation are the root, tip and leading edge vortices. These structures are visible in Figure 5.13a, with the addition of a second weaker tip vortex structure originating closer to the trailing edge than the primary tip vortex. Poelma, Dickson, and Dickinson [87] experimentally observed a similar vortex for steady rotation at *Re* = 256, however the strength of their second vortex was on the same order of magnitude as the primary tip vortex. The cause for this difference may be related to the Reynolds number or differences in wingtip geometry. It is interesting to note that Poelma, Dickson and Dickinson reported that the result of the counter-rotating tip vortex pair was a strong spanwise flow of 50 – 75% of the tip velocity. In the present case, at the 60% span location the spanwise flow is 49% of the tip velocity, however this flow does not seem to be associated with a vortex jet between tip vortex structures.

As the wing flip that started at $t/T = 76\%$ continues, by $t/T = 87\%$ the trailing edge vortex generated by the flip begins to form. The rapid acceleration of the trailing edge, with a prescribed peak pitching velocity at $t/T = 92\%$, also causes a growth of the secondary tip vortex and a contraction of the still attached root vortex towards the wingtip (Figure 5.13b – c). The difference in the origination point of the root vortex as it begins to detach is especially clear when comparing the top views of Figures 5.1a and 5.1c. Between $t/T = 95\%$ and $t/T = 100\%$, promoted by the growth of the new upstroke LEV, the downstroke LEV separates by peeling off of the leading edge from tip to root (Figure 5.13d, top view).

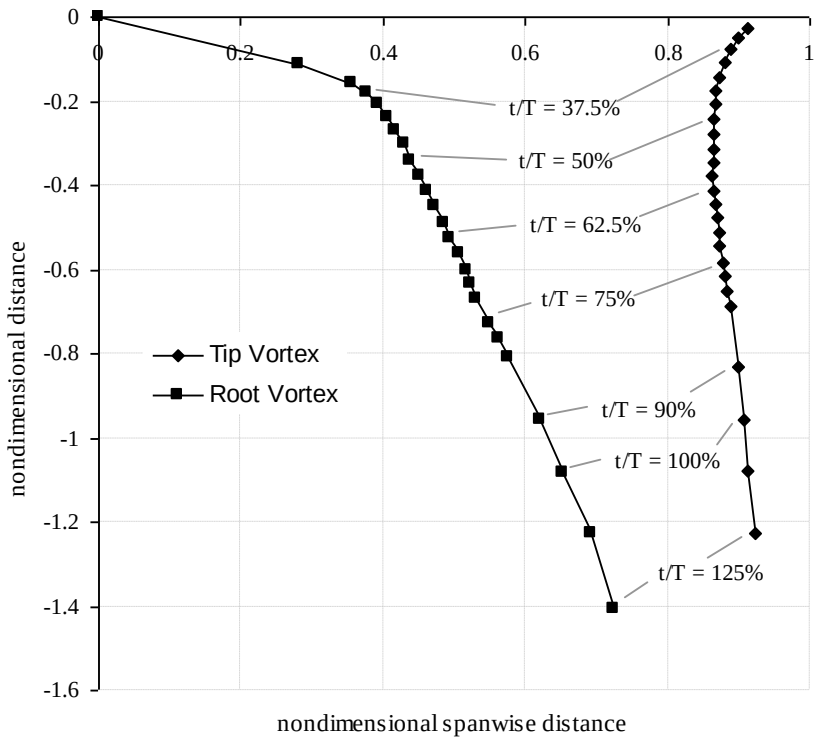

Figure 5.12: Mid-stroke root and tip vortex positions over a single stroke.

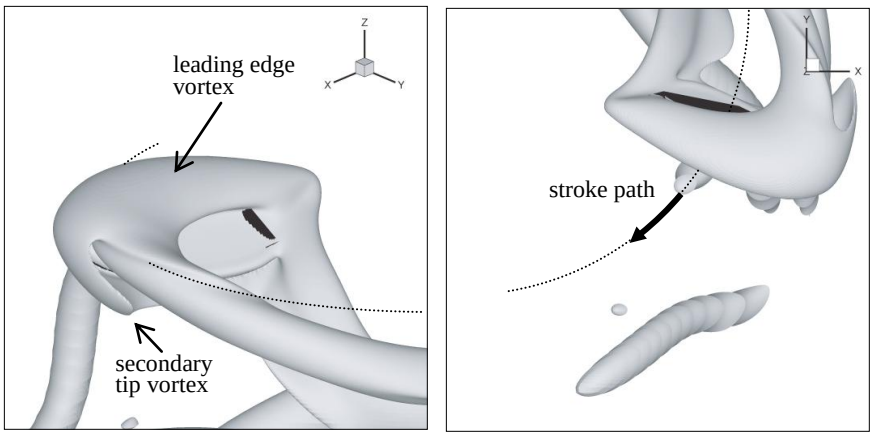

(a) t/T = 80% (downstroke)

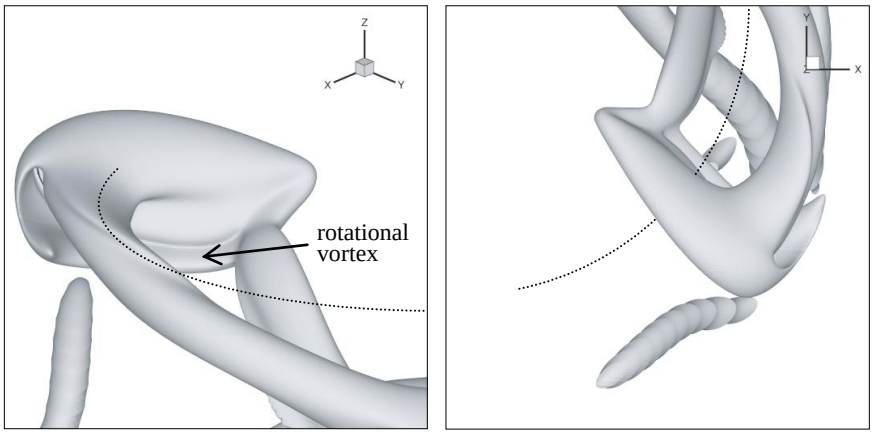

(b) t/T = 87% (downstroke)

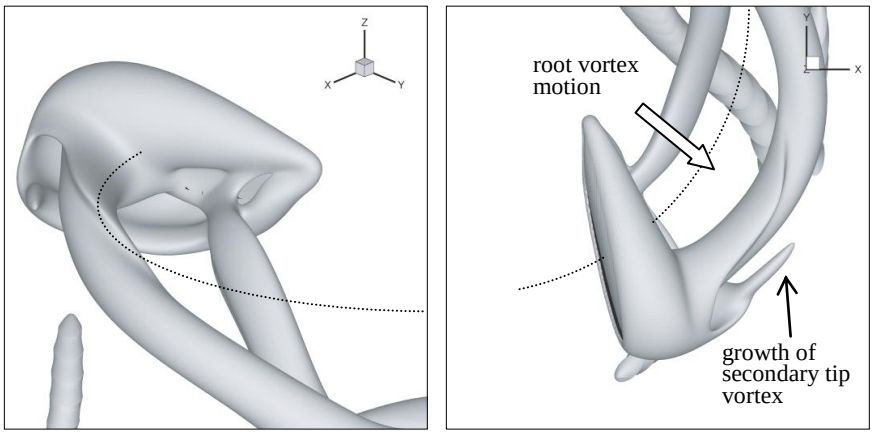

(c) t/T = 95% (downstroke)

Figure 5.13: Oblique (left) and top (right) views of vortical structures present during the stroke reversal at the end of the stroke 4 downstroke. Isosurfaces of Q.

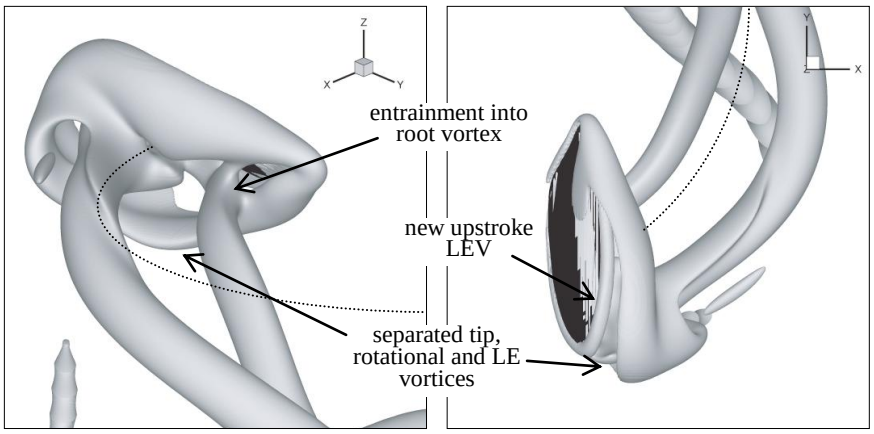

(d) t/T = 100% (supination)

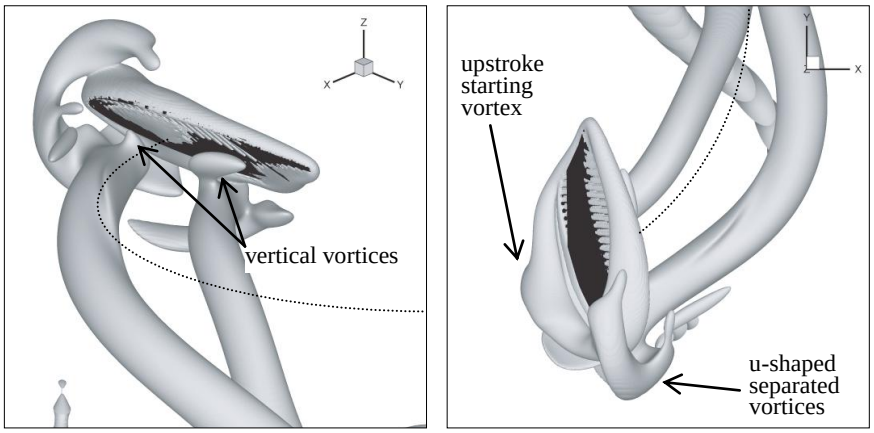

(e) t/T = 105% (upstroke)

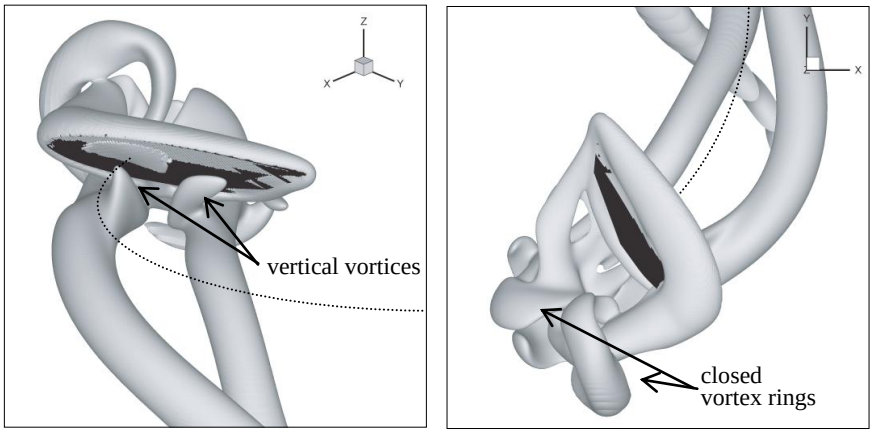

(f) t/T = 110% (upstroke)

Figure 5.13 (continued)

The strongest structures remaining in the wake at supination are the separated root and tip vortices, and a u-shaped open vortex ring consisting of portions of the secondary tip vortex, the separated LEV, and the separated trailing edge vortex formed during the flip (Figure 5.13d). As the wing begins the upstroke, the leading edge collides with this shed vortex ring causing a slight dissipation and outboard convection of the portions of the shed vortex ring associated with the wingtip (Figure 5.13e). Some weaker inboard portions of the shed vortex ring rapidly dissipate, most likely as a result of their interaction with the new attached vortex ring of opposite rotational sense. Interestingly however, the inboard section of the shed downstroke LEV gets pushed *down* along the lower surface of the wing and merges with the trailed root vortex, which itself is being impacted by the trailing edge and pulled *upwards* along the lower surface of the wing. The resulting formation is a vertically oriented vortex that sits at the lower surface of the wing, just inboard of mid-span, whose rotation is roughly in the positive z-direction (Figure 5.13e – f, oblique views). There is also a corresponding, but stronger, counter-rotating vertical vortex that sits just outboard of mid-span, although its origin does not seem to be rooted in the collision with the vortex ring. Instead, this outboard vortex appears to form as the returning trailing edge of the wing grazes the upper portion of the shed tip vortex. Because there is certainly a correlation between the size and position of the tip vortex and the wingtip shape, we would expect that the characteristics or even the existence of this outboard vertical vortex is determined in large part by the outboard planform of the wing.

Although the influence of these vertical vortices on the forces will require further study, a number of factors support the idea that their presence is not insignificant.

Between t/T = 105% and t/T = 110%, the vortex pair strengthens, presumably pulling energy from the shed root and tip vortices of the downstroke. By t/T = 110%, their strength is comparable to the attached developing LEV, and over their duration, the counter-rotation induces a fluid jet oriented in the direction of travel. This vortex pair persists well into the upstroke, and it is not until t/T = 124% (nearly mid-upstroke) that both vortices appear to fully recede into the wake, as the shed tip and root vortices from the previous half stroke become more distanced from the stroke plane (e.g. Figure 5.10).

Remaining at the point of supination are a variety of vortex rings, fairly similar to those observed by Dong et al. [43] in their computational study of a pitching and plunging elliptical wing at *Re* = 200. The upper section of the u-shaped shed vortex ring, visible in Figure 5.13e, wraps downward to join with the starting vortex formed when the wing accelerated after supination. The resulting closed vortex ring is visible in the upper portion of Figure 5.13f (oblique view). Inboard, a smaller vortex ring forms as the shed downstroke root vortex becomes entrained into the upstroke starting vortex. The resulting vortex ring is visible towards the left side of the top view of Figure 5.13f. The combined influence of these rings on the starting vortex was visible in the spanwise vorticity isosurfaces of Figure 5.6a.

5.1.2.3.3 Induced inflow through the stroke plane

Another way to quantify the influence of the wake on the force production is to look at the velocity that it induces normal to the stroke plane. This *induced velocity*, v_i, is a parameter frequently used in rotorcraft analysis where it is normalized by rotor tip speed to give the *induced inflow ratio* $\lambda = v_i/(\Omega R)$. For a rotorcraft, actuator disk momentum theory, combined with small pitch angle assumptions and high L/D values, allows some

useful relations to be derived relating λ to efficiency and airloads, particularly at the hover condition. However, because the unsteady flapping cases involve unsteady wing motion, high angles of attack, predominately separated flow, irregular wing planforms and a large influence of viscosity on the forces, it is not as convenient to derive these relations. Nevertheless, a map of the time-averaged inflow distribution normal to the stroke plane, as given in Figure 5.14, gives some insight into which portions of the stroke are most affected by the induced flow from previous strokes. Inflow velocity is normalized by average tip velocity. Figure 5.14 also plots the inflow at mid-stroke as a function of radial position. Because of the immersed boundary method, it should be noted that in the stroke plane itself ($z = 0$), points inside of the immersed wing are included in the averaging, and thus the net effect is to artificially attenuate the averaged inflow. This effect should be minimal, however.

At mid-stroke in the stroke plane itself, Figure 5.14b shows a roughly linear increase in inflow magnitude up to a peak of 0.26 at r/R=69% . Effective angle of attack can be approximated as

$$\alpha_{eff} = \alpha_{geom} - \tan^{-1}\left(\frac{v_i}{\omega(t)r}\right) \tag{5.6}$$

Therefore, at the $r/R = 69\%$ station at mid-stroke $\alpha_{geom} = 45°$, the wing is effectively operating at approximately $\alpha_{eff} = 27.1°$. While the induced inflow reduces linearly towards zero at the root, the local velocity $\omega(t)r$ also reduces linearly with r, thus the significant induced angle of attack change is nearly constant for the inboard 69% of the wing, before sharply decreasing outboard. Furthermore, this induced angle of attack change persists for the entirety of the 'steady' rotation phase of the stroke.

Below the stroke plane, as the counter-rotating root and tip vortices shed into the wake, they form a concentrated velocity jet between them that peaks at $\lambda = 0.49$ only 0.42 radii below the stroke plane. This is the same vortex pair seen in Figure 5.11, and the radially outward convection discussed previously is seen in Figure 5.14 as the mid-stroke peak in axial flow moving to $r/R = 80\%$ by 1.67 radii (or $4\bar{c}$) below the stroke plane.

The highest inflow velocities are initially at mid-stroke, however moving axially below the stroke plane, the highest inflow velocities shift towards the stroke endpoints. The cause for this can be most clearly seen in the stroke plane view of Figure 5.10. Note that the primary root and tip vortex pair convect more rapidly downwards than the vortices closer to stroke reversal points. This is the result of the reduction in wing rotational velocity surrounding the endpoints, and since the primary driver of the inflow is this rotational motion, the stroke reversal vortical structures convect away from the stroke plane more slowly.

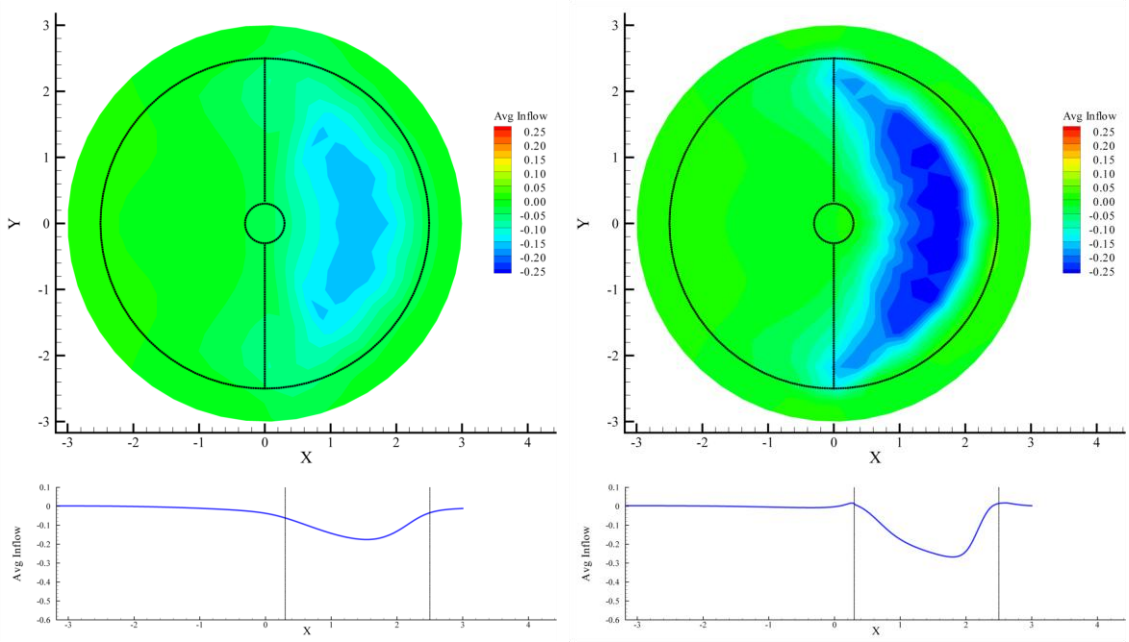

(a) z =0.20R (b) z = 0.0R, stroke plane

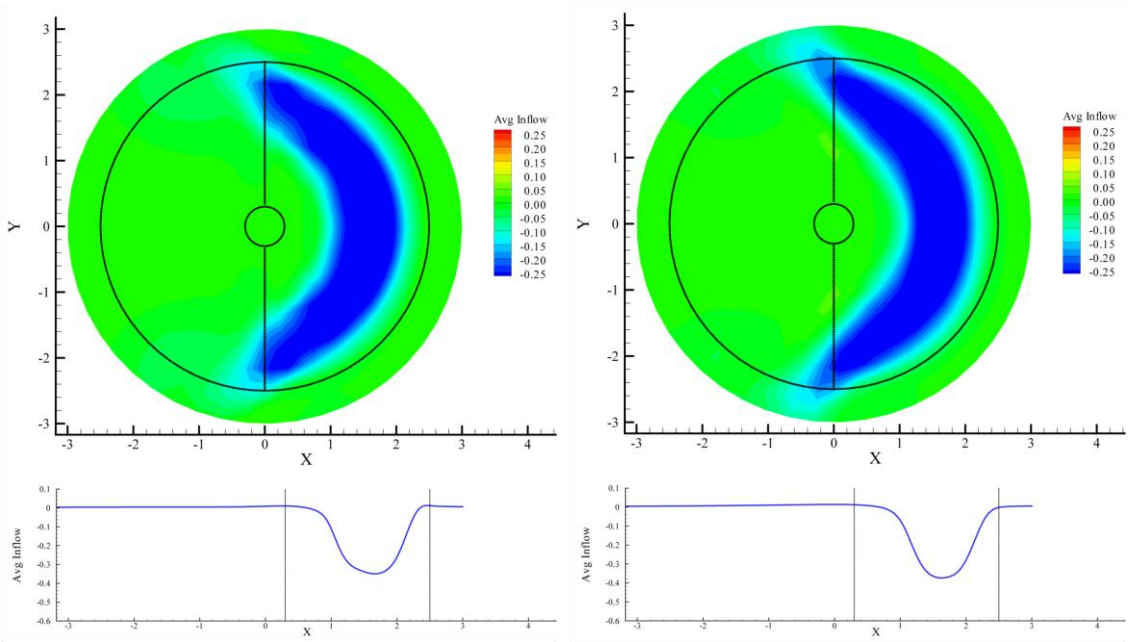

(c) z = -0.25R (d) z = -0.42R

Figure 5.14: Contours of time-averaged inflow ratio over a combined up/downstroke at planes parallel to the stroke plane. Circles on contour plots indicate root and tip path radii. Below each contour plot is the spanwise inflow profile at mid-stroke ($y = 0$).

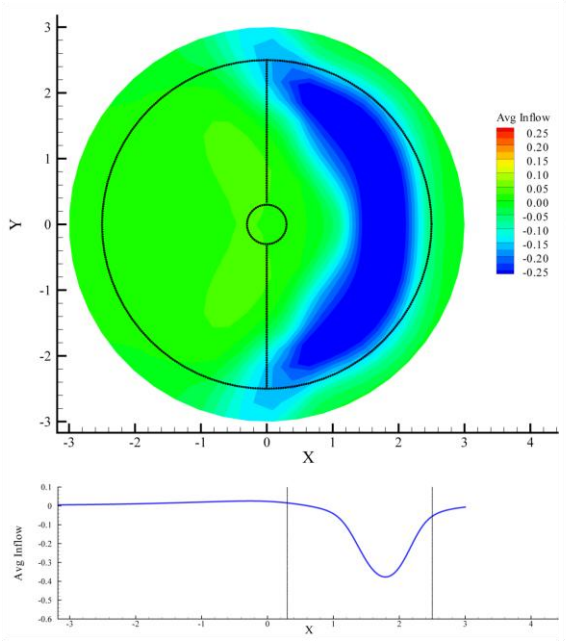

(e) z = -0.83R

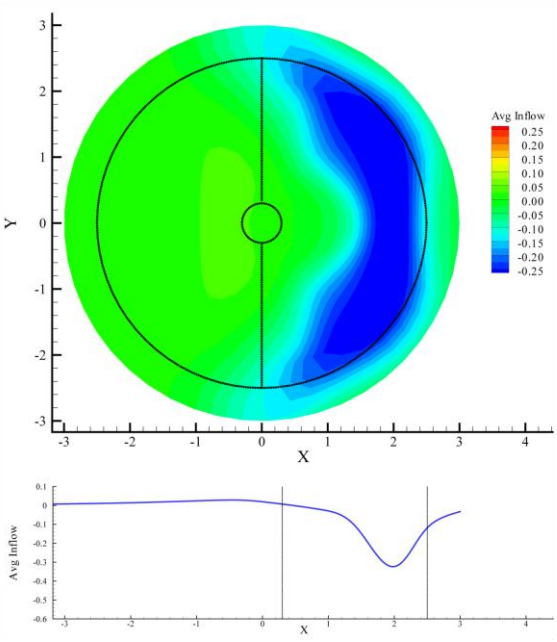

(f) z = -1.25R

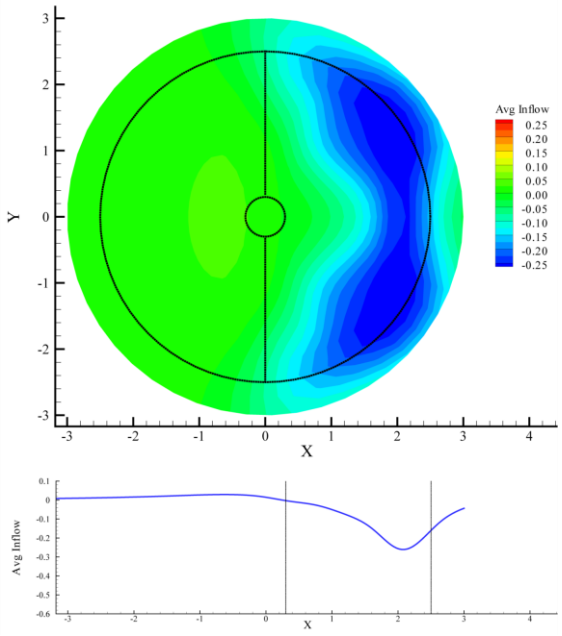

(g) z = -1.67R

Figure 5.14 (continued)

5.1.2.4 Power

Figure 5.15 plots the aerodynamic power required for the baseline flapping case during the fourth stroke, decomposed into viscous and pressure components. The mean power for a full stroke is 0.11W. With the mean lift for this case at 0.47N, the effective mean power loading for this case is $PL = 4.27\ N/W$ or $PL = 716\ lb/hp$. It should be stressed that this is based purely on aerodynamic loads, and a physical system moving a finite mass, mechanical or biological, would incur inertial power costs, in addition to the aerodynamic ones. Experimental literature suggests a range of ratios between the inertial and aerodynamic forces for insect wings and MAVs [5], [12]. Inertial forces have been reported as being nearly an order of magnitude greater than aerodynamic forces for $Re = O(10^3)$ insects, to being nearly the same magnitude for $Re = O(10^4)$ flapping mechanisms. Therefore we can assume that the inertial force contribution would likely be of some significance, and would reduce this effective power loading.

The power time history shows that the viscous profile power required remains relatively small in comparison with the pressure losses throughout the entire stroke. Even the viscous power peaks surrounding stroke reversal do not grow beyond their mid-stroke "quasisteady" values. Total power required itself closely resembles the drag curve, as expected, and the mean power for the full stroke is 0.11 W.

As the wing pitches down and accelerates in the rotational direction at the start of the upstroke at t/T=0%, there is a minor peak in power required. The induced velocities in the stroke plane from the shed wake vortices discussed previously are also a contributing factor. So while the "wake-capture" effect provides a means to generate lift, it comes at the cost of an increase in aerodynamic power required at stroke reversal. This local peak

is followed by the steady rotation constant pitch angle portion of the stroke where power remains essentially constant and near its mean value. As the wing begins to pitch up towards a pitch angle of 90°, the power required sharply increases to a peak of 0.26W, which is 2.5x the mean value. Power then immediately reduces as the wing rotationally decelerates and begins to pitch past 90° for the start of the downstroke at t/T=50%. Briefly just before stroke reversal, power is *extracted* from the flow as the wing's rotation has nearly stopped and the induced in-plane flow creates the upstream low pressure region discussed earlier and seen in Figure 5.6g. As the wing begins the downstroke, the power increases as the starting vortex is formed, and the power requirement proceeds as with the upstroke.

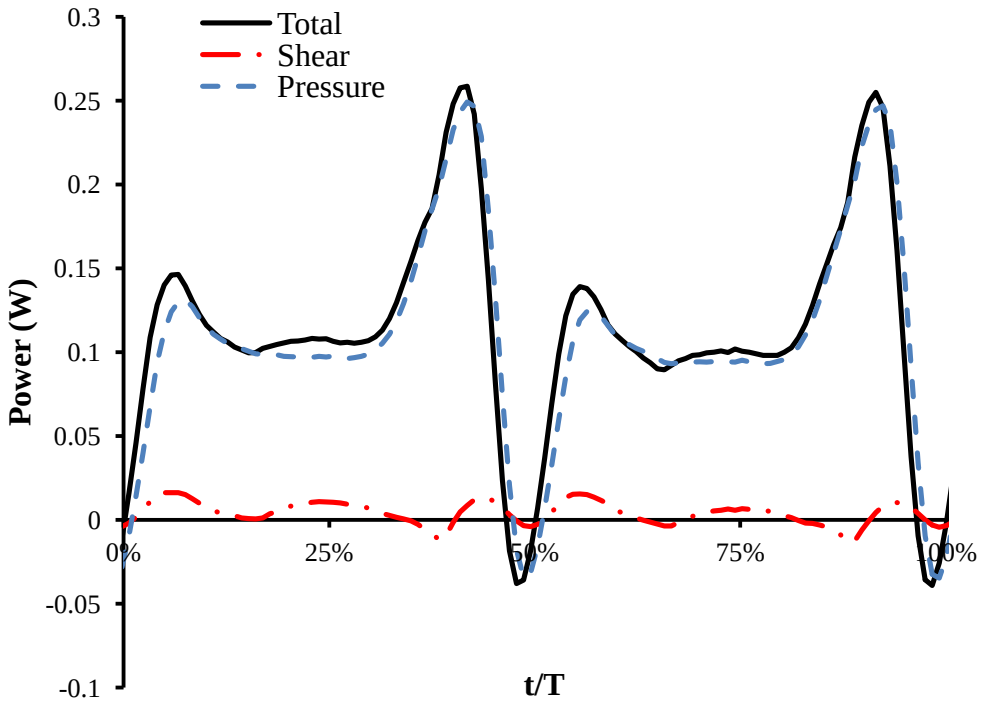

Figure 5.15: Power time history of the baseline flapping case decomposed into pressure (normal) and viscous (tangential) components.

5.2 Modified Pitch Angle Cases

At this point we have built a detailed description of the baseline flapping stroke, its wake, and the resulting forces. However, it is difficult to draw conclusions about the mechanisms underlying the baseline flowfield and its resulting forces without comparison to other kinematics. It has already been shown how well the quasisteady simulation predicts the mid-stroke lift, drag and power, as well as how reasonably close the quasisteady value is for the stroke averaged force and power quantities. Therefore, in order to further explore this relationship and determine what departures there are (if any) from the other kinematics, the mid-stroke flapping angle is chosen as the free parameter of interest.

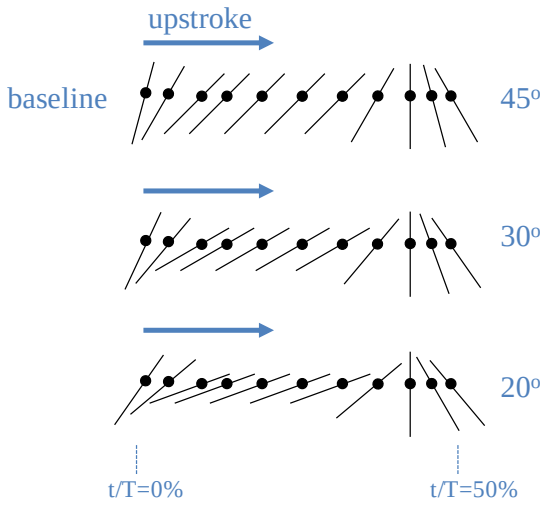

Figure 5.16: Stroke diagrams for the baseline and modified advanced-flip flapping cases.

The geometric, kinematic, and computational parameters of the modified flapping stroke remain the same as described by Equations (5.1) – (5.5) and in Figure 5.3, with the exception that the mid-stroke angle is modified to be $\alpha_{mid} = 20°$ and $30°$ (Figure 5.16). The flip at stroke reversal still takes place in advance of the supination and pronation

points, in the same amount of time as for the baseline case, and the mean tip velocity and Reynolds number remain the same.

5.2.1 Forces

Figure 5.17 plots the lift and drag force time histories over one stroke for the 20°, 30°, and baseline 45° flapping cases. As a general expected trend, the lift and drag tend to decrease with mid-stroke pitch angle. However, if the forces are parameterized by their peak value, the mean value over a single stroke, and the mean value over the constant velocity rotational portion of an up/down stroke, as in Figures 5.18 and 5.19, it is seen that the force peaks actually increase with decreasing mid-stroke pitch angle. This is primarily attributed to the increased pitching acceleration required to pitch the wing through the greater total pitching angle with decreasing mid-stroke angle. While peak rotational velocity is the same for all cases, peak pitching rate for the 20° and 30° cases are $2.42 rad/s$ and $2.07 rad/s$, respectively (maximum reduced frequency metrics, as described in Section 4.2 remain well within incompressible limits), which represents a 56% and a 33% increase over the baseline case.

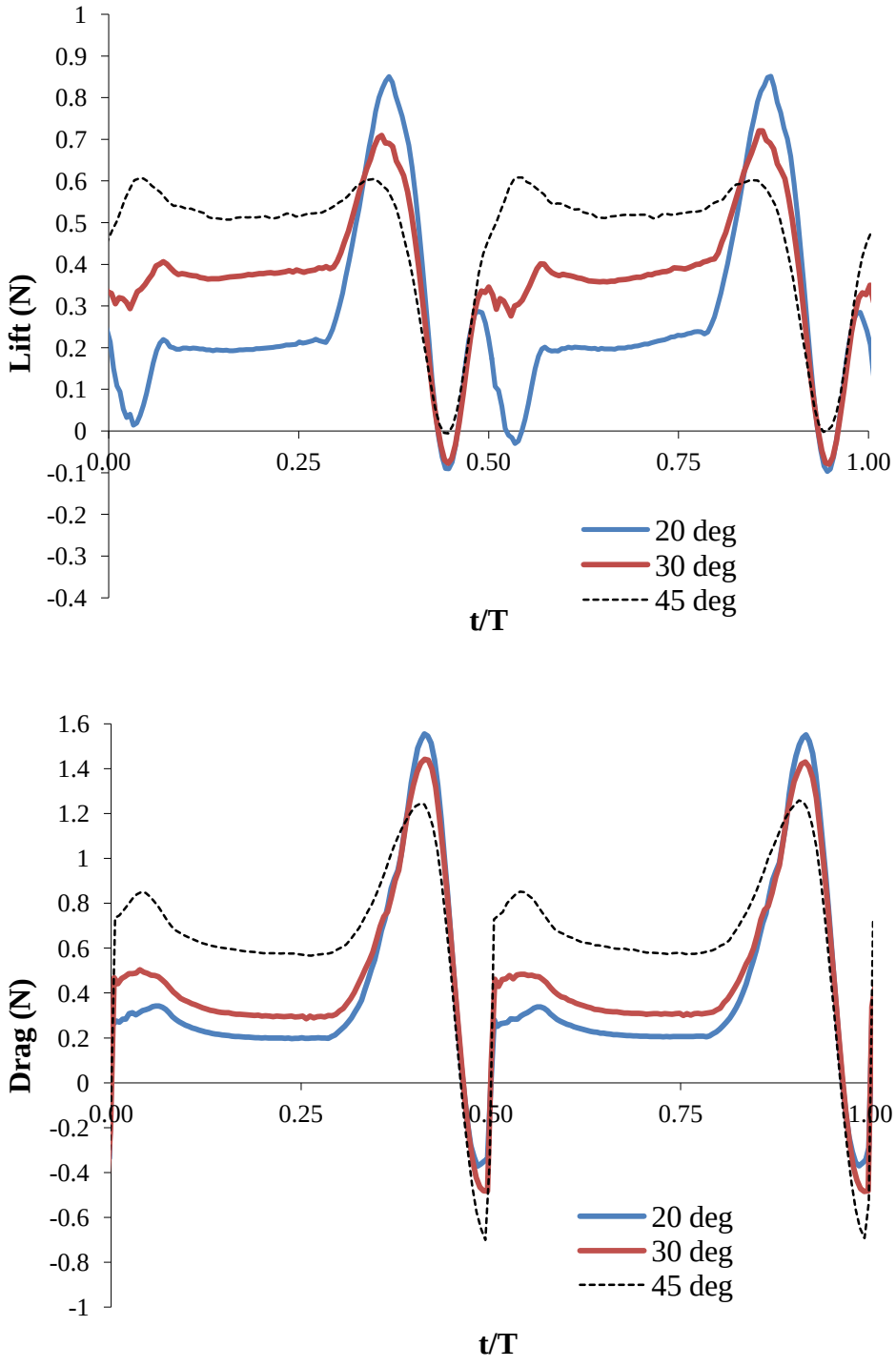

Figure 5.17: Lift and drag time histories for 20°, 30°, and 45° mid-stroke flapping cases.

Compared with the quasisteady results, the mean lift of the flapping cases is consistently about 10% lower (Figure 5.18). While the mean lift for the steady rotation portion of the stroke is close in value with the quasisteady result at 45°, for the 30° and 20° cases, the mean lift gets progressively lower than the quasisteady predictions. Differences in forces may be attributed primarily to differences in the downwash for the unsteady cases. More specifically, the progressively increasing departure from quasisteady results with lower mid-stroke pitch angles suggests an increased influence of downwash with reducing pitch angle (see section 5.2.2). This is in contrast to the drag, where the steady rotation portion of the drag is predicted quite well by the quasisteady simulations for all simulated mid-stroke pitch angles; drag is not as affected by the differences in the downwash for the flapping cases. The mean drag over the entire stroke is consistently higher than the quasisteady value (Figure 5.19), and the reduction in slope of the mean drag curve compared with the quasisteady curve shows a slightly reduced sensitivity to mid-stroke pitch angle. This is what we would expect, noting that in the quasisteady case, drag was most sensitive to pitch angle near 45°, and less so as we moved towards $\alpha = 0°$. For both the lift and drag plots, the large effect of wake capture is readily apparent by noting the gaps between the peak and the mean computed forces in Figure 5.18 and Figure 5.19.

It is interesting to note that while the drag time histories for all cases appear to have qualitatively similar trends in peaks and steady values, the lift time histories for both the 20° and 30° cases are different from each other, and also different from the 45° degree case surrounding stroke reversal. For the 45° case, at $t/T = 43\%$ lift drops to essentially zero as the wing pitches through $\alpha_{geom} = 90°$. The similar lift minima for the 20° and

30° cases drops below zero to -0.09N and -0.08N, respectively, before beginning the lift recovery associated with wake capture. For the 45° degree case, the lift then *monotonically* increases to a peak of 0.61N. However for the lower pitch angle cases, just before the stroke reversal, this wake capture increase in lift stalls out, and both the 20° and 30° cases begin to lose lift. At supination, the 20° case's lift falls to -0.03N before it slowly recovers to towards the mid-stroke mean value. The 30° case builds small local lift peaks but does not climb significantly above the mid-stroke mean value.

This collapse of the lift-peak post-stroke reversal highlights a difference in interaction with the shed wake for the lower angle of attack cases. In Figures 5.20 and 5.21, two key points of departure in lift behavior are shown along with the instantaneous Q-criterion isosurfaces for each case. Figure 5.20 plots these isosurfaces at the pre-supination inflection point of the lift curve, just before 20° and 30° cases begin to lose lift. Figure 5.21 shows these isosurfaces just after supination, where lift is near its peak value for the $\alpha = 45°$ case, but is at a local *minima* for the 20° and 30° cases.

Immediately apparent at both points in the stroke is the reduction in strength of the root and tip vortices with the reduction in mid-stroke pitch angle. As previously noted, the root vortex on the 45° case is the same order of magnitude in terms of strength as the tip vortex, and it persists generating a velocity jet between them. As the root vortex weakens in relative strength, this velocity jet also decreases in magnitude, thus some of the additional inflow is reduced for the lower pitch angle cases.

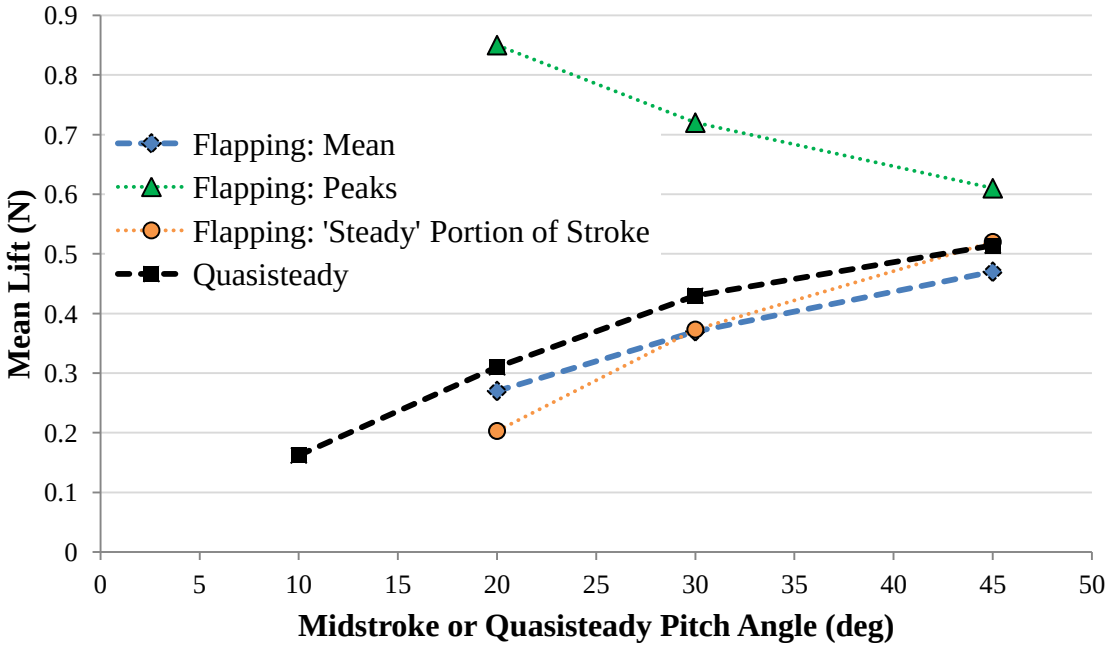

Figure 5.18: Stroke-averaged lift for the unsteady cases compared with quasisteady lift, average lift over the steady portions of the stroke, and instantaneous positive peak values.

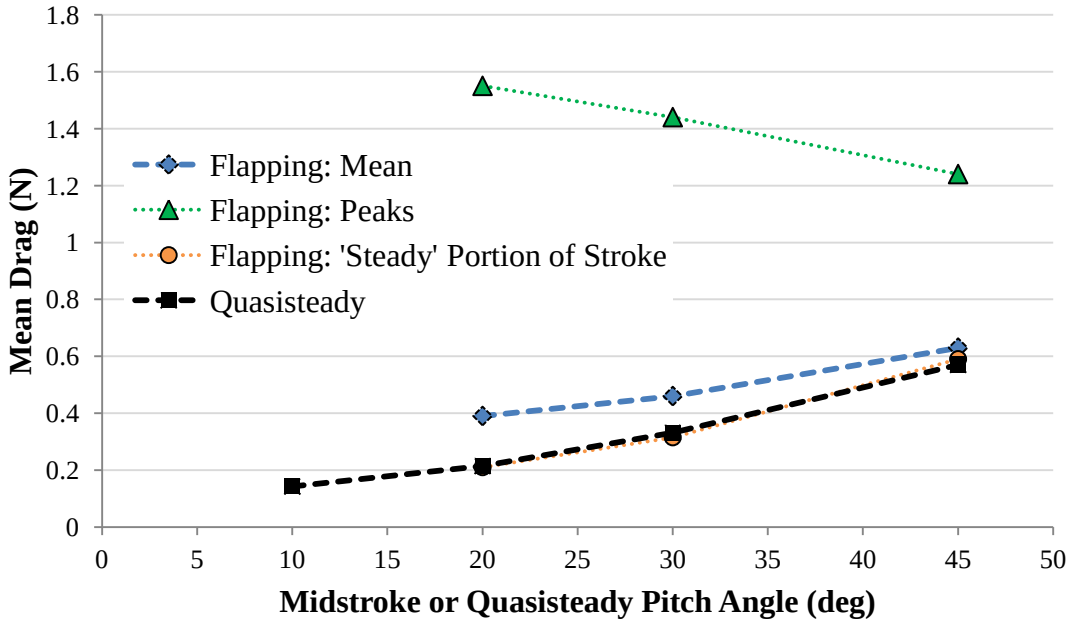

Figure 5.19: Stroke-averaged drag for the unsteady cases compared with quasisteady drag, average drag over the steady portions of the stroke, and instantaneous positive peak values.

The root vortex for the 30° case dissipates quickly in the wake, and the root vortex for the 20° case is not strong enough to remain distinct from the rotational vortex formed by the trailing edge, thus the two structures coalesce to form a closed vortex ring that remains in close proximity to the wing (Figure 5.20). The reduction in inflow from the reduction in tip/root vortex strength is combined with a reduction in the amount of fluid that is 'pulled' along with the wing in the previous stroke generating an in-plane induced flow. The result, from the perspective of the lift, is an attenuation of the peak magnitude.

The isosurfaces of Q-criterion in Figure 5.21 shows that post separation, there is more interaction with the (stronger) wake for the 45° case than the 20° and 30° cases. Note that the vortices generated near the tip during the wing flip are increasingly separated from the wing with decreasing pitch angle. More significantly though, note the relative pitch angles of the three cases at this point in the stroke. Rotational velocity is near its lowest values, therefore the flow over the wing is primarily attributed to the combination of in-plane induced flow and the induced flow normal to the stroke plane. As the wing's pitch angle is reduced at this point in the flow, the component of the resultant induced flow vector creates a reduced induced angle of attack. This balance between stroke reversal pitch angle and induced flow vector dictates the magnitude of the life peak, post-supination.

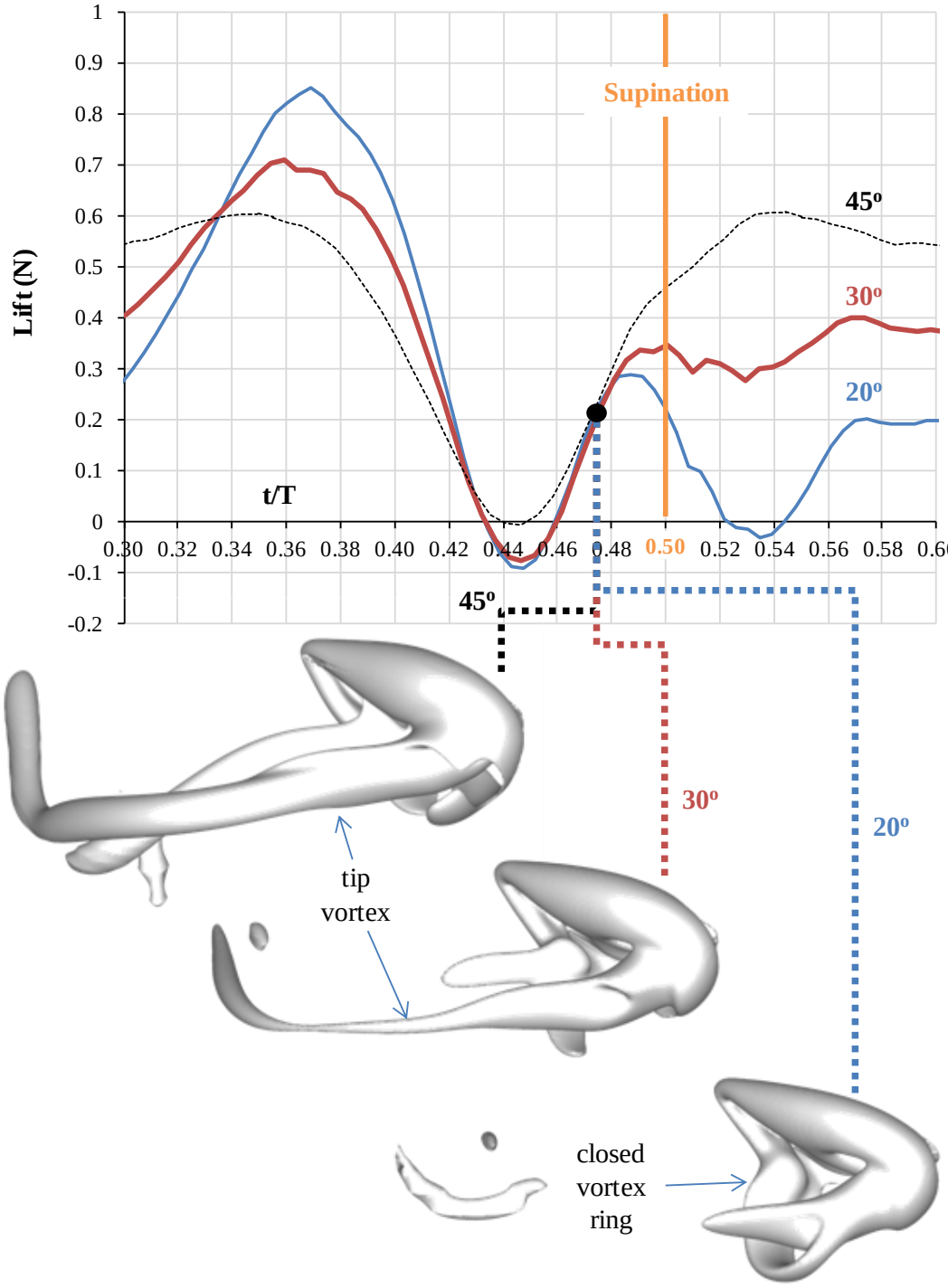

Figure 5.20: Detail of lift time history surrounding supination. Isosurfaces of Q-criterion for each case are plotted at t/T=47.5% to highlight factors affecting the loss in lift for the 20° and 30° cases.

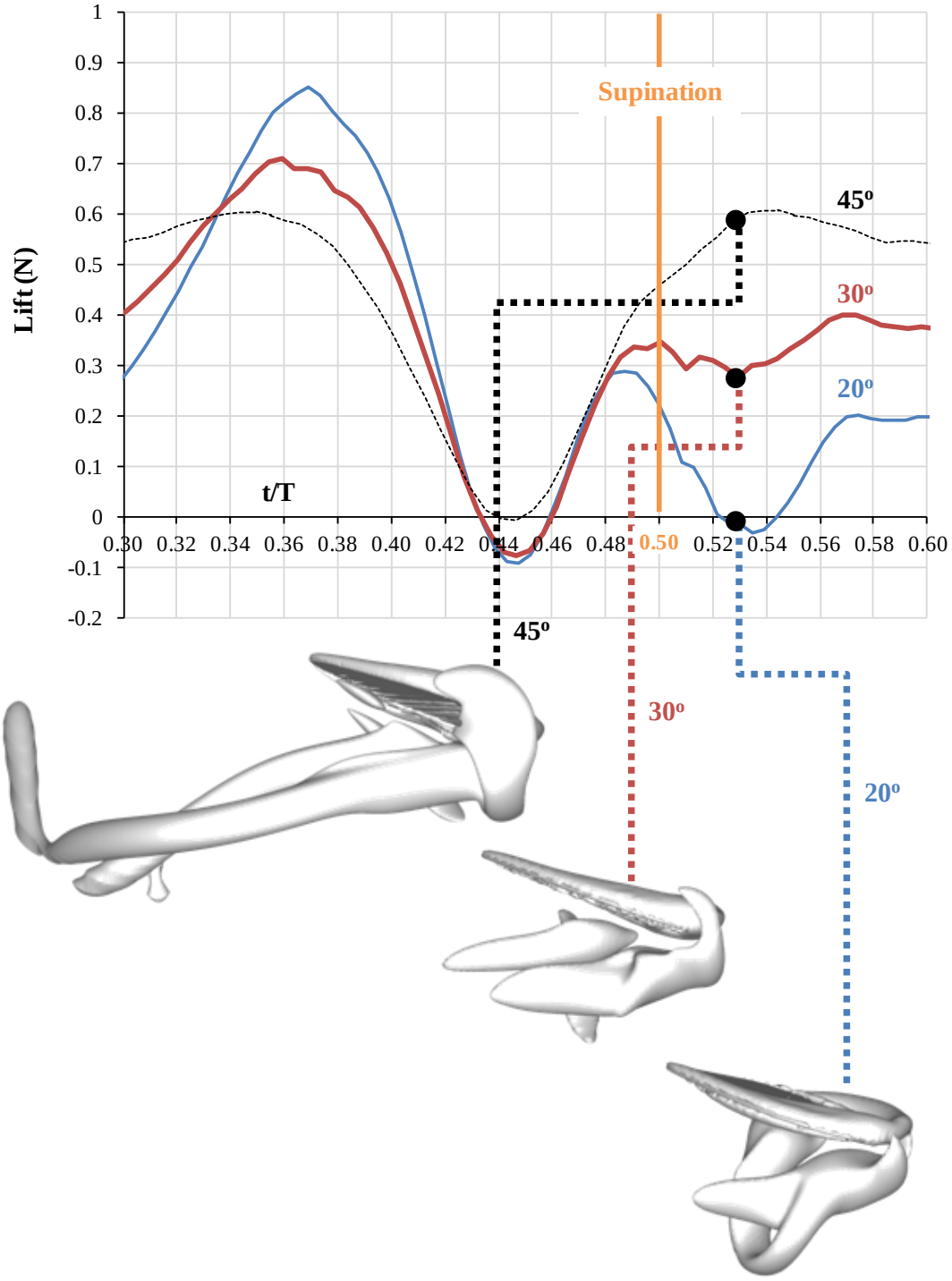

Figure 5.21: Detail of lift time history surrounding supination. Isosurfaces of Q-criterion for each case are plotted at t/T=53% to highlight factors affecting the differential behavior of the post-supination lift curve for the 20°, 30°, and 45° cases.

5.2.2 Induced Inflow

The time-averaged inflow in the stroke plane for the 20° and 30° cases is mapped in Figure 5.22. Both distributions over the stroke plane are similar in shape, with the 20° case having a slightly lower inflow magnitude. This is in line with the previous observations that the average forces over the stroke qualitatively follow the trend of the quasisteady simulations, where the instantaneous peaks show significant variation with changes in mid-stroke pitch angle. The inflow distribution for the baseline case in Figure 5.14b is also qualitatively similar, with a slightly greater inflow magnitude than the 30° case. The reduction in magnitude between the two modified pitch angle cases is further highlighted by the spanwise inflow distributions, plotted in below the contour plots in Figure 5.22. From the root through mid-span the inflow for the lower pitch angle case is lower, with a peak of $\lambda = 0.20$ for the 20° case, and $\lambda = 0.24$ for the 30° case. Outboard of the peak values, inflow distributions collapse to exhibit a common linear decrease towards the wingtip.

In spite of the increased inflow ratio across the span for the 30° case compared with that of the 20° case, as discussed previously, the mean lift plots of Figure 5.18 imply an increased effect of the downwash as mid-stroke pitch angle is reduced. This implication is borne out by noting that the wake trajectory in Figure 5.23 shows the reduced axial convection speed of the root and tip vortices as mid-stroke pitch angle is decreased. The plots are terminated as the vortex cores became to diffuse to reliably identify. This wake age became smaller with reduced pitch angle because those vortices that remained closer to the stroke plane were broken up as the wing passed over them for successive strokes. This is especially apparent in the 20° case where the vortex core that was shed at

$t/T = 25\%$ was critically disrupted almost exactly as the wing passed back over it at $t/T = 75\%$ when the vortex was only about 0.5 radii (or $1.2\bar{c}$ chords) below the stroke plane.

It is also interesting to note that as mid-stroke pitch angle is reduced, the wake tends to convect further inboard. This is likely attributed to the decreasing relative strength of the tip vortex compared with that of the root vortex, as the stronger vortex would tend to pull the weaker vortex towards it.

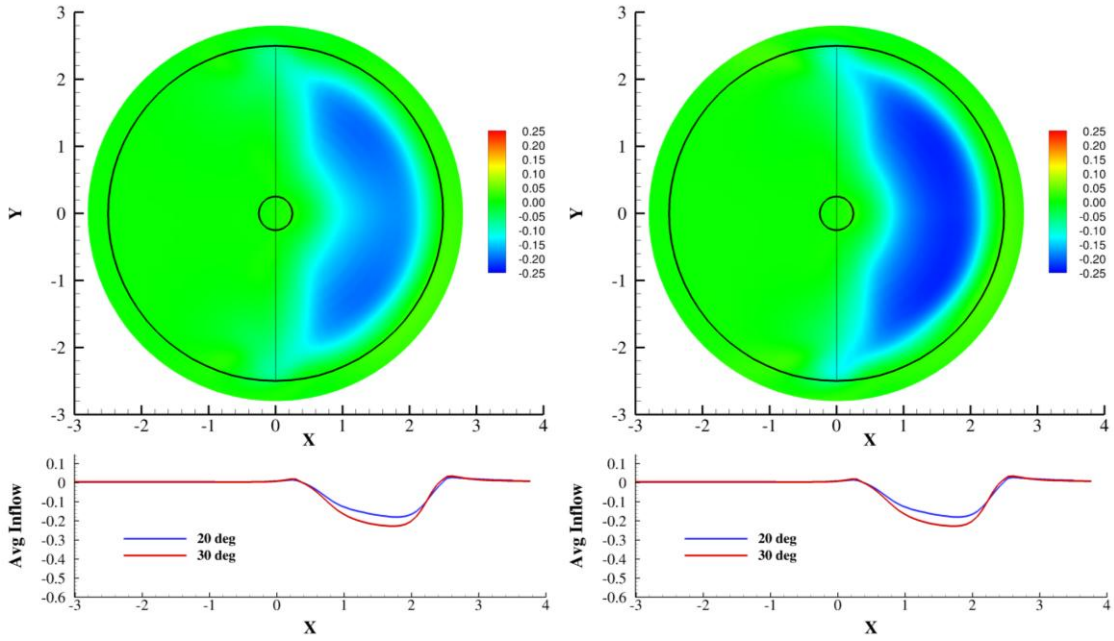

(a) 20° (b) 30°

Figure 5.22: Contours of time-averaged inflow ratio over a combined up/downstroke at planes parallel to the stroke plane for the (a) 20° and (b) 30° cases. Circles on contour plots indicate root and tip path radii. Plotted below each contour plot is the spanwise inflow profile at mid-stroke ($y = 0$).

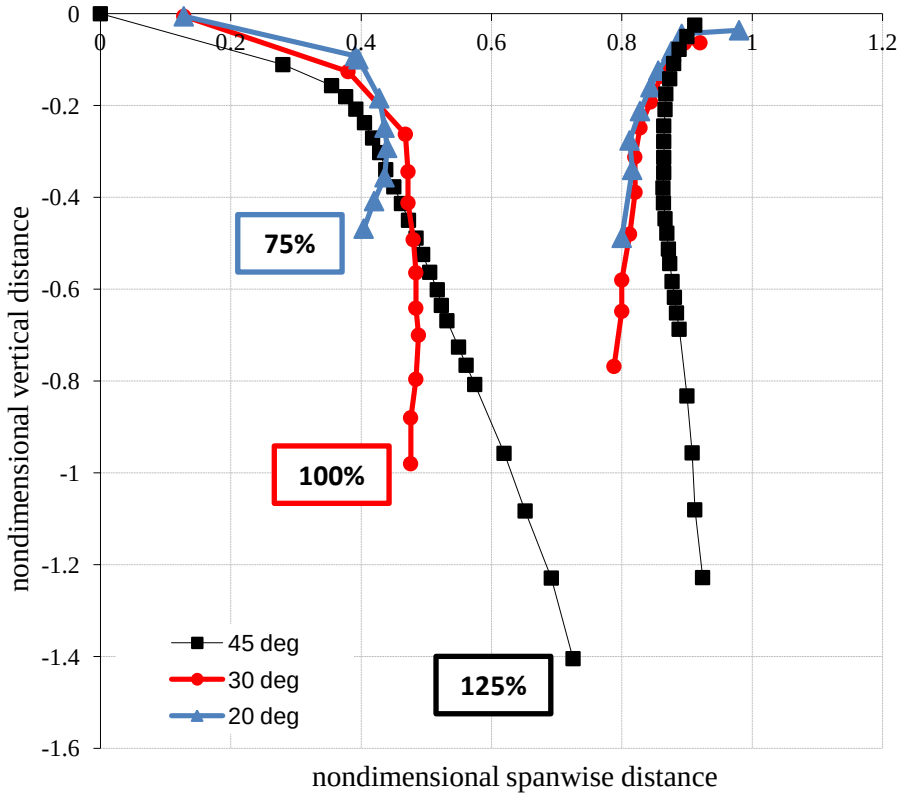

Figure 5.23: Mid-stroke root and tip vortex trajectories for modified pitch angle cases. Distances nondimensionalized by span length.

5.2.3 Power

In general, as seen with the quasisteady cases, the mean power requirements reduce with reductions in mid-stroke pitch angle. However, compared with the quasisteady cases, mean aerodynamic power for the unsteady cases is much less sensitive to reductions in pitch angle (Figure 5.24). This is almost entirely due to the relatively large power expenditures at stroke reversal for the unsteady cases. If we consider the peak stroke power, the power requirement *increases* with decreasing mid-stroke pitch angle which counterbalances the decrease we would expect from the quasisteady results. As we saw with the force peaks, these increased power requirements at stroke reversal are the

result of the increased pitching velocity required for the pitching flip with reducing mid-stroke pitch angle. If we however consider separately the mean power required for only the steady portions of the flapping stroke, in Figure 5.25 we see that it actually decreases with reducing mid-stroke pitch angle at a very similar rate as the quasisteady case, and in fact, the actual magnitudes of the power requirements are quite similar to the quasisteady values. It should be noted, however, that there is a significant increased mean aerodynamic power requirement over the quasisteady cases, and this effect is greater with decreasing mid-stroke pitch angle. Again, this is primarily attributed to the large peak power required at stroke reversal, as evidenced by the similar values to the quasisteady power requirements when the stroke reversal portion is taken out of the average.

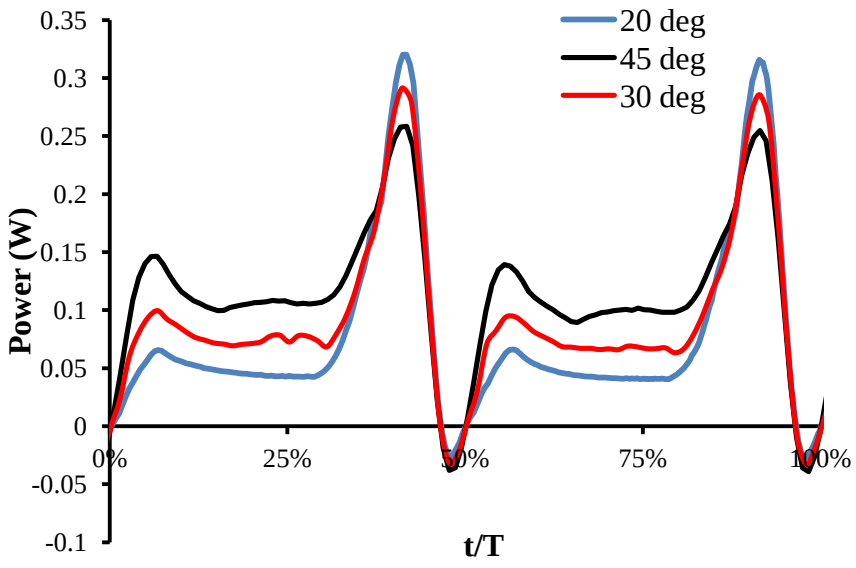

Figure 5.24: Power time histories for 20°, 30°, and 45° mid-stroke flapping cases.

Figure 5.26 shows that mean lift-to-power slightly decreases with reducing mid-stroke pitch angle, where there is an increase to a maximum value at $\alpha_{geom} = 20°$ for the quasisteady cases. As seen in Figure 5.25 and Figure 5.18, this is the result of an

increased mean power requirement, as well as a slightly reduced mean lift compared to the quasisteady cases. Therefore, although the mean power for the 45° case is the highest of all of the unsteady cases, the effective aerodynamic power loading is maximized for this case. Furthermore, the magnitude of the power being *extracted* from the flow during the last 5% of the up or down strokes is maximized for the 45° case.

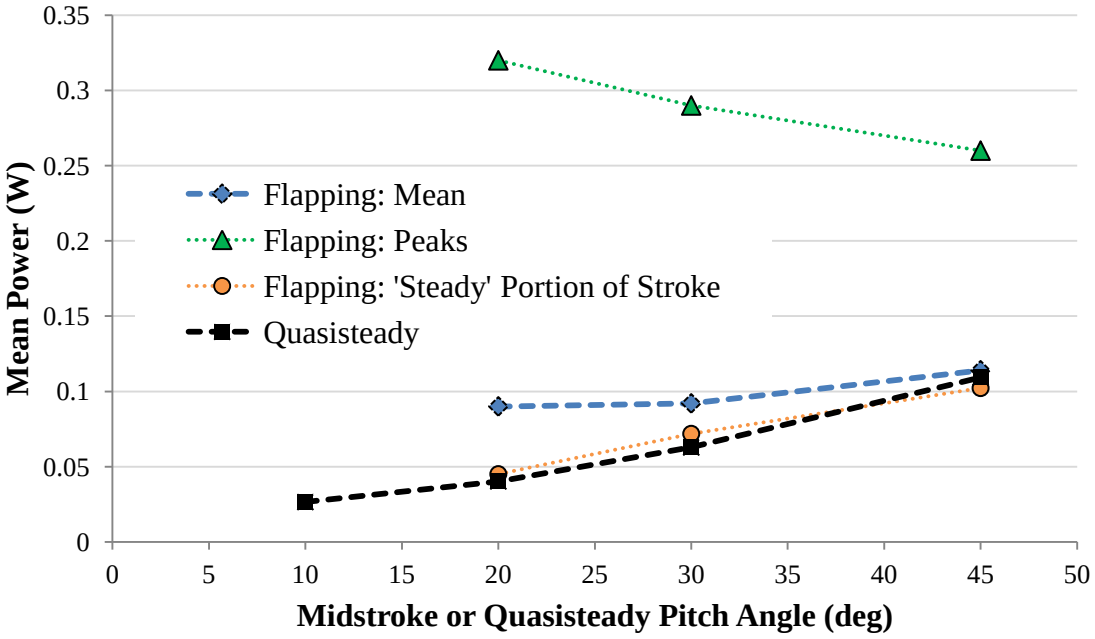

Figure 5.25: Stroke-averaged power for the unsteady cases compared with quasisteady power, average power over the steady portions of the stroke, and instantaneous positive peak values.

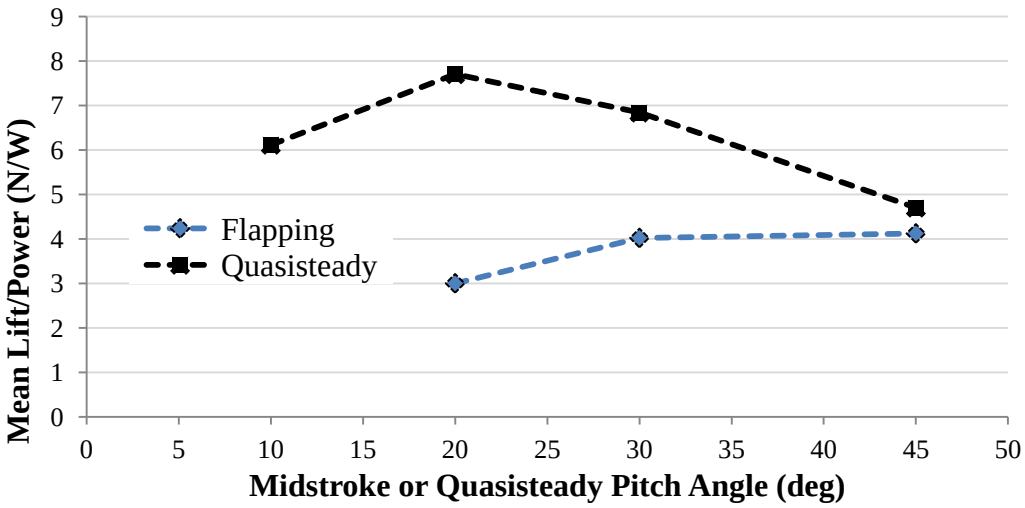

Figure 5.26: Mean lift-to-power ratio for the flapping and quasisteady cases.

5.3 High Reynolds Number Flapping

The final case uses the baseline kinematics (Figure 5.3, mid-stroke pitch angle of 45°) , but increases the Reynolds number one order of magnitude from $Re = 147$ to $Re = 1400$. Figure 5.27 provides an illustrative example of some of the computational difficulties that are faced at higher Reynolds numbers. Large laminar root and tip vortices dominated the flow for most of the stroke at $Re = 147$. However for $Re = 1400$, the root and tip vortices are more compact, and stronger in vorticity magnitude meaning that a finer mesh is required to adequately resolve them. Furthermore, the primary LEV, root and tip vortices are accompanied by smaller coherent vortex structures that arise as a result of shear layer instabilities that were previously damped by the increased viscosity. Finally, care must also be taken to damp non-physical oscillations arising from the sharper velocity gradients (recall Figure 2.3, for example).

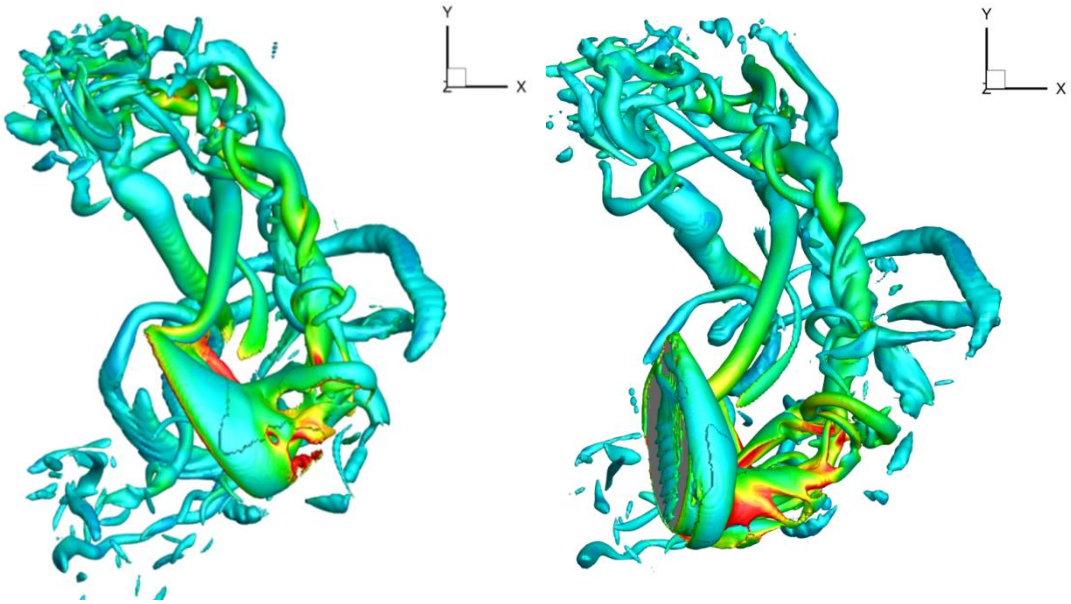

Figure 5.27: Isosurfaces of Q-criterion for the $Re = 1400$ flapping case at $t/T = 87\%, downstroke$ (left), and $t/T = 2\%, upstroke$ (right), colored by vorticity magnitude.

Although the $Re = 1400$ quasisteady cases were able to be run successfully with reasonable mesh sizes without the additional turbulence modeling, the kinematics of the flapping case dictate that the mesh be refined over a significantly larger area. Therefore, the LES solver is employed to properly account for the turbulence that develops, without needing to drive up the mesh count by refining to an impractically small mesh spacing over the entire stroke area. The present mesh contains 48×10^6 nodes, with a uniform spacing of 0.75mm in the stroke region. This spacing is roughly based on the observed largest eddies in the $Re = 1400$, $\alpha = 50°$ quasisteady case. The simulations are run in a fully explicit mode (AB2 on all terms) at a constant CFL of 0.3 with 2nd order Van Leer limited upwinding. Forces and flow visualizations are taken at the sixth full stroke, as periodicity took slightly longer to achieve than for the $Re = 147$ cases.

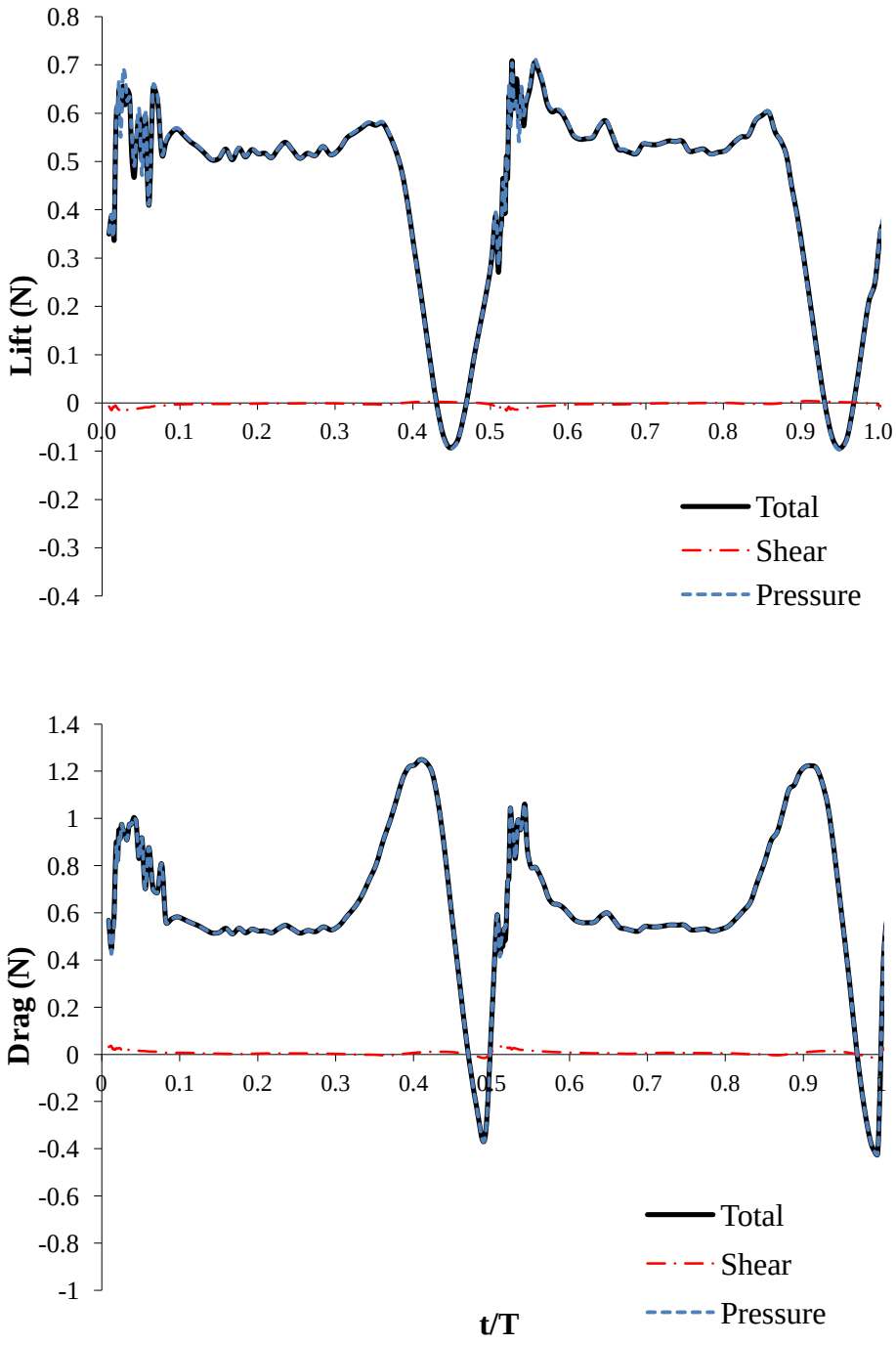

Figure 5.28: Computed lift and drag for the $Re = 1400$ flapping case decomposed into viscous and pressure components.

5.3.1 Forces

The lift and drag time histories plotted in Figure 5.28 show some level of stroke-to-stroke variation, particularly just after the stroke reversal peak. Nevertheless, they are qualitatively similar to the lift and drag of the baseline case. The same peaks occurring at a frequency of 1/per stroke exist in both cases, however the higher Re case also contains forces at higher frequencies, notably around stroke reversal. Much of this can be attributed to interaction with the increased unsteadiness in the shed wake. However, it must be noted that the "kink" in the lift and drag curves exactly at stroke reversal ($t/T = 0{,}50\%, \ldots$) are purely computational artifacts of the immersed boundary implementation. At the time step when the wing reverses direction, the IB nodes imposing the velocity boundary condition flip sign, causing a brief perturbation of the flowfield. The finer mesh combined with the reduced physical viscosity produces a stronger perturbation with less damping than was observed in the lower Re cases, where it was negligible. However, the higher frequency force peaks just after stroke reversal, as the wing enters the wake capture phase and interacts with the mid-scale vortices shed during the flip wake capture, are fairly mesh independent and appear to be physical in origin.

As expected, the shear forces for both lift and drag are essentially negligible at this Reynolds number, and therefore the mean values of lift and drag for the full stroke of 0.47N and 0.68N, respectively, are attributed almost entirely to inviscid forces. The mean values are nearly identical to the baseline mean values of 0.47N and 0.63N for lift and drag. Recalling Figure 4.7 for the quasisteady comparisons at similar Reynolds numbers, we see that the forces at $\alpha = 45°$, especially the drag, are relatively insensitive to

changes in Re in this range. However, it is still somewhat surprising that the mean lift is not slightly higher for the $Re = 1400$ case. This reduction in expected magnitude is likely due to the more complex wake capture phase where we see lift vacillating near the peak value, where for the lower Re case the lift increased smoothly to the peak.

The mean lift and drag during the steady rotational portion of the stroke are 0.52N and 0.53N, respectively. These values are again similar to the $Re = 147$ case where the mean lift and drag values were 0.52N and 0.59N, respectively. Both cases compare favorably with the quasisteady values, with lift again unexpectedly showing no significant increase in mean value at the higher Reynolds number.

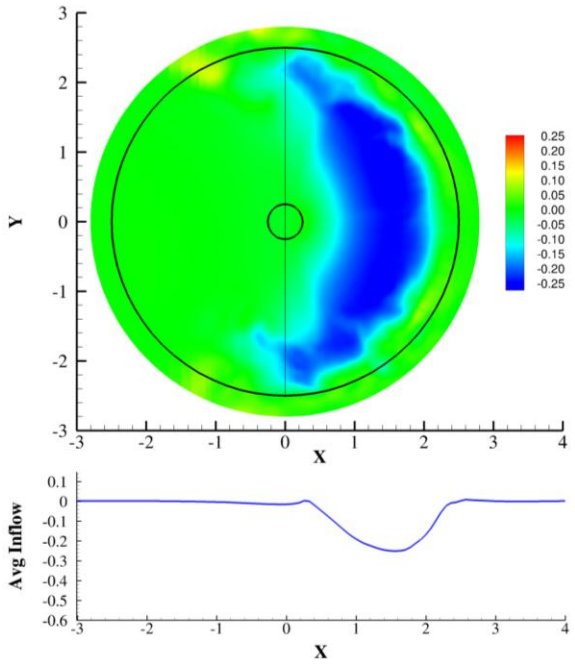

Figure 5.29: Contours of time-averaged inflow ratio over two combined up/downstrokes at planes parallel to the stroke plane for the $Re = 1400$ case. Circles on contour plot indicates root and tip path radius. Plotted below the contour plot is the spanwise inflow profile at mid-stroke ($y = 0$).

5.3.2 Induced Inflow

The stroke plane inflow shown in Figure 5.29 is computed by averaging over 2 full strokes, as opposed to the single stroke average of Figure 5.14 and Figure 5.22. Nevertheless, the asymmetry that was somewhat apparent in the lift and drag time histories is more apparent here. Strong vortices exist just outside of the stroke radius at pronation (top of Figure 5.29) that create an upwash. While these features are present at supination as well (bottom of Figure 5.29), they are significantly weaker. The spanwise inflow at mid-stroke peaks at $\lambda = 0.26$, the same as the baseline case. However, compared to the baseline case, the spanwise inflow distribution is less linear inboard of the peak. This difference is due, in part, to the additional averaging performed on the $Re = 1400$ case, however the relative decrease in size and increase in strength for the higher Reynolds number also has a significant effect on the shape of the distribution.

Figure 5.30 compares the root and tip vortex trajectories for the $Re = 1400$ and $Re = 147$ cases. As with the force time histories, the average path is roughly the same for the two cases, however the higher Re vortices tend to have a less monotonically linear trajectory, as their paths are affects by interactions by smaller vortices. Also note that even with the increased motion of the vortices along the wake trajectory, the axial convection speeds are quite similar even with the order of magnitude increase in the Reynolds number.

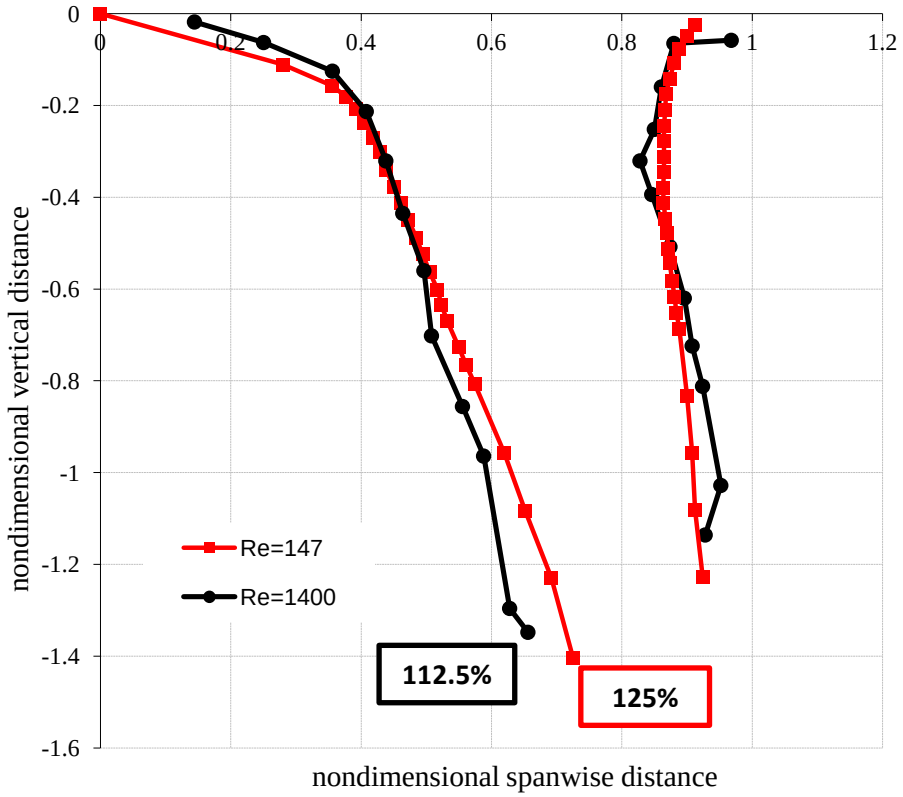

Figure 5.30: Mid-stroke root and tip vortex trajectories for $Re = 1400$ and baseline $Re = 147$ cases. Distances nondimensionalized by span length.

5.3.3 Mid-stroke Flow Visualization

One of the dominant characteristics of the flowfield for the quasisteady case at $Re = 1400$ and $\alpha = 50°$ (Figure 4.12) was a strong spanwise flow that peaked at 1.61 times the mean tip velocity at $r/R = 45\%$ span. This spanwise velocity was also coincident with the center of the compact LEV. Figure 5.31 plots isosurfaces of spanwise velocity at values of 0.25 and 0.50. Notice that while there is a large region of axial flow moving radially outwards, most of it is fairly low in magnitude. The extent of the region of higher spanwise flow is fairly limited, and only a small portion towards the outboard tip of the wing appears strongly associated with the LEV. The peak spanwise velocity is

0.68 and it occurs at 66% span – significantly different than the quasisteady results, even considering the 5° difference in pitch angles. This is partially the result of the flapping wing not having sufficient time to build the axial flow as in the quasisteady case. While the value at mid-stroke, t/T=25%, is low, the peak spanwise flow velocity increases to 1.10 times the mean tip velocity at the r/R=58% station by t/T=41% when the rotational deceleration begins.

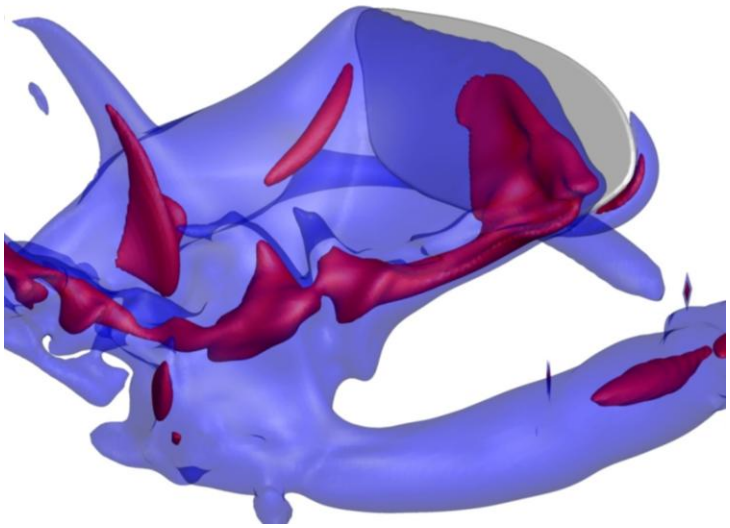

Figure 5.31: Isosurfaces of spanwise velocity normalized by mean tip velocity at values 0.25 (blue) and 0.5 (red). $Re = 1400$

A second factor affecting the axial flow magnitude is the increased magnitude of the inflow for the flapping case, resulting from the influence of the shed wake. Figure 5.32 shows the vorticity magnitude contours at a number of spanwise stations at mid-stroke, and Figure 5.33 plots the spanwise vorticity contours along with streamlines computed in a fixed inertial frame at the r/R=65% span location. Note that the streamlines are significantly more deflected for this case than for the comparable quasisteady case. From a simple momentum perspective, since the mean power is nearly identical for the flapping

and quasisteady cases, it appears that the additional momentum cost of accelerating the flow through the stroke plane is traded for that which would have been required to accelerate the axial flow. Also note that the LEV structure at the r/R=65% station in Figure 5.33 does not exhibit the complex secondary and tertiary vortex patterns that were observed in the quasisteady case.

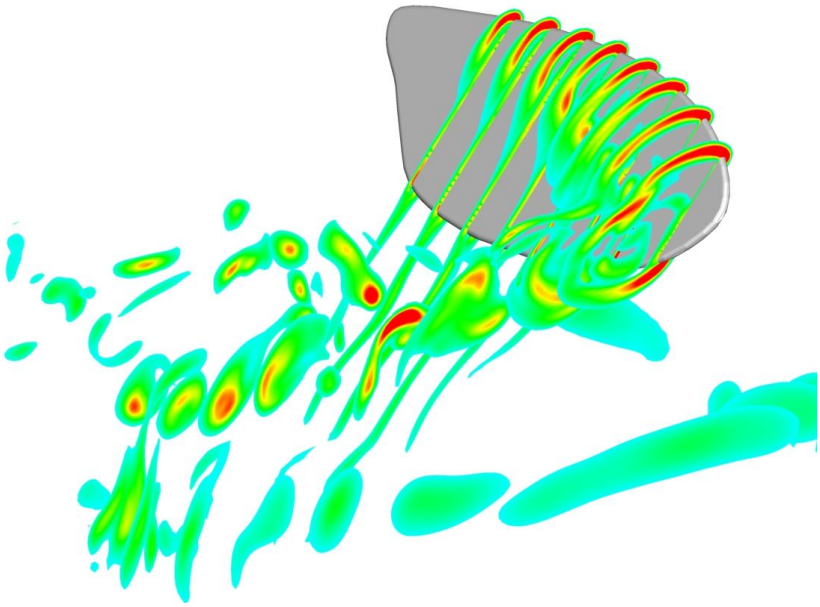

Figure 5.32: Mid-stroke vorticity magnitude contours (red counter-clockwise) at $r/R = 35\% - 87.5\%$ in increments of 7.5% r/R

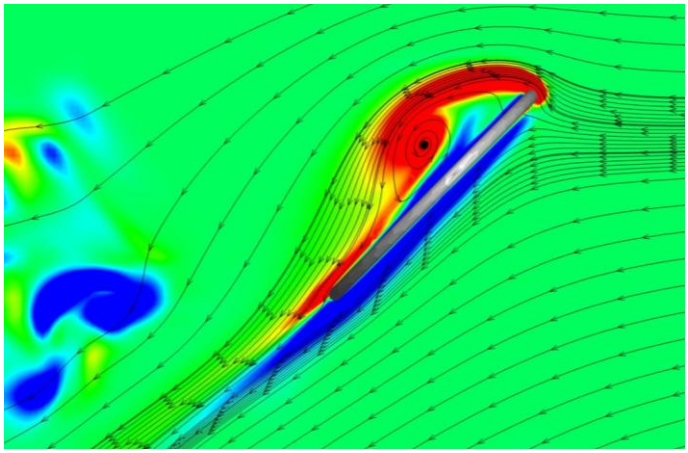

Figure 5.33: Contours of spanwise vorticity with streamlines computed in the inertial frame at $r/R = 65\%$. $Re = 1400$.

5.3.4 Power

The aerodynamic power required over a full stroke for the $Re = 1400$ flapping case is plotted in Figure 5.34. Based on the quasisteady power comparison across Re (Figure 4.14) which showed a small (approximately 10%) increase in aerodynamic power required for the high Re case, the aerodynamic power for the $Re = 1400$ flapping case is quite similar to the power for the baseline $Re = 147$ flapping case. As with the lift and drag, the primary difference is the increased high frequency content, particularly after stroke reversal. The asymmetry seen in the lift and drag results is also seen here. Nevertheless, the mean for the entire stroke is 0.11 W, which is the same as was seen for the $Re = 147$ case, and is similar to the quasisteady results of approximately 0.12 W. Since we saw that mean lift was also nearly identical to the lower Re case, this means that the effective power loading for the strokes are the same (4.12 N/W). This similarity is, again, consistent with the quasisteady results.

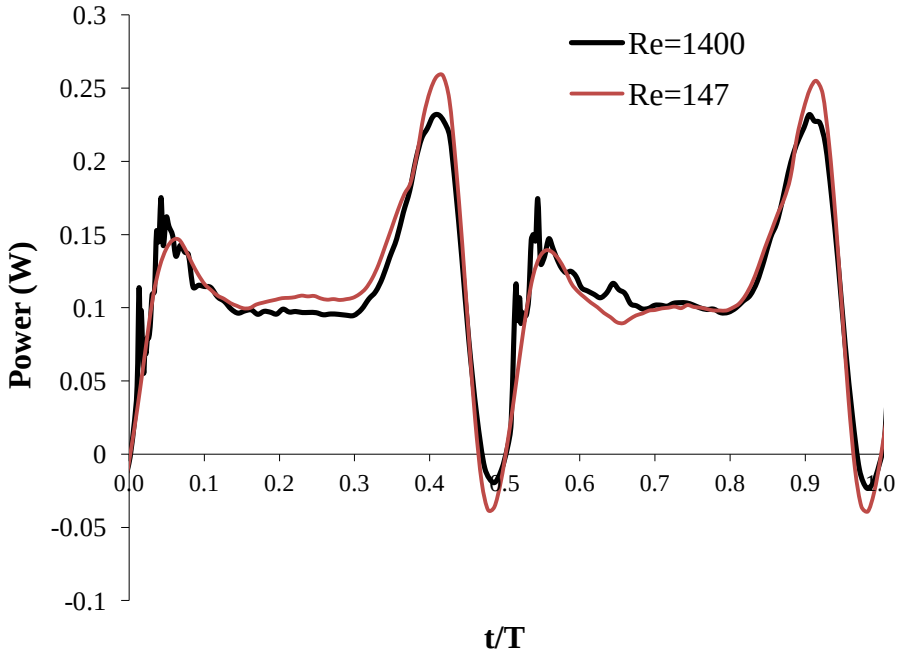

Figure 5.34: Power time history of the $Re = 1400$ flapping case compared against the $Re = 147$ baseline case (4^{th} stroke).

5.4 Summary

The flow visualizations of the idealized stroke of a *Drosophila* wing presented in this chapter allowed for a detailed description of some of the salient features of the flowfield, by studying both 2D cross- sectional pressure, velocity and vorticity fields, as well as the 3D vortex field. These visualizations were discussed in terms of their relevance to various events in the force and power time histories, as well their correlation to the quasisteady results of the previous chapter.

- During the steady rotation portion of the stroke the LEV continues to grow for at least half of the upstroke. Although the low pressure region increases in size with this growth, the pressure lift decreases. This loss in lift is apparently

balanced by a steady increase in shear lift, resulting in a nearly constant total lift during steady rotation.

- Peak lift for this baseline case (0.61N) occurs as the wing pitches up approaching stroke reversal. The peak drag (1.24N) is nearly coincident with the onset of rotational deceleration, at a stroke-time just before the flip midpoint.
- Over the last 5% of each half stroke, although the wing is at a geometric angle of attack greater than 90^{o}, the induced flow from the stroke causes an induced flow that puts the wing at an effective lift producing angle of attack. The result is a rapid increased in lift coupled with a *negative* drag over this period.
- After stroke reversal, the viscous force contribution reaches a peak, apparently because of a lack of recirculatory flow at the wing surface. Computationally this adds to the potential for increased error magnitude in computed forces. During stroke reversal, the imposed body acceleration, which enters into the surface boundary condition on pressure, is near its maximum value.

The comparison of the baseline case with experiment showed reasonable mean force values, especially for drag, however both forces were overpredicted. A number of potential causes for the larger discrepancies in peak force values were presented:

- It is speculated that the steady rotation differences in lift are the result of the wing operating at a different effective angle of attack than the experiment, due to a smaller induced stroke plane inflow.
- A source of induced flow is identified in the close proximity of the shed root and tip vortices. Because the influence of the vortex jet that forms between

them may be significant, the position of these vortices, determined in part by the wing geometry, is critical to accurate predictions. Thus it is speculated that the different wing root geometry of the computations may have played a part in the inaccurate predictions. This also helps to explain the underprediction of the pre-stroke-reversal lift peaks as well and the relative speed of the lift recovery after stall.

- All computational lift and drag peaks occurred in advance of the experimental peaks. Because the peaks occur near points of maximum body acceleration (either pitching or rotational) this discrepancy may simply have to do with the imprecise matching of kinematics.

For the baseline case the wake structure was examined to quantify its development and potential influences on the force:

- At the mid-stroke plane, the developing root vortex is pushed rapidly outboard early in its formation. The result is a root vortex that is located near mid chord, close to the tip vortex, but still near the stroke plane, giving the vortex pair increased influence over subsequent strokes.
- Just after stroke reversal, a pair of counter-rotating vortices become positioned just upstream of the wing on the lower surface. The factors affecting their development as well as the vortex pair's influence on the present case's forces is an interesting topic for future study.
- The shed wake at the stroke reversal point resembles that left by the pitching and plunging elliptical wing studied by Dong and colleagues. The primary qualitative differences in the shed vortices at supination appears to be the

asymmetry of the vortex ring pair resulting from the disparity in strengths of the root and tip vortex.

- In spite of the increased inflow compared to the quasisteady cases, the forces remain nearly the same between the two cases

In order to study the sensitivity of the baseline results to changes in kinematics, as well as to compare them to the quasisteady results of the previous chapter, the baseline kinematics were modified by changing the mid-stroke pitch angle to 20° and 30°

- As Expected, mean lift and drag for the stroke decrease with mid-stroke pitch angle, however peak lift and drag values increase.
- Mean lift for the 'steady' portion of the stroke was found to decrease at the same rate as the quasisteady case for decreases in mid-stroke pitch angle, however there was an offset in magnitude. Mean drag for the steady portion of the flapping stroke and the quasisteady cases agreed quite well with each other.
- It was found that the primary factor dictating the lift-peak post-stroke reversal is the balance between stroke reversal pitch angle and induced flow vector resulting from the combination of in-plane induced flow and inflow through the stroke plane.
- The effect of the differences in inflow between the flapping cases and quasisteady cases was shown to be greater as the mid-stroke pitch angle was reduced. This manifested as a reduction in lift as compared to the quasisteady results as mid-stroke pitch angle decreased.

- While the distribution of the mean inflow through the stroke plane did not vary greatly with reduced mid-stroke pitch angle, the wake trajectory showed significant differences. Reductions in pitch angle produced a shed wake that descended more slowly away from the stroke plane, dissipated at earlier wake ages, and tended to move further inboard
- The $45°$ mid-stroke pitch angle case required the highest mean aerodynamic power of the three cases. Therefore, in cases where it is advantageous to minimize mean power expenditures (such as hover), the $45°$ case is the leaset efficient. However, in other measures it compared more favorably against the $20°$ and $30°$ cases:
  - Effective aerodynamic power loading is maximized for the $45°$ case. This is in contrast to the quasisteady cases which showed the peak lift-to-power at $20°$
  - Instantaneous peak power requirements are minimized
  - Instantaneous power extraction is maximized

Finally, the baseline kinematics were re-run at a Reynolds number of $Re = 1400$ with the LES solver.

- The lift, drag and power curves for the $Re = 1400$ case were similar in trend and magnitude to the $Re = 147$ flapping case. The primary difference was the increased higher frequency content, particularly surrounding stroke reversal, and a slight asymmetry in inflow and forces between strokes.
- Unlike the lower Re case, the flow topology of the $Re = 1400$ case appeared somewhat different than its quasisteady counterpart. There was a marked

reduction in peak axial flow, and a weaker singular LEV was seen in place of the stronger multi-part LEV of the quasisteady case. These differences were attributed, in part, to the significant difference in induced flow between the two cases.

- The inflow distribution at the stroke plane showed some asymmetries in the strength and location of upwash near stroke reversal. These differences are tied to the asymmetries in forces at stroke reversal.
- The wake evolution showed a similar axial convection speed as the lower Re baseline case, with roughly the same path aside from additional motion caused by interactions with smaller regions of vorticity.

Chapter 6 –

Closure

Developing a deeper understanding of the flowfield and the aerodynamic forces associated with flapping-wing flight is critical to furthering our ability to build efficient flapping MAVs. This final chapter presents a summary of the work performed during the development of the immersed boundary solver, and the application of that solver to help further that understanding.

6.1 Summary

The primary objectives of this work have been to develop a robust computational platform well-suited to studying low Reynolds number incompressible flapping-wing flight, and to apply the tool to an idealized flapping-wing stroke in order to build a more detailed understanding of the aerodynamic mechanisms responsible for the production of unsteady forces during the stroke.

The Cartesian structured immersed boundary incompressible Navier-Stokes solver computational platform that was developed, IBINS, was verified and validated as a baseline NS solver using an exact solution to the incompressible governing equations, and a comparison with published computational data. Immersed boundaries were then implemented, and the solver was validated using simple flows representative of the Reynolds number range of interest for the flow applications, $Re = O(10^2 - 10^3)$. IBINS

was shown to exhibit the expected second order convergence away from boundaries, and with the application of the immersed boundaries, the vortex development at the low and high ends of the applicable Reynolds number range was shown to match experimental data. The code was extended to include a dynamic Smagorinsky model for LES calculations of moderate Reynolds number. The SGS model was validated by demonstrating the expected turbulent energy decay in an isotropic flowfield for meshes with spatial resolutions lower than that which would be required for a direct Navier-Stokes solution.

The solver was then applied to simulate a rigid model *Drosophila* wing in steady rotation at a fixed pitch angle. The pitch angle was incrementally varied from $0° - 90°$ across two Reynolds numbers, $Re = 120$ and $Re = 1400$. These simulations were compared against published experimental data of a similar kinematically scaled wing and showed good agreement. Because experimental data was available with which to compare, these rotating quasisteady cases provided further validation of the code for moving boundaries and the force computation methodologies. Visualizations of the near-body flowfield were made specifically addressing the spanwise flow, the leading edge vortex topology, and the velocity distribution at the wing's suction-side surface.

Next, kinematics from the Robofly mechanical flapping apparatus were simulated at a Reynolds number of 147. These kinematics represented an idealized *Drosophila* hovering wingstroke, consisting of a periodic rotational flapping with flips about an axis parallel to the span at the end of each half stroke. At the mid-point of each half-stroke, the wing was at a pitch angle of 45°, and for a middle portion of this stroke, the wing was moving with

a constant rotational velocity and a constant pitch. Each half stroke was symmetric, and only one wing was simulated with no mirror or symmetry plane to simulate the effects of a second wing (similar to the experiment). The computed forces were compared with experimentally measured values, and discrepancies were discussed. A detailed description of the stroke in terms of force, power, wake and kinematic events was provided, with support from detailed flow visualizations of the near and far wake generated during the stroke.

The baseline Robofly kinematics were then modified by reducing the mid-stroke pitch angle to $30°$ and $20°$. The corresponding changes in forces and power were noted, and a detailed description of the key differences in the unsteady forces was provided, again supported with flowfield visualization. Additionally, comparison of the expected trends with changes in pitch angle based on the quasisteady cases were made.

Finally, the Reynolds number of the baseline kinematics was changed from $Re = 147$ to $Re = 1400$. This served as a test case for the LES solver portion of IBINS. Flow visualization was provided, and a discussion of the sensitivity of the force and power time histories to the Reynolds number change was made.

6.2 Observations and Insights

A number of relevant observations, conclusions and contributions resulting from the development of IBINS and its applications to flapping wings were arrived at in this work.

6.2.1 IBINS Development

IBINS went through a variety of incarnations and implementations before arriving at the form discussed in this work. While immersed boundaries are, in principle, well-suited to the present flapping-wing applications, it was found that without certain modifications to the baseline methodologies, and efficient implementations of algorithms, the IB technique could yield computationally expensive, unstable, oscillatory, or overly dissipative results. Key insights gained from the development of IBINS relating to immersed boundaries and flapping wing research are as follows:

1. For a steady case with non-moving boundaries, the boundary identification process is a pre-processing step and its efficiency is not an issue. However, for the moving boundary cases where this identification needs to be performed at each time step, the choice of identification methodology is key to an efficient code. Depending on the mesh density and the immersed boundary surface definition, the simple vector cross product identification technique first employed could take 10% of the iteration time. The barycentric coordinate methodologies described in Chapter 3 reduced the per-iteration time to less than 1% for all cases in this work. It required a triangulated surface however, therefore if the surface mesh is defined using other regular polygons, it would be recommended to re-tessellate the polygons into triangles, even per iteration, in order to maintain efficiency.
2. By decoupling the pressure and the velocity fields, the collocated variable arrangement allows isolated pressure or velocity oscillations to propagate

throughout the flowfield. This potential can be mitigated without immersed boundaries or with a strongly coupled pressure-velocity formulation by adding in a higher order dissipation term. However, for the fractional step method, in which the pressure and velocity fields are loosely coupled by a Poisson equation, this dissipation becomes slightly less effective. When immersed boundaries are added in addition to the fractional step methodology, the inherent oscillations for a moving boundary caused by mesh nodes moving in and out of the solution domain, forces the required dissipation to be so large as to damp the physical vortices of interest. Therefore, with immersed boundaries and a fractional step method, the staggered mesh arrangement should be employed to incorporate coupling of the pressure and velocity fields.

3. The velocity gradient field is very sensitive to the Reynolds number. As Re is increased, velocity gradients rapidly rise with it. This results in increased gradients at the immersed surface and therefore increased potential for problems with oscillatory flowfields. It was found that implementing some form of upwinding helped reduce non-physical mesh-scale oscillations and speed convergence of the velocity equations. QUICK upwinding provided the most effective elimination of these oscillations, but at the greatest computational cost. The less complex second order slope-limited upwind schemes provided a reasonable balance of computational efficiency and solution accuracy. For the lower Reynolds number quasisteady and steady

cases, the simple second order central discretization proved sufficient and non-oscillatory.

6.2.2 Force Production on Flapping Wings

6.2.2.1 Quasisteady Impulsively Started Rotation

1. Forces reached a steady value for all pitch angles and both Reynolds numbers. This indicates that no unsteady shedding of the LEV was observed through the full course of rotation. Thus the range of "Low" Reynolds numbers at which the steady LEV phenomenon exists included $Re = 1400$.
2. Forces did not reach steady values until $70°$ of rotation after the impulsive start. This means that for the idealized flapping stroke, where there is $59°$ of steady, fixed-pitch rotation, there is less justification to assume that the quasisteady values of lift and drag will hold. We also see in the flapping case that the LEV continues to grow throughout the steady portion of the stroke.
3. For the $Re = 120$ cases, the peak spanwise flow was found to not coincide with the center of the LEV. Instead, unexpectedly the peak region of spanwise flow formed just aft of the wing. This aft spanwise flow was observed in the $Re = 147$ flapping cases as well, and provided a mechanism for the outboard convection of the root vortex towards the tip.
4. For the $Re = 1400$ cases, the peak spanwise flow was found to coincide with the center of the LEV, as expected. Both the $Re = 120$ and $Re = 1400$ cases showed stable vortices after $70°$ of rotational travel distance, however. Therefore, LEV

stabilization is not necessarily related to a convection of momentum out of the vortex through its core.

5. The wing surface velocity maps for the quasisteady cases provided a more detailed description of the LEV topology than is seen elsewhere in literature. In spite of the far more complex flowfield that is observed for the $Re = 1400$ cases, with secondary and tertiary vortices formed at the leading edge, the computed forces, particularly drag, again are not particularly sensitive to Reynolds number in this range.
6. The power required for the quasisteady wing increased linearly above a pitch angle of 15°, indicating that it can be simply estimated from the bluff body area. More importantly, aerodynamic power required was shown to not significantly vary with Reynolds number between the $Re = 120$ and $Re = 1400$ cases.
7. Reynolds number was shown to have a strong effect on the magnitude of L/D. $(L/D)_{max}$ for the $Re = 1400$ cases was more than twice that of the $Re = 120$ case.
8. The effect of Reynolds number on lift/power was less significant, specifically for pitch angles below 40°, which would seem to indicate that the change in Reynolds number produces an outboards movement of the effective spanwise location of the drag. However, flow visualization at the wing's upper surface appeared to indicate that the peak spanwise location moves *inboard* at the higher Reynolds number.

6.2.2.2 Idealized Flapping Stroke

1. Stroke-averaged lift and drag are shown to not be well predicted by the quasisteady values (although the trends with changes in kinematics are qualitatively similar). However, when the pronation and supination portions of the strokes are removed from the averaging, the lift, drag, and power are predicted quite well by the quasisteady simulations. In a flapping wing insect such as *Drosophila* with a flapping frequency of 200 Hz, the sensory feedback and body dynamics are not fast enough to respond to these high frequency force peaks, therefore a quasisteady simulation, particularly in hover, provides a reasonable estimate for dynamics and control applications.
2. The post-stroke-reversal lift recovery was shown to be critically dependent on a balance between the pitch angle at stroke reversal and the induced inflow angle. The induced inflow angle itself is dependent on the relative magnitudes of the in-plane induced flow and the induced flow perpendicular to the stroke plane. For this idealized stroke, these dependencies are fixed by mid-stroke angle. However by modifying the kinematics to increase the effective angle of attack just after stroke reversal, the loss of lift at stroke reversal observed in the lower mid-stroke pitch angle cases might be avoided.
3. It was shown that inflow below the stroke plane rapidly contracts to form a strong vortex jet at 49% the velocity of the mean tip velocity only 0.42 radii below the stroke plane. The jet is the result of the interaction of the root and tip vortices. This interaction is strong because of the relative size of the vortices at the lower

Re, the vortices' relative proximity when formed as a result of the low aspect ratio wing, and the trailed spanwise peak flow seen in the quasisteady cases which forces the root vortex outboard towards the tip vortex.

4. While one would traditionally expect a contraction of the trailed tip vortex towards the root in a higher Reynolds number rotating wing, after a brief period of contraction for the tip vortex, the opposite is shown to happen for the low Reynolds number case.
5. Interaction with the shed wake is shown to lead to the production of a vortex pair oriented perpendicular to the stroke plane and upstream of the wing just after stroke reversal. Their size and strength appears correlated with the lift peak just after stroke reversal, however this was only observed on the baseline $45°$ flapping case.
6. For the low Reynolds number flapping cases, the pressure lift *decreases* during the mid portion of the stroke, however there is a balance of shear and pressure forces that results in a near constant total lift for all pitch angles simulated. Then it is surprising that for the higher Reynolds number case we still see a near constant lift over the mid-portion of the stroke, since the shear forces are not significant in the total force.
7. Mean lift for the 'steady' portion of the flapping stroke was found to decrease at the same rate as the quasisteady case for decreases in mid-stroke pitch angle, however there was an offset in magnitude. Mean drag for the 'steady' portion of the flapping stroke and the quasisteady cases agreed quite well with each other.

8. By comparing the forces generated during the steady portion of the stroke to those of the corresponding quasisteady cases, it was shown that as mid-stroke pitch angle is reduced, the influence of the induced flow through the stroke plane on force production is *increased.* The wake for the reduced mid-stroke pitch angles remains closer to the stroke plane as mid-stroke pitch angle decreases.
9. The 45° mid-stroke pitch angle case required the highest mean aerodynamic power of the three cases. Therefore, in cases where it is advantageous to minimize mean power expenditures (such as hover), the 45° case is the leaset efficient. However, in other measures it compared more favorably against the 20° and 30° cases:
    - Effective aerodynamic power loading is maximized for the 45° case. This is in contrast to the quasisteady cases which showed the peak lift-to-power at 20°
    - Instantaneous peak power requirements are minimized
    - Instantaneous power extraction is maximized
10. The mean values for lift and drag change less than 10% by increasing the Reynolds number one order of magnitude. This shows that forces are somewhat independent of Re at this range, although flow structures are significantly different. This was observed for the flapping as well as the quasisteady cases and is similar as to what was observed by Sane [23] "[Although] viscosity is necessary for vorticity generation, its contribution to net forces is very small beyond *Re*=100 and the forces may be predominantly due to the dynamic pressure

gradients across the wing." However, the present study would extend that conclusion to say that viscosity's contribution to net forces is small below $Re \approx 1000$.

6.3 Future Directions

Some of the most interesting conclusions reached have to do with the sensitivity of the forces to changes in Reynolds number. As a direct continuation of this work, it would be useful to simulate the modified mid-stroke pitch angle kinematics at $Re = 1400$ to see if the conclusions about the stroke reversal lift peaks hold. Furthermore, running a parametric sweep of the Reynolds number would facilitate building a more complete understanding of this and other Reynolds number dependencies.

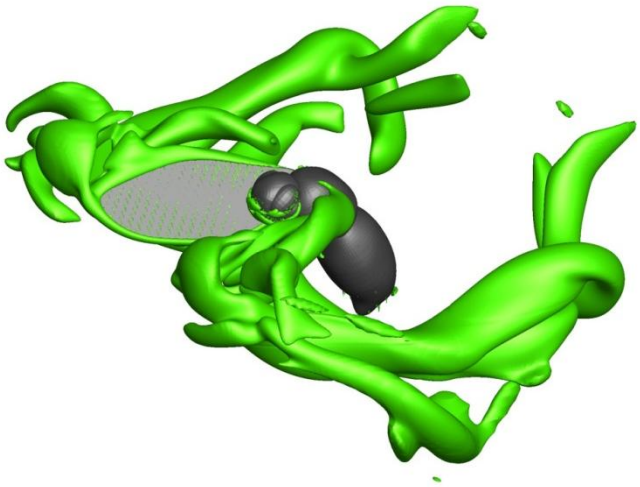

Figure 6.1: IBINS simulation showing iso-surfaces of Q-criterion surrounding flapping wings in steady axial descent.

While hovering flight was the goal of the present simulations, moving to steady flight simulations with similar kinematics could further expand on the above conclusions. It would particularly be interesting to characterize the various aerodynamic modes present when moving from hover to axial descent (Figure 6.1), where wake interaction is increased. It is at present unclear what would happen to the required power and the aerodynamic efficiency in these modes. Furthermore, as of this writing, the code has already been used in a non-hover mode to compute stability derivatives for the configuration shown in Figures 6.1 and 6.2 to be used in improving the predictions of quasisteady aerodynamic models [92].

While the capability was not utilized in this work, IBINS can compute the flowfields around multiple bodies moving separately (Figure 6.2), opening up the possibility to study how the forces and flowfield are affected by asymmetries in the flapping stroke, and the presence of a vehicle or insect body.

The incompressible solver developed for this work, while effective, is only a starting platform. With continued development, IBINS can become a far more versatile solver and provide insight into a variety of low Reynolds number fluid dynamics problems. Some potential next steps that would improve efficiency, stability, and the range of problems for which the code is efficient include:

- Application of cut-cell immersed boundary methodologies specifically geared towards reducing spurious pressure oscillations (e.g. the mass conservative method of Seo and Mittal [93])

- Implementation of a parallel multigrid Poisson solver to decrease iteration time, and improve convergence.
- Modification of the dynamic Smagorinsky model to smooth and limit the Smagorinsky constant based on a weighted average over particle paths [67]. This would eliminate the current ad-hoc Smagorinsky constant limiting and would improve stability for moderate Re flows.
- Implementation of an inertial frame version of the code, and/or application to curvilinear coordinates to allow for better positioning of nodes. This could dramatically reduce mesh node count for a number of problems.
- Implementation of fluid/structural coupling allowing externally provided forces to dictate or modify the prescribed motions of the immersed bodies. This modification would open up the possibility of studying, for example, gusts on flapping wings, trimmed flight, and flexible membrane non-prescribed simulations.

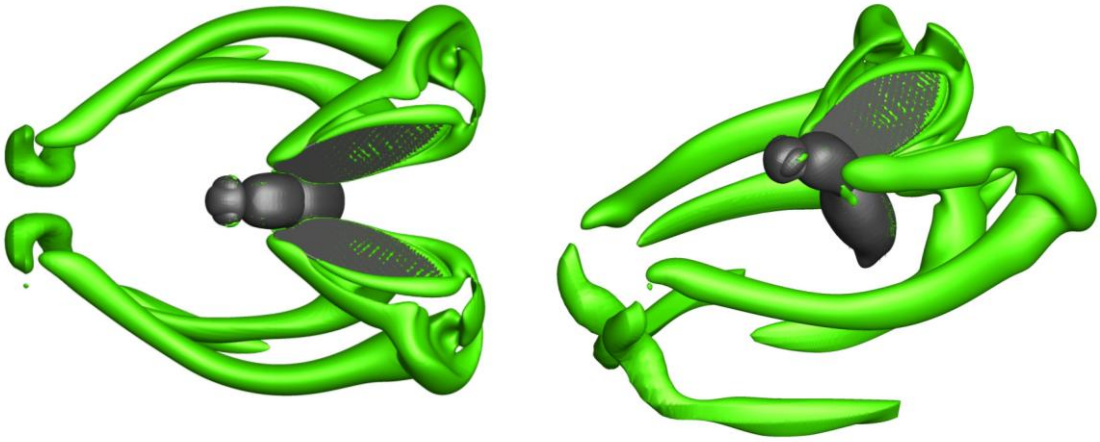

Figure 6.2: Top and isometric views of the multi-body capability of IBINS, showing a model insect body and two flapping wings.

Bibliography

[1] J. Roget, J. Sitaraman, R. Harmon, J. Grauer, J. Hubbard and S. Humbert, "Computational Study of Flexible Wing Ornithopter Flight," *Journal of Aircraft,* vol. 46, no. 6, 2009.

[2] R. C. Michelson, "Entomopter and Method for using the Same". United States of America Patent 6,082,671, 4 July 2000.

[3] J. Pereira, D. Bawek and I. Chopra, "Design and Development of a Quad-Shrouded-Rotor Micro Air Vehicle," in *American Helicopter Society 65th Annual Forum*, Grapevine, Texas, 2009.

[4] M. Benedict, "Fundamental Understanding of the Cycloidal-Rotor Concept for Micro Air Vehicle Applications," *Ph.D Thesis, University of Maryland, College Park,* 2010.

[5] B. Singh, "Dynamics and Aeroelasticity of Hover Capable Flapping Wings: Experiments and Analysis," *Ph.D. Thesis, University of Maryland, College Park,* 2006.

[6] L. Petricca, P. Ohlckers and C. Grinde, "Micro- and Nano-Air Vehicles: State of the Art," *International Journal of Aerospace Engineering,* vol. 2011, 2011.

[7] T. J. Mueller and S. M. Batill, "Experimental Studies of Separation on a Two-Dimersional Airfoil at Low Reynolds Numbers," *AIAA Journal,* vol. 20, no. 4, pp.

457-463, 1982.

[8] I. H. Tuncer and M. F. Platzer, "Thrust Generation due to Airfoil Flapping," *AIAA Journal,* vol. 34, no. 2, pp. 324-331, 1996.

[9] C. P. Ellington, "The Aerodynamics of Hovering Insect Flight I: The Quasisteady Analysis," *Transactions of the Royal Society,* vol. 305, no. 1122, pp. 1-15, 1984.

[10] K. Taira, C. Rowley, T. Colonius and D. R. Williams, "Lift Enhancement for Low-Aspet-Ratio Wings with Periodic Excitation," *AIAA Journal,* vol. 48, no. 8, 2010.

[11] C. P. Ellington, "The Aerodynamics of Hovering Insect Flight, III: Kinematics," *Phil. Trans. R. Soc. Lon Ser. B,* vol. 305, pp. 41-78, 1984.

[12] S. A. Combes and T. L. Daniel, "Into Thin Air: Contribution of Aerodynamic and Inertial-Elastic Forces to Wing Bending in the Hawkmoth Manduca Sexta," *Journal of Experimental Biology,* vol. 206, pp. 2999-3006, 2003.

[13] M. Ramasamy and J. G. Leishman, "Phase-Locked Particle Image Velocimetry Measurements of a Flapping Wing," *Journal of Aircraft,* vol. 43, no. 6, 2006.

[14] M. H. Dickinson, F. H. Lehmann and S. P. Sane, "Wing Rotation and the Aerodynamic Basis of Insect Flight," *Science,* vol. 305, pp. 1954-1960, 1999.

[15] M. Fuchiwaki, T. Kuroki, K. Tanaka and T. Tababa, "Dynamic Behavior of the Vortex Ring Formed on a Butterfly Wing," *Experiments in Fluids,* vol. 54, no. 1, pp. 1-12, 2013.

[16] A. P. Willmott, C. P. Ellington and A. L. R. Thomas, "Flow Visualization and Unsteady Aerodynamics in the Flight of the Hawkmoth, Manduca Sexta,"

Philosophical Transactions of the Royal Society, vol. 29, no. 1351, pp. 303-316, 1997.

[17] J. M. Birch and M. H. Dickinson, "The Influence of Wing-Wake Interaction of the Production of Aerodynamic Forces in Flapping Flight," *Journal of Experimental Biology,* vol. 206, pp. 2257-2272, 2003.

[18] T. Weis-Fogh, "Quick Estimates of Flight Fitness in Hovering Animals, Including Novel Mechanisms for Lift Production," *Journal of Experimental Biology,* vol. 59, pp. 169-230, 1973.

[19] M. J. Lighthill, "On the Weis-Fogh Mechanism of Lift Generation," *Journal of Fluid Mechanics,* vol. 60, pp. 1-17, 1973.

[20] D. Kolomenskiy, H. K. Moffatt, M. Farge and K. Schneider, "The Lighthill-Weis-Fogh Clap-Fling-Sweep Mechanism Revisited," *Journal of Fluid Mechanics,* 2011.

[21] G. R. Spedding and T. Maxworthy, "The Generation of Circulation and Lift in a Rigid Two-Dimensional Fling," *Journal of Fluid Mechanics,* vol. 165, pp. 247-272, 1986.

[22] L. Bennett, "Clap and Fling Aerodynamics - An Experimental Evaluation," *Journal of Experimental Biology,* vol. 69, pp. 261-272, 1977.

[23] S. P. Sane, "The Aerodynamics of Insect Flight," *Journal of Experimental Biology,* vol. 206, pp. 4191-4208, 2003.

[24] C. P. Ellington, "The Aerodynamics of Normal Hovering Flight: Three Approaches," in *Comparitive Physiology: Water, Ions and Fluid Mechnaics,*

Cambridge, Cambgride University Press, 1978, pp. 327-345.

[25] A. Azuma, S. Azuma, I. Wanatabe and T. Furuta, "Flight Mechanics of a Dragonfly," *Journal of Experimental Biology,* vol. 116, pp. 79-107, 1985.

[26] A. Azuma and T. Wanatabe, "Flight Performance of a Dragonfly," *Journal of Experimental Biology,* vol. 137, pp. 221-252, 1988.

[27] S. P. Sane and M. H. Dickinson, "The Control of Flight Force by a Flapping Wing: Lift and Drag Production," *Journal of Experimental Biology,* vol. 206, pp. 2607-2626, 2001.

[28] M. Smith, P. Wilkin and M. Williams, "The Advantages of an Unsteady Panel Method in Modeling the Aerodynamic Forces on Rigid Flapping Wings," *Journal of Experimental Biology,* vol. 199, pp. 1073-1083, 1996.

[29] J. D. Eldridge, "Efficient Tools for the Simulation of Flapping Wing Flows," in *AIAA Aerospace Sciences Meeting and Exhibit,* Reno, Nevada, 2005.

[30] M. F. Platzer, K. S. Neace and C. K. Pang, "Aerodynamic Analysis of Flapping Wing Propulsion," *AIAA Paper No 93-0484,* 1993.

[31] K. D. Jones and M. F. Platzer, "Numerical Computation of Flapping Wing Propulsion and Power Extraction," *AIAA Paper No. 97-0826,* 1997.

[32] H. Liu and K. Kawachi, "A Numerical Study of Insect Flight," *Jounral of Computational Physics,* vol. 146, 1998.

[33] C. P. Ellington, C. Van den Berg, A. P. Willmott and A. L. R. Thomas, "Leading-Edge Cortices in Insect Flight," *Nature,* vol. 384, pp. 626-630, 1996.

[34] T. Sun and J. Tang, "Unsteady Aerodynamic Force Generation by a Model Fruit Fly Wing in Flapping Motion," *Journal of Experimental Biology,* vol. 205, pp. 50-72, 2002.

[35] R. Ramamurti and W. C. Sandberg, "A Three-Dimensional Computational Study of the Aerodynamic Mechanisms of Insect Flight," *Journal of Experimental Biology,* vol. 205, pp. 1507-1518, 2002.

[36] C. S. Peskin, "Flow Patterns around Heart Valves: A Numerical Method," *Journal of Computational Physics,* vol. 10, 1972.

[37] C. S. Peskin and McQueen, "A Three-Dimensional Computational Method for Blood Flow in the Heart: Immersed Elastic Fibers in a Viscous Incompressible Fluid," *Journal of Computational Physics,* vol. 81, 1989.

[38] R. Verzicco, J. Mohd-Yusof, P. Orlandi and D. Haworth, "LES in Complex Geometries using Boundary Body Forces," *AIAA Journal,* vol. 38, 2000.

[39] G. Kalitzin, G. Iaccarino and B. Khalighi, "Towards and Immersed Boundary Solver for RANS Simulations," *AIAA Journal,* 2003.

[40] M. Bozkurttas, H. Dong, R. Mittal, T. James, H. Ian, G. V. Lauder and P. Madden, "CFD Based Analysis and Design of Biomimetic Flexible Propulsors for Autonomous Underwater Vehicle," in *37th AIAA Fluid Dynamics Conference and Exhibit*, Miami, Florida, 2007.

[41] A. Von Loebbecke, R. Mittal, R. Mark and J. Hahn, "A Computational Method for Analysis of Underwater Dolphin Kick Hydrodynamics in Human Swimming,"

Sports Biomechanics, vol. 8, no. 1, pp. 20-77, 2009.

[42] M. Vanella, T. Fitzgerald, S. Preidikman, E. Balaras and B. Balachandran, "Influence of Flexibility on the Aerodynamic Performance of a Hovering Wing," *Journal of Experimental Biology,* vol. 212, pp. 95-105, 2009.

[43] H. Dong, R. Mittal and F. M. Najjar, "Wake Topology and Hydrodynamic Performance of Low-Aspect-Ratio Flapping Foils," *Journal of Fluid Mechanics,* vol. 566, pp. 309-343, 2006.

[44] J. Emblemsvag and G. Candler, "Simulations of the Unsteady Aerodynamics of the Fruit Fly (Drosophila)," in *34th AIAA Fluid Dynamics Conference and Exhibit*, Portland, OR, 2004.

[45] J. C. I. Newmann, "IIntegrated Multidisciplinary Design Optimization Using Discrete Sensitivity Analysis for Geometrically Comples Aeroelastic Configurations," *Ph.D. Thesis,* 1997.

[46] R. Mittal and G. Iaccarino, "Immersed Boundary Methods," *Annual Reviews of Flid Mechanics,* vol. 37, 2005.

[47] A. P. Kravchenco, P. Moin and R. D. Moser, "Zonal Embedded Grids for Numerical Simulations of Wall-Bounded Turbulent Flows," *Journal of Computational Physics,* vol. 127, 1996.

[48] P. A. Durbin and G. Iaccarino, "An Approach for Local Grid Refinement of Structured Grids," *Journal of Computational Physics,* vol. 181, 2002.

[49] D. Goldstein, R. Handler and L. Sirovich, "Modeling No-Slip Flow Boundary win

an External Force Field," vol. 105, 1993.

[50] E. A. Fadlun, R. Verzicco, P. Orlandi and J. Mohd-Yusof, "Combined Immersed-Boundary Finite Difference Methods for Three-Dimersional Complex Flow Simulations," *Jounral of Computational Physics,* vol. 61, pp. 35-60, 2000.

[51] E. M. Saiki and S. Birinbeg, "Numerical Simulation of a Cylinder in Uniform FLow: Application of a Virtual Boundary Method," *Journal of Compuational Physics,* vol. 123, 1996.

[52] P. Angot, C. H. Bruneau and P. Frabrie, "A Penalization Method to Take Into Account Obstacles in Viscous Flows," *Numerische Mathematik,* vol. 81, 1999.

[53] G. Iaccarino and R. Verzicco, "Immersed Boundary Techniques for Turbulent Flow Simulations," *Applied Mechanics Reviews,* vol. 56, 2003.

[54] J. Yang, "An Embedded-Boundary Formulation for Large Eddy Simulation of Turbulent Flows Interacting with Moving Boundaries," *Ph.D. Thesis, University of Maryland College Park,* 2005.

[55] R. Mittal, Y. Utturkar and H. S. Udaykumar, "Computational Modeling and Analysis of Biomimetic Flight Mechanisms," *AIAA 2002-0865,* 2002.

[56] J. J. Quirk, "An Alternative to Unstructured Grids for Computing Gas Dynamic Flows around Arbitrary Two-Dimensional Bodies," *Computers & Fluids,* vol. 23, 1994.

[57] E. Balaras, "Modeling Complex Boundaries using an External Force Field on Fixed Cartesian Grids in Large-Eddy Simulations," *Computers & Fluids,* vol. 33, pp. 375-

404, 2004.

[58] J. Kim and P. Moin, "Applications of a Fractional Step Method to Incompressible Navier-Stokes Equations," *Jounral of Computational Physics,* vol. 59, pp. 308-323, 1985.

[59] D. Rempfer, "On Boundary Conditions for Incompressible Navier-Stokes Problems," *Applied Mechanics Reviews,* vol. 59, 2006.

[60] C. M. Rhie and W. L. Chow, "Numerical Study of the Turbulent Flow Past an Airfoil with Trailing Edge Separation," *AIAA Journal,* vol. 21, 1983.

[61] K. Kuwahara, S. Komurasaki and A. Bethancourt, Incompressible Flow SImulation by Using Multidirectional Finite Difference Scheme, M. M. Hafez, Ed., World Scientific, 2003.

[62] C. B. Laney, Computational Gasdynamics, Cambridge University Press, 1998.

[63] J. H. Ferziger and M. Peric, Computational Methods for Fluid Dynamics, 3rd ed., Springer, 2002.

[64] H. L. Stone, "Iterative Solution of Implicit Approximation of Multidimensional Partial Differential Equations," *SIAM Journal of Numerical Analysis,* vol. 5, 1968.

[65] M. Zedan and G. E. Schneider, "A Three-Dimensional Modified Strongly Implicit Procedure for Heat Conduction," *AIAA Jounral,* vol. 21, no. 2, 1983.

[66] J. Orlanski, "A Simple Boundary Condition fo Unbounded Hyperbolic Flows," *Journal of Computational Physics,* vol. 21, 1976.

[67] P. S. Bernard and J. M. Wallace, Turbulent Flow Analysis, Measurement, and

Prediction, Hoboken, New Jersey: John Wiley & Sons, 2002.

[68] Y. Zang, R. L. Street and J. R. Koseff, "A Dynamic Mixed Subgrid-Scale Model and its Application to Turbulent Recirculating Flows," *Physics of Fluids,* vol. 5, pp. 3186-3196, 1993.

[69] E. Erturk, T. C. Corke and C. Gökçöl, "Numerical Solutions of 2-D Steady Incompressible Driven Cavity Flow at High Reynolds Numbers," *International Journal for Numerical Methods in Fluids*, vol. 48, 2005.

[70] U. Ghia, Ghia, K. N and C. T. Shin, "High-Re Solutions for Incompressible Flows using the Navier Stokes Equations and Multigrid Method," *Journal of Computational Physics,* vol. 48, 1982.

[71] R. S. Rogallo, "Numerical Experiments in Homogeneous Turbulence," *NASA-TM-81315*, 1981.

[72] N. N. Mansour and A. A. Wray, "Decay of Isotropic Turbulence at Low Reynolds Numbers," *Physics of Fluids,* vol. 6, no. 2, 1994.

[73] S. Majumdar, G. Iaccarino and P. A. Durbin, "RANS Solver with Adaptive Structured Boundary Non-Conforming Grids," *Annual Research Briefs, Center for Turbulence Research, Stanford,* 2001.

[74] J. O'Rourke, Computational Geometry in C, Cambridge University Press, 1998.

[75] W. G. Chinn and N. E. Steenrod, First Concepts of Topology: The Geometry Mappings of Segments, Curves, Circles and Disks, Mathematical Association of America, 1966.

[76] R. Mittal, H. Dong, M. Bozkurttas, A. Von Loebbecke and F. Najjar, "Analysis of Flowing and Swimming in Nature Using and Immersed Boundary Method," in *36th AIAA Fluid Dynamics Conference and Exhibit*, 2006.

[77] J. Kim, D. Kim and H. Choi, "An Immersed-Boundary Finite-Volume Method for Simulations of Flows in Complex Geometries," *Journal of Computational Physics,* vol. 171, 2001.

[78] S. Taneda, "Experimental Investigation of the Wakes behind Cylinders and Plates at Low Reynolds Numbers," *Journal of the Physical Society of Japan,* vol. 11, pp. 302-307, 1956.

[79] D. Russell and Z. J. Wang, "A Cartesian Grid Method for Modeling Multiple Moving Objects in 2D Incompressible Viscous Flows," *Journal of Computational Physics,* vol. 191, pp. 177-205, 2003.

[80] F. L. Ponta, "The KLE Method; A Velocity-Vorticity Formulation for the Navier Stokes Equations," *Mećanica Computacional,* vol. 23, 2004.

[81] J. Yang and E. Balaras, "An Embedded-Boundary Formulation for Large Eddy Simulation of Turbulent FLows Interacting with Moving Boundaries," *Journal of Computational Physics,* vol. 215, 2006.

[82] B. Bush and J. D. Baeder, "Computational Investigation of Flapping-Wing Flight," in *37th AIAA Fluid Dynamics Conference and Exhibit*, Miami, FL, 2007.

[83] T. A. Johnson and V. C. Patel, "Flow Past a Sphere up to a Reynolds Number of 300," *Journal of Fluid Mechanics,* vol. 378, 1999.

[84] S. M. Kaplan, A. Altman and M. Ol, "Angle of Attack and Planform Effects on Flat Plate Trailing Vortices at Low Reynolds Numbers," in *44th AIAA Aerospace Sciences Meeting and Exhibit, 9-12 January*, 2006.

[85] J. G. Leishman, Principles of Helicopter Aerodynamics, Cambridge University Press, 2000.

[86] F. O. Lehmann and M. H. Dickinson, "The Changes in Power Requirements and Muscle Efficiency During Elevated Force Production in the Fruit Fly, Drosophila Melanogaster," *Journal of Experimental Biology*, vol. 200, pp. 1133-1143, 1997.

[87] C. Poelma, W. B. Dickson and M. H. Dickinson, "Time-Resolved Reconstruction of the Full Velocity Field around a Dynamically-Scaled Flapping Wing," *Experimental Fluids*, vol. 41, 2006.

[88] J. M. Birch, W. B. Dickson and M. H. Dickinson, "Force Production and Flow Structure of the Leading Edge Vortex of Flapping Wings at High and Low Reynolds Numbers," *Journal of Experimental Biology*, vol. 207, pp. 1063-1072, 2003.

[89] C. Ostowari and D. Naik, "Post Stall Studies of Untwisted Varying Aspect Ratio Blades with NACA 44XX Series Airfoil Section - Part II," *Wind Engineering*, vol. 9, no. 3, pp. 149-164, 1985.

[90] R. Ramamurti and W. Sandberg, "Simulation of Flow about Flapping Airfoils using Finite Element Incompressible Solver," *AIAA Journal*, vol. 39, no. 2, pp. 253-260, 2001.

[91] J. M. Birch and M. H. Dickinson, "Spanwise Flow and the Attachment of the Leading-Edge Vortex on Insect Wings," *Nature*, vol. 412, pp. 729-733, 2001.

[92] B. Bush, M. Macfarlane, J. Baeder and J. S. Humbert, "Development of Immersed Boundary Code with Applications to MAV Stability Analysis," in *Army Science Conference*, Orlando, Florida, 2010.

[93] J. H. Seo and R. Mittal, "A Sharp-Interface Immersed Boundary Method with Improved Mass Conservation and Reduced Spurious Pressure Oscillations," *Journal of Computational Physics*, vol. 230, pp. 7347-7363, 2011.

[94] A. Yakhot, L. Grinberg and N. Nikitin, "Simulating Pulsatile Flows through a Pipe Orifice by and Immersed-Boundary Method," *Journal of Fluids Engineering*, vol. 126, 2004.

[95] C. H. K. Williamson, "Oblique and Parallel Modes of Vortex Shedding in the Wake of a Circular Cylinder at Low Reynolds Numbers," *Journal of Fluid Mechanics*, vol. 206, 1989.

[96] N. Vandenberghe, J. Zhang and S. Childress, "Symmetry Breaking Leads to Forward Flapping Flight," *Jounral of Fluid Mechanics*, vol. 506, 2004.

[97] D. J. Pines and F. Bohorquez, "Challenges Facing Future Micro-Air-Vehicle Development," *Journal of Aircraft*, vol. 43, 2006.

[98] T. A. Johnson, "Numerical Investigation of Flow past a Sphere up to a Reynolds Number of 300," *Ph.D. Thesis, University of Iowa*, 1996.

[99] J. Jeong and F. Hussain, "On the Identification of a Vortex," *Journal of Fluid*

Mechanics, vol. 285, 1995.

[100] N. A. Gumerov, R. Duriswami and E. A. Borovikov, "Data Structures, Optimal Choice of Parameters, and Complexity Results for Generalized Multilevel Fast Multipole Methods in d Dimensions," *University of Maryland at College Park, Institute for Advanced Computer Studies Technical Report CS-TR-4458,* vol. 91, 2003.

[101] R. Ghias, R. Mittal and T. S. Lund, "A Non-Body Conformal Grid Method for Simulation of Compressible Flows with Complex Geometries," in *42nd AIAA Aerospace Sciences Meeting and Exhibit,* Reno, NV, 2004.

[102] S. C. R. Dennis and G. Chang, "Numerical Solutions for Steady Flow Past a Circular Cylinder at Reynolds Numbers up to 100," *Journal of Fluid Mechanics,* vol. 42, 1970.

[103] E. Balaras and J. Yang, "Nonboundary Conforming Methods for Large Eddy Simulations of Biological Flows," *Journal of Fluids Engineering,* vol. 127, 2005.